

Fermi Large Area Telescope Fourth Source Catalog

6 S. ABDOLLAHI,¹ F. ACERO,² M. ACKERMANN,³ M. AJELLO,⁴ W. B. ATWOOD,⁵ M. AXELSSON,^{6,7}
7 L. BALDINI,⁸ J. BALLE^T,² G. BARBIELLINI,^{9,10} D. BASTIERI,^{11,12} J. BECERRA GONZALEZ,^{13,14,15}
8 R. BELLAZZINI,¹⁶ A. BERRETTA,¹⁷ E. BISSALDI,^{18,19} R. D. BLANDFORD,²⁰ E. D. BLOOM,²⁰
9 R. BONINO,^{21,22} E. BOTTACINI,^{23,20} T. J. BRANDT,¹⁴ J. BREGEON,²⁴ P. BRUEL,²⁵ R. BUEHLER,³
10 T. H. BURNETT,²⁶ S. BUSON,²⁷ R. A. CAMERON,²⁰ R. CAPUTO,¹⁴ P. A. CARAVEO,²⁸
11 J. M. CASANDJIAN,² D. CASTRO,^{29,14} E. CAVAZZUTI,³⁰ E. CHARLES,²⁰ S. CHATY,² S. CHEN,^{11,23}
12 C. C. CHEUNG,³¹ G. CHIARO,²⁸ S. CIPRINI,^{32,33} J. COHEN-TANUGI,²⁴ L. R. COMINSKY,³⁴
13 J. CORONADO-BLÁZQUEZ,^{35,36} D. COSTANTIN,³⁷ A. CUOCO,^{38,21} S. CUTINI,³⁹ F. D'AMMANDO,⁴⁰
14 M. DEKLOTZ,⁴¹ P. DE LA TORRE LUQUE,¹⁸ F. DE PALMA,²¹ A. DESAI,⁴ S. W. DIGEL,²⁰
15 N. DI LALLA,⁸ M. DI MAURO,¹⁴ L. DI VENERE,^{18,19} A. DOMÍNGUEZ,⁴² D. DUMORA,⁴³
16 F. FANA DIRIRSA,⁴⁴ S. J. FEGAN,²⁵ E. C. FERRARA,¹⁴ A. FRANCKOWIAK,³ Y. FUKAZAWA,¹
17 S. FUNK,⁴⁵ P. FUSCO,^{18,19} F. GARGANO,¹⁹ D. GASPARRINI,^{32,33} N. GIGLIETTO,^{18,19} P. GIOMMI,³³
18 F. GIORDANO,^{18,19} M. GIROLETTI,⁴⁰ T. GLANZMAN,²⁰ D. GREEN,⁴⁶ I. A. GRENIER,² S. GRIFFIN,¹⁴
19 M.-H. GRONDIN,⁴³ J. E. GROVE,³¹ S. GUIRIEC,^{47,14} A. K. HARDING,¹⁴ K. HAYASHI,⁴⁸ E. HAYS,¹⁴
20 J.W. HEWITT,⁴⁹ D. HORAN,²⁵ G. JÓHANNESSON,^{50,51} T. J. JOHNSON,⁵² T. KAMAE,⁵³ M. KERR,³¹
21 D. KOCEVSKI,¹⁴ M. KOVAC'EVIC',³⁹ M. KUSS,¹⁶ D. LANDRIU,² S. LARSSON,^{7,54,55} L. LATRONICO,²¹
22 M. LEMOINE-GOUMARD,⁴³ J. LI,³ I. LIODAKIS,²⁰ F. LONGO,^{9,10} F. LOPARCO,^{18,19} B. LOTT,⁴³
23 M. N. LOVELLETTE,³¹ P. LUBRANO,³⁹ G. M. MADEJSKI,²⁰ S. MALDERA,²¹ D. MALYSHEV,⁴⁵
24 A. MANFREDA,⁸ E. J. MARCHESINI,²² L. MARCOTULLI,⁴ G. MARTÍ-DEVESA,⁵⁶ P. MARTIN,⁵⁷
25 F. MASSARO,^{22,21,58} M. N. MAZZIOTTA,¹⁹ J. E. MCENERY,^{14,15} I. MEREU,^{17,39} M. MEYER,^{20,20,20}
26 P. F. MICHELSON,²⁰ N. MIRABAL,^{14,59} T. MIZUNO,⁶⁰ M. E. MONZANI,²⁰ A. MORSELLI,³²
27 I. V. MOSKALENKO,²⁰ M. NEGRO,^{21,22} E. NUSS,²⁴ R. OJHA,¹⁴ N. OMODEI,²⁰ M. ORIENTI,⁴⁰
28 E. ORLANDO,^{20,61} J. F. ORMES,⁶² M. PALATIELLO,^{9,10} V. S. PALIYA,³ D. PANEQUE,⁴⁶ Z. PEI,¹²
29 H. PEÑA-HERAZO,^{22,21,58,63} J. S. PERKINS,¹⁴ M. PERSIC,^{9,64} M. PESCE-ROLLINS,¹⁶ V. PETROSIAN,²⁰
30 L. PETROV,¹⁴ F. PIRON,²⁴ H. POON,¹ T. A. PORTER,²⁰ G. PRINCIPE,⁴⁰ S. RAINÒ,^{18,19}
31 R. RANDO,^{11,12} M. RAZZANO,^{16,65} S. RAZZAQUE,⁴⁴ A. REIMER,^{56,20} O. REIMER,⁵⁶ Q. REMY,²⁴
32 T. REPOSEUR,⁴³ R. W. ROMANI,²⁰ P. M. SAZ PARKINSON,^{5,66,67} F. K. SCHINZEL,^{68,69} D. SERINI,¹⁸
33 C. SGRÒ,¹⁶ E. J. SISKIND,⁷⁰ D. A. SMITH,⁴³ G. SPANDRE,¹⁶ P. SPINELLI,^{18,19} A. W. STRONG,⁷¹
34 D. J. SUSON,⁷² H. TAJIMA,^{73,20} M. N. TAKAHASHI,⁴⁶ D. TAK,^{74,14} J. B. THAYER,²⁰
35 D. J. THOMPSON,¹⁴ L. TIBALDO,⁵⁷ D. F. TORRES,^{75,76} E. TORRESI,⁷⁷ J. VALVERDE,²⁵
36 B. VAN KLAVEREN,²⁰ P. VAN ZYL,^{78,79,80} K. WOOD,⁸¹ M. YASSINE,^{9,10} AND G. ZAHARIJAS^{61,82}

37 ¹*Department of Physical Sciences, Hiroshima University, Higashi-Hiroshima, Hiroshima 739-8526, Japan*
38 ²*AIM, CEA, CNRS, Université Paris-Saclay, Université Paris Diderot, Sorbonne Paris Cité, F-91191 Gif-sur-Yvette,*
39 *France*

40 ³*Deutsches Elektronen Synchrotron DESY, D-15738 Zeuthen, Germany*

41 ⁴*Department of Physics and Astronomy, Clemson University, Kinard Lab of Physics, Clemson, SC 29634-0978, USA*

42 ⁵*Santa Cruz Institute for Particle Physics, Department of Physics and Department of Astronomy and Astrophysics,*
43 *University of California at Santa Cruz, Santa Cruz, CA 95064, USA*

44 ⁶*Department of Physics, Stockholm University, AlbaNova, SE-106 91 Stockholm, Sweden*

jean.ballet@cea.fr

tburnett@u.washington.edu

digel@stanford.edu

lott@cenbg.in2p3.fr

- 45 ⁷*Department of Physics, KTH Royal Institute of Technology, AlbaNova, SE-106 91 Stockholm, Sweden*
- 46 ⁸*Università di Pisa and Istituto Nazionale di Fisica Nucleare, Sezione di Pisa I-56127 Pisa, Italy*
- 47 ⁹*Istituto Nazionale di Fisica Nucleare, Sezione di Trieste, I-34127 Trieste, Italy*
- 48 ¹⁰*Dipartimento di Fisica, Università di Trieste, I-34127 Trieste, Italy*
- 49 ¹¹*Istituto Nazionale di Fisica Nucleare, Sezione di Padova, I-35131 Padova, Italy*
- 50 ¹²*Dipartimento di Fisica e Astronomia “G. Galilei”, Università di Padova, I-35131 Padova, Italy*
- 51 ¹³*Instituto de Astrofísica de Canarias, Observatorio del Teide, C/Via Lactea, s/n, E38205, La Laguna, Tenerife, Spain*
- 52 ¹⁴*NASA Goddard Space Flight Center, Greenbelt, MD 20771, USA*
- 53 ¹⁵*Department of Astronomy, University of Maryland, College Park, MD 20742, USA*
- 54 ¹⁶*Istituto Nazionale di Fisica Nucleare, Sezione di Pisa, I-56127 Pisa, Italy*
- 55 ¹⁷*Dipartimento di Fisica, Università degli Studi di Perugia, I-06123 Perugia, Italy*
- 56 ¹⁸*Dipartimento di Fisica “M. Merlin” dell’Università e del Politecnico di Bari, I-70126 Bari, Italy*
- 57 ¹⁹*Istituto Nazionale di Fisica Nucleare, Sezione di Bari, I-70126 Bari, Italy*
- 58 ²⁰*W. W. Hansen Experimental Physics Laboratory, Kavli Institute for Particle Astrophysics and Cosmology,*
- 59 *Department of Physics and SLAC National Accelerator Laboratory, Stanford University, Stanford, CA 94305, USA*
- 60 ²¹*Istituto Nazionale di Fisica Nucleare, Sezione di Torino, I-10125 Torino, Italy*
- 61 ²²*Dipartimento di Fisica, Università degli Studi di Torino, I-10125 Torino, Italy*
- 62 ²³*Department of Physics and Astronomy, University of Padova, Vicolo Osservatorio 3, I-35122 Padova, Italy*
- 63 ²⁴*Laboratoire Univers et Particules de Montpellier, Université Montpellier, CNRS/IN2P3, F-34095 Montpellier,*
- 64 *France*
- 65 ²⁵*Laboratoire Leprince-Ringuet, École polytechnique, CNRS/IN2P3, F-91128 Palaiseau, France*
- 66 ²⁶*Department of Physics, University of Washington, Seattle, WA 98195-1560, USA*
- 67 ²⁷*Institut für Theoretische Physik and Astrophysik, Universität Würzburg, D-97074 Würzburg, Germany*
- 68 ²⁸*INAF-Istituto di Astrofisica Spaziale e Fisica Cosmica Milano, via E. Bassini 15, I-20133 Milano, Italy*
- 69 ²⁹*Harvard-Smithsonian Center for Astrophysics, Cambridge, MA 02138, USA*
- 70 ³⁰*Italian Space Agency, Via del Politecnico snc, 00133 Roma, Italy*
- 71 ³¹*Space Science Division, Naval Research Laboratory, Washington, DC 20375-5352, USA*
- 72 ³²*Istituto Nazionale di Fisica Nucleare, Sezione di Roma “Tor Vergata”, I-00133 Roma, Italy*
- 73 ³³*Space Science Data Center - Agenzia Spaziale Italiana, Via del Politecnico, snc, I-00133, Roma, Italy*
- 74 ³⁴*Department of Physics and Astronomy, Sonoma State University, Rohnert Park, CA 94928-3609, USA*
- 75 ³⁵*Instituto de Física Teórica UAM/CSIC, Universidad Autónoma de Madrid, 28049, Madrid, Spain*
- 76 ³⁶*Departamento de Física Teórica, Universidad Autónoma de Madrid, 28049 Madrid, Spain*
- 77 ³⁷*University of Padua, Department of Statistical Science, Via 8 Febbraio, 2, 35122 Padova*
- 78 ³⁸*RWTH Aachen University, Institute for Theoretical Particle Physics and Cosmology, (TTK), D-52056 Aachen,*
- 79 *Germany*
- 80 ³⁹*Istituto Nazionale di Fisica Nucleare, Sezione di Perugia, I-06123 Perugia, Italy*
- 81 ⁴⁰*INAF Istituto di Radioastronomia, I-40129 Bologna, Italy*
- 82 ⁴¹*Stellar Solutions Inc., 250 Cambridge Avenue, Suite 204, Palo Alto, CA 94306, USA*
- 83 ⁴²*Grupo de Altas Energías, Universidad Complutense de Madrid, E-28040 Madrid, Spain*
- 84 ⁴³*Centre d’Études Nucléaires de Bordeaux Gradignan, IN2P3/CNRS, Université Bordeaux 1, BP120, F-33175*
- 85 *Gradignan Cedex, France*
- 86 ⁴⁴*Department of Physics, University of Johannesburg, PO Box 524, Auckland Park 2006, South Africa*
- 87 ⁴⁵*Friedrich-Alexander Universität Erlangen-Nürnberg, Erlangen Centre for Astroparticle Physics, Erwin-Rommel-Str.*
- 88 *1, 91058 Erlangen, Germany*
- 89 ⁴⁶*Max-Planck-Institut für Physik, D-80805 München, Germany*
- 90 ⁴⁷*The George Washington University, Department of Physics, 725 21st St, NW, Washington, DC 20052, USA*
- 91 ⁴⁸*Department of Physics and Astrophysics, Nagoya University, Chikusa-ku Nagoya 464-8602, Japan*

- 92 ⁴⁹*University of North Florida, Department of Physics, 1 UNF Drive, Jacksonville, FL 32224, USA*
 93 ⁵⁰*Science Institute, University of Iceland, IS-107 Reykjavik, Iceland*
 94 ⁵¹*Nordita, Royal Institute of Technology and Stockholm University, Roslagstullsbacken 23, SE-106 91 Stockholm,*
 95 *Sweden*
 96 ⁵²*College of Science, George Mason University, Fairfax, VA 22030, resident at Naval Research Laboratory,*
 97 *Washington, DC 20375, USA*
 98 ⁵³*Department of Physics, Graduate School of Science, University of Tokyo, 7-3-1 Hongo, Bunkyo-ku, Tokyo 113-0033,*
 99 *Japan*
 100 ⁵⁴*The Oskar Klein Centre for Cosmoparticle Physics, AlbaNova, SE-106 91 Stockholm, Sweden*
 101 ⁵⁵*School of Education, Health and Social Studies, Natural Science, Dalarna University, SE-791 88 Falun, Sweden*
 102 ⁵⁶*Institut für Astro- und Teilchenphysik, Leopold-Franzens-Universität Innsbruck, A-6020 Innsbruck, Austria*
 103 ⁵⁷*IRAP, Université de Toulouse, CNRS, UPS, CNES, F-31028 Toulouse, France*
 104 ⁵⁸*Istituto Nazionale di Astrofisica-Osservatorio Astrofisico di Torino, via Osservatorio 20, I-10025 Pino Torinese,*
 105 *Italy*
 106 ⁵⁹*Department of Physics and Center for Space Sciences and Technology, University of Maryland Baltimore County,*
 107 *Baltimore, MD 21250, USA*
 108 ⁶⁰*Hiroshima Astrophysical Science Center, Hiroshima University, Higashi-Hiroshima, Hiroshima 739-8526, Japan*
 109 ⁶¹*Istituto Nazionale di Fisica Nucleare, Sezione di Trieste, and Università di Trieste, I-34127 Trieste, Italy*
 110 ⁶²*Department of Physics and Astronomy, University of Denver, Denver, CO 80208, USA*
 111 ⁶³*Instituto Nacional de Astrofisica, Óptica y Electrónica, Tonantzintla, Puebla 72840, Mexico*
 112 ⁶⁴*Osservatorio Astronomico di Trieste, Istituto Nazionale di Astrofisica, I-34143 Trieste, Italy*
 113 ⁶⁵*Funded by contract FIRB-2012-RBFR12PM1F from the Italian Ministry of Education, University and Research*
 114 *(MIUR)*
 115 ⁶⁶*Department of Physics, The University of Hong Kong, Pokfulam Road, Hong Kong, China*
 116 ⁶⁷*Laboratory for Space Research, The University of Hong Kong, Hong Kong, China*
 117 ⁶⁸*National Radio Astronomy Observatory, 1003 Lopezville Road, Socorro, NM 87801, USA*
 118 ⁶⁹*University of New Mexico, MSC07 4220, Albuquerque, NM 87131, USA*
 119 ⁷⁰*NYCB Real-Time Computing Inc., Lattingtown, NY 11560-1025, USA*
 120 ⁷¹*Max-Planck Institut für extraterrestrische Physik, D-85748 Garching, Germany*
 121 ⁷²*Purdue University Northwest, Hammond, IN 46323, USA*
 122 ⁷³*Solar-Terrestrial Environment Laboratory, Nagoya University, Nagoya 464-8601, Japan*
 123 ⁷⁴*Department of Physics, University of Maryland, College Park, MD 20742, USA*
 124 ⁷⁵*Institute of Space Sciences (CSICIEEC), Campus UAB, Carrer de Magrans s/n, E-08193 Barcelona, Spain*
 125 ⁷⁶*Institució Catalana de Recerca i Estudis Avançats (ICREA), E-08010 Barcelona, Spain*
 126 ⁷⁷*INAF-Istituto di Astrofisica Spaziale e Fisica Cosmica Bologna, via P. Gobetti 101, I-40129 Bologna, Italy*
 127 ⁷⁸*Hartebeesthoek Radio Astronomy Observatory, PO Box 443, Krugersdorp 1740, South Africa*
 128 ⁷⁹*School of Physics, University of the Witwatersrand, Private Bag 3, WITS-2050, Johannesburg, South Africa*
 129 ⁸⁰*Square Kilometre Array South Africa, Pinelands, 7405, South Africa*
 130 ⁸¹*Praxis Inc., Alexandria, VA 22303, resident at Naval Research Laboratory, Washington, DC 20375, USA*
 131 ⁸²*Center for Astrophysics and Cosmology, University of Nova Gorica, Nova Gorica, Slovenia*

ABSTRACT

132
 133 We present the fourth *Fermi* Large Area Telescope catalog (4FGL) of γ -ray sources.
 134 Based on the first eight years of science data from the *Fermi* Gamma-ray Space Telescope
 135 mission in the energy range from 50 MeV to 1 TeV, it is the deepest yet in this
 136 energy range. Relative to the 3FGL catalog, the 4FGL catalog has twice as much
 137 exposure as well as a number of analysis improvements, including an updated model

for the Galactic diffuse γ -ray emission, and two sets of light curves (1-year and 2-month intervals). The 4FGL catalog includes 5065 sources above 4σ significance, for which we provide localization and spectral properties. Seventy-five sources are modeled explicitly as spatially extended, and overall 354 sources are considered as identified based on angular extent, periodicity or correlated variability observed at other wavelengths. For 1337 sources we have not found plausible counterparts at other wavelengths. More than 3130 of the identified or associated sources are active galaxies of the blazar class, and 239 are pulsars.

Keywords: Gamma rays: general — surveys — catalogs

1. INTRODUCTION

The *Fermi Gamma-ray Space Telescope* was launched in June 2008, and the Large Area Telescope (LAT) onboard has been continually surveying the sky in the GeV energy range since then. Integrating the data over many years, the *Fermi*-LAT collaboration produced several generations of high-energy γ -ray source catalogs (Table 1). The previous all-purpose catalog (3FGL, [Acero et al. 2015](#)) contained 3033 sources, mostly active galactic nuclei (AGN) and pulsars, but also a variety of other types of extragalactic and Galactic sources.

This paper presents the fourth catalog of sources, abbreviated as 4FGL (for *Fermi* Gamma-ray LAT) detected in the first eight years of the mission. As in previous catalogs, sources are included based on the statistical significance of their detection considered over the entire time period of the analysis. For this reason the 4FGL catalog does not contain transient γ -ray sources which are detectable only over a short duration, including Gamma-ray Bursts (GRBs, [Ajello et al. 2019](#)), solar flares ([Ackermann et al. 2014a](#)), and most novae ([Ackermann et al. 2014b](#)).

The 4FGL catalog benefits from a number of improvements with respect to the 3FGL, besides the twice longer exposure:

1. We used Pass 8 data¹ (§ 2.2). The principal difference relative to the P7REP data used for 3FGL is about 20% larger acceptance at all energies and improved angular resolution above 3 GeV.
2. We developed a new model of the underlying diffuse Galactic emission (§ 2.4).
3. We introduced weights in the maximum likelihood analysis (§ 3.2) to mitigate the effect of systematic errors due to our imperfect knowledge of the Galactic diffuse emission.
4. We tested all sources with three spectral models (power law, log normal and power law with subexponential cutoff, § 3.3).
5. We explicitly modeled 75 sources as extended emission regions (§ 3.4), up from 25 in 3FGL.
6. We built light curves and tested variability using two different time bins (one year and two months, § 3.6).

¹ See http://fermi.gsfc.nasa.gov/ssc/data/analysis/documentation/Pass8_usage.html.

Table 1. Previous *Fermi*-LAT catalogs

Acronym	IRFs/Diffuse model	Energy range/Duration	Sources	Analysis/Reference
1FGL	P6_V3_DIFFUSE gll_iem_v02	0.1 – 100 GeV 11 months	1451 (P)	Unbinned, F/B Abdo et al. (2010a)
2FGL	P7SOURCE_V6 gal_2yearp7v6_v0	0.1 – 100 GeV 2 years	1873 (P)	Binned, F/B Nolan et al. (2012)
3FGL	P7REP_SOURCE_V15 gll_iem_v06	0.1 – 300 GeV 4 years	3033 (P)	Binned, F/B Acero et al. (2015)
FGES	P8R2_SOURCE_V6 gll_iem_v06	10 GeV – 2 TeV 6 years	46 (E)	Binned, PSF, $ b < 7^\circ$ Ackermann et al. (2017b)
3FHL	P8R2_SOURCE_V6 gll_iem_v06	10 GeV – 2 TeV 7 years	1556 (P)	Unbinned, PSF Ajello et al. (2017)
FHES	P8R2_SOURCE_V6 gll_iem_v06	1 GeV – 1 TeV 7.5 years	24 (E)	Binned, PSF, $ b > 5^\circ$ Ackermann et al. (2018)
4FGL	P8R3_SOURCE_V2 gll_iem_v07 (§ 2.4.1)	0.05 GeV – 1 TeV 8 years	5065 (P)	Binned, PSF this work

NOTE—In the Analysis column, F/B stands for *Front/Back*, and PSF for PSF event types^a. In the Sources column, we write (P) when the catalog’s objective is to look for point-like sources, (E) when it looks for extended sources.

^aSee https://fermi.gsfc.nasa.gov/ssc/data/analysis/LAT_essentials.html.

173 7. To study the associations of LAT sources with counterparts at other wavelengths, we updated
174 several of the counterpart catalogs, and correspondingly recalibrated the association procedure.

175 A preliminary version of this catalog (FL8Y²) was built from the same data and the same software,
176 but using the previous interstellar emission model (gll_iem_v06) as background, starting at 100 MeV
177 and switching to curved spectra at $TS_{\text{curv}} > 16$ (see § 3.3 for definition). We use it as a starting
178 point for source detection and localization, and to estimate the impact of changing the underlying
179 diffuse model. The result of a dedicated effort for studying the AGN population in the 4FGL catalog
180 is published in the accompanying fourth LAT AGN catalog (4LAC, [Fermi-LAT collaboration 2019](#))
181 paper.

182 Section 2 describes the LAT, the data, and the models for the diffuse backgrounds, celestial and
183 otherwise. Section 3 describes the construction of the catalog, with emphasis on what has changed
184 since the analysis for the 3FGL catalog. Section 4 describes the catalog itself, Section 5 explains the
185 association and identification procedure, and Section 6 details the association results. We conclude
186 in Section 7. We provide appendices with technical details of the analysis and of the format of the
187 electronic version of the catalog.

188

2. INSTRUMENT & BACKGROUND

² See <https://fermi.gsfc.nasa.gov/ssc/data/access/lat/fl8y/>.

2.1. The Large Area Telescope

189 The LAT detects γ rays in the energy range from 20 MeV to more than 1 TeV, measuring their
 190 arrival times, energies, and directions. The field of view of the LAT is ~ 2.7 sr at 1 GeV and above.
 191 The per-photon angular resolution (point-spread function, PSF, 68% containment radius) is $\sim 5^\circ$
 192 at 100 MeV, improving to 0.8° at 1 GeV (averaged over the acceptance of the LAT), varying with
 193 energy approximately as $E^{-0.8}$ and asymptoting at $\sim 0.1^\circ$ above 20 GeV (Figure 1). The tracking
 194 section of the LAT has 36 layers of silicon strip detectors interleaved with 16 layers of tungsten foil
 195 (12 thin layers, 0.03 radiation length, at the top or *Front* of the instrument, followed by 4 thick
 196 layers, 0.18 radiation lengths, in the *Back* section). The silicon strips track charged particles, and
 197 the tungsten foils facilitate conversion of γ rays to positron-electron pairs. Beneath the tracker is a
 198 calorimeter composed of an 8-layer array of CsI crystals (~ 8.5 total radiation lengths) to determine
 199 the γ -ray energy. More information about the LAT is provided in [Atwood et al. \(2009\)](#), and the
 200 in-flight calibration of the LAT is described in [Abdo et al. \(2009a\)](#), [Ackermann et al. \(2012a\)](#) and
 201 [Ackermann et al. \(2012b\)](#).

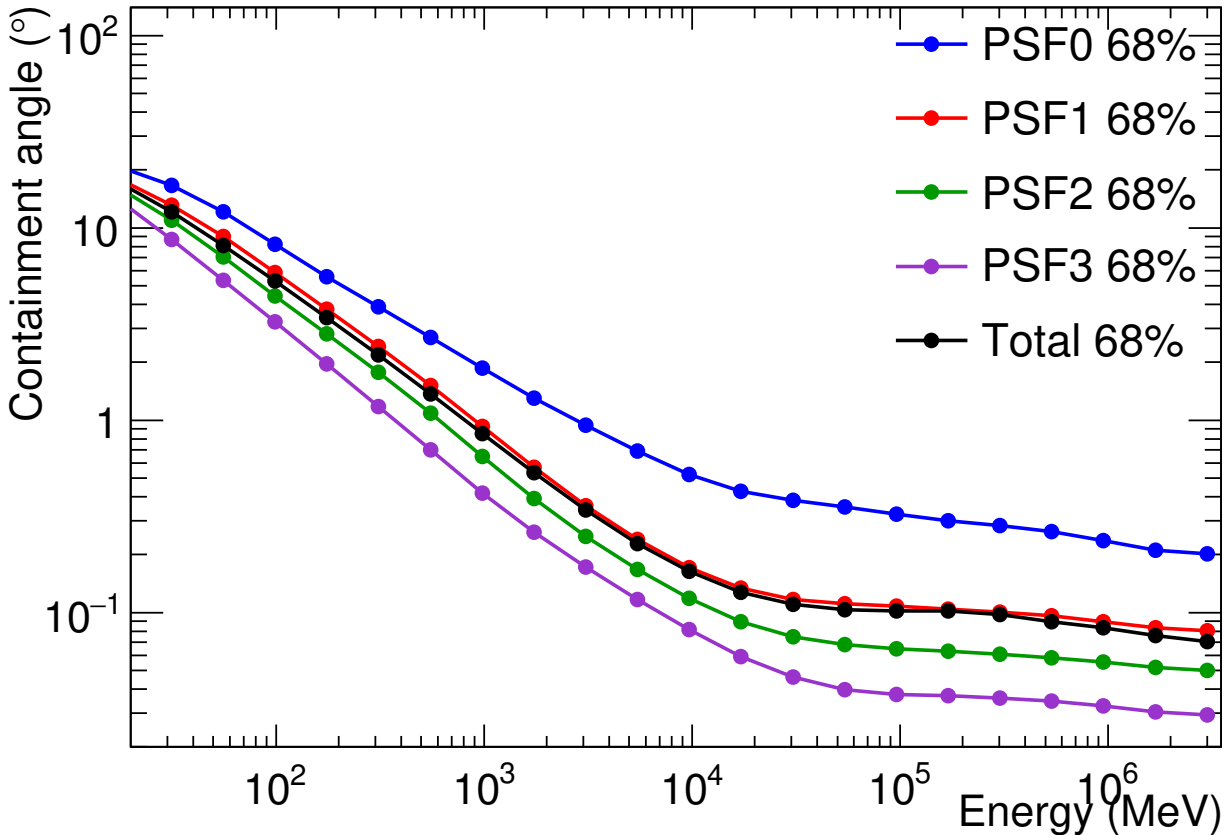


Figure 1. Containment angle (68%) of the *Fermi*-LAT PSF as a function of energy, averaged over off-axis angle. The black line is the average over all data, whereas the colored lines illustrate the difference between the four categories of events ranked by PSF quality from worst (PSF0) to best (PSF3).

203 The LAT is also an efficient detector of the intense background of charged particles from cosmic
 204 rays and trapped radiation at the orbit of the *Fermi* satellite. A segmented charged-particle
 205 anticoincidence detector (plastic scintillators read out by photomultiplier tubes) around the tracker
 206 is used to reject charged-particle background events. Accounting for γ rays lost in filtering charged
 207 particles from the data, the effective collecting area at normal incidence (for the P8R3_SOURCE_V2
 208 event selection used here; see below)³ exceeds 0.3 m² at 0.1 GeV, 0.8 m² at 1 GeV, and remains
 209 nearly constant at ~ 0.9 m² from 2 to 500 GeV. The live time is nearly 76%, limited primarily
 210 by interruptions of data taking when *Fermi* is passing through the South Atlantic Anomaly (SAA,
 211 $\sim 15\%$) and readout dead-time fraction ($\sim 9\%$).

2.2. The LAT Data

212
 213 The data for the 4FGL catalog were taken during the period 2008 August 4 (15:43 UTC) to 2016
 214 August 2 (05:44 UTC) covering eight years. During most of this time, *Fermi* was operated in sky-
 215 scanning survey mode (viewing direction rocking north and south of the zenith on alternate orbits).
 216 As in 3FGL, intervals around solar flares and bright GRBs were excised. Overall, about two days
 217 were excised due to solar flares, and 39 ks due to 30 GRBs. The precise time intervals corresponding
 218 to selected events are recorded in the GTI extension of the FITS file (Appendix A). The maximum
 219 exposure (4.5×10^{11} cm² s at 1 GeV) is reached at the North celestial pole. The minimum exposure
 220 (2.7×10^{11} cm² s at 1 GeV) is reached at the celestial equator.

221 The current version of the LAT data is Pass 8 P8R3 (Atwood et al. 2013; Bruel et al. 2018). It
 222 offers 20% more acceptance than P7REP (Bregeson et al. 2013) and a narrower PSF at high energies.
 223 Both aspects are very useful for source detection and localization (Ajello et al. 2017). We used the
 224 Source class event selection, with the Instrument Response Functions (IRFs) P8R3_SOURCE_V2.
 225 We took advantage of the new PSF event types (Figure 1) to avoid mixing poorly localized events
 226 (PSF0) with high-quality ones (PSF3).

227 The lower bound of the energy range was set to 50 MeV, down from 100 MeV in 3FGL, to constrain
 228 the spectra better at low energy. It does not help detecting or localizing sources because of the very
 229 broad PSF below 100 MeV. The upper bound was raised from 300 GeV in 3FGL to 1 TeV. This is
 230 because as the source-to-background ratio decreases, the sensitivity curve (Figure 18 of Abdo et al.
 231 2010a, 1FGL) shifts to higher energies. The 3FHL catalog (Ajello et al. 2017) went up to 2 TeV, but
 232 only 566 events exceed 1 TeV over 8 years (to be compared to 714,000 above 10 GeV).

2.3. Zenith angle selection

233
 234 The zenith angle cut was set such that the contribution of the Earth limb at that zenith angle was
 235 less than 10% of the total (Galactic + isotropic) background. Integrated over all zenith angles, the
 236 residual Earth limb contamination is less than 1%. We kept PSF3 event types with zenith angles
 237 less than 80° between 50 and 100 MeV, PSF2 and PSF3 event types with zenith angles less than
 238 90° between 100 and 300 MeV, and PSF1, PSF2 and PSF3 event types with zenith angles less than
 239 100° between 300 MeV and 1 GeV. Above 1 GeV we kept all events with zenith angles less than 105°
 240 (Table 2).

241 The resulting integrated exposure over 8 years is shown in Figure 2. The dependence on declination
 242 is due to the combination of the inclination of the orbit (25.6°), the rocking angle, the zenith angle

³ See http://www.slac.stanford.edu/exp/glast/groups/canda/lat_Performance.htm.

Table 2. 4FGL Summed Likelihood components

Energy interval (GeV)	NBins	ZMax (deg)	Ring width (deg)	Pixel size (deg)				
				PSF0	PSF1	PSF2	PSF3	All
0.05 – 0.1	3	80	7	0.6	...
0.1 – 0.3	5	90	7	0.6	0.6	...
0.3 – 1	6	100	5	...	0.4	0.3	0.2	...
1 – 3	5	105	4	0.4	0.15	0.1	0.1	...
3 – 10	6	105	3	0.25	0.1	0.05	0.04	...
10 – 1000	10	105	2	0.04

NOTE—We used 15 components (all in binned mode) in the 4FGL Summed Likelihood approach (§ 3.2). Components in a given energy interval share the same number of energy bins, the same zenith angle selection and the same ROI size, but have different pixel sizes in order to adapt to the PSF width (Figure 1). Each filled entry under Pixel size corresponds to one component of the summed log-likelihood. NBins is the number of energy bins in the interval, ZMax is the zenith angle cut, Ring width refers to the difference between the ROI core and the extraction region, as explained in item 5 of § 3.2.

243 selection and the off-axis effective area. The north-south asymmetry is due to the SAA, over which no
 244 scientific data is taken. Because of the regular precession of the orbit every 53 days, the dependence
 245 on right ascension is small when averaged over long periods of time. The main dependence on energy
 246 is due to the increase of the effective area up to 1 GeV, and the addition of new event types at
 247 100 MeV, 300 MeV and 1 GeV. The off-axis effective area depends somewhat on energy and event
 248 type. This, together with the different zenith angle selections, introduces a slight dependence of the
 249 shape of the curve on energy.

250 Selecting on zenith angle applies a kind of time selection (which depends on direction in the sky).
 251 This means that the effective time selection at low energy is not exactly the same as at high energy.
 252 The periods of time during which a source is at zenith angle $< 105^\circ$ but (for example) $> 90^\circ$
 253 last typically a few minutes every orbit. This is shorter than the main variability time scales of
 254 astrophysical sources in 4FGL, and therefore not a concern. There remains however the modulation
 255 due to the precession of the spacecraft orbit on longer time scales over which blazars can vary. This is
 256 not a problem for a catalog (it can at most appear as a spectral effect, and should average out when
 257 considering statistical properties) but it should be kept in mind when extracting spectral parameters
 258 of individual variable sources. We used the same zenith angle cut for all event types in a given energy
 259 interval, to reduce systematics due to that time selection.

260 Because the data are limited by systematics at low energies everywhere in the sky (Appendix B)
 261 rejecting half of the events below 300 MeV and 75% of them below 100 MeV does not impact the
 262 sensitivity (if we had kept these events, the weights would have been lower).

263 2.4. Model for the Diffuse Gamma-Ray Background

264 2.4.1. Diffuse emission of the Milky Way

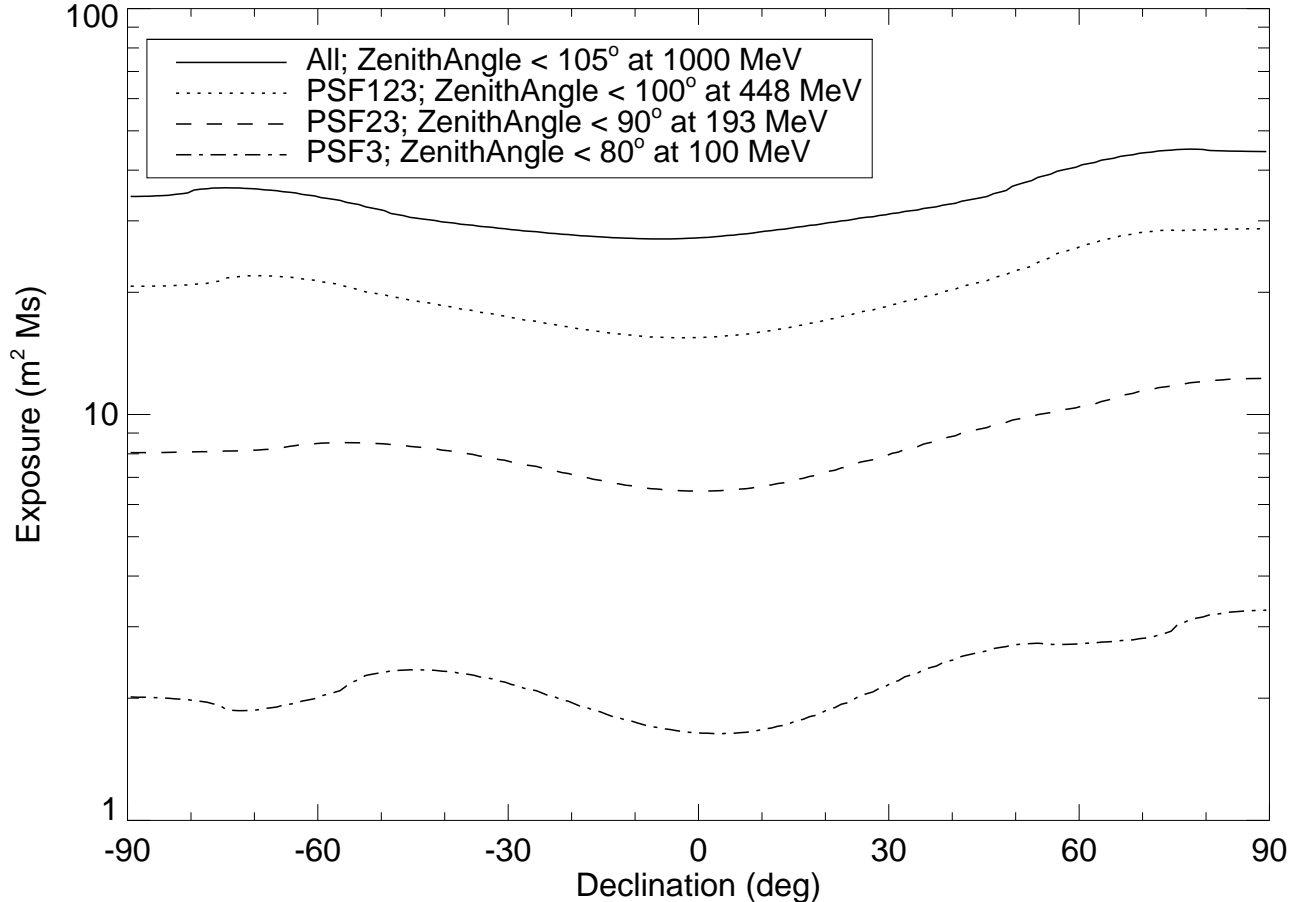


Figure 2. Exposure as a function of declination and energy, averaged over right ascension, summed over all relevant event types as indicated in the figure legend.

265 We extensively updated the model of the Galactic diffuse emission for the 4FGL analysis, using the
 266 same P8R3 data selections (PSF types, energy ranges, and zenith angle limits). The development
 267 of the model is described in more detail online⁴. Here we summarize the primary differences from
 268 the model developed for the 3FGL catalog (Acero et al. 2016a). In both cases, the model is based
 269 on linear combinations of templates representing components of the Galactic diffuse emission. For
 270 4FGL we updated all of the templates, and added a new one as described below.

271 We have adopted the new, all-sky high-resolution, 21-cm spectral line HI4PI survey (HI4PI
 272 Collaboration et al. 2016) as our tracer of HI, and extensively refined the procedure for partitioning
 273 the HI and H₂ (traced by the 2.6-mm CO line) into separate ranges of Galactocentric distance
 274 (‘rings’), by decomposing the spectra into individual line profiles, so the broad velocity dispersion of
 275 massive interstellar clouds does not effectively distribute their emission very broadly along the line of
 276 sight. We also updated the rotation curve, and adopted a new procedure for interpolating the rings
 277 across the Galactic center and anticenter, now incorporating a general model for the surface density

⁴ https://fermi.gsfc.nasa.gov/ssc/data/analysis/software/aux/4fgl/Galactic_Diffuse_Emission_Model_for_the_4FGL_Catalog_Analysis.pdf

278 distribution of the interstellar medium to inform the interpolation, and defining separate rings for
 279 the Central Molecular Zone (within ~ 150 pc of the Galactic center and between 150 pc and 600 pc
 280 of the center). With this approach, the Galaxy is divided into ten concentric rings.

281 The template for the inverse Compton emission is still based on a model interstellar radiation field
 282 and cosmic-ray electron distribution (calculated in GALPROP v56, described in Porter et al. 2017)⁵
 283 but now we formally subdivide the model into rings (with the same Galactocentric radius ranges as
 284 for the gas templates), which are fit separately in the analysis, to allow some spatial freedom relative
 285 to the static all-sky inverse-Compton model.

286 We have also updated the template of the ‘dark gas’ component (Grenier et al. 2005), representing
 287 interstellar gas that is not traced by the HI and CO line surveys, by comparison with the *Planck*
 288 dust optical depth map⁶. The dark gas is inferred as the residual component after the best-fitting
 289 linear combination of total $N(\text{HI})$ and W_{CO} is subtracted, i.e., as the component not correlated with
 290 the atomic and molecular gas spectral line tracers, in a procedure similar to that used in Acero et al.
 291 (2016a). In particular, as before we retained the negative residuals as a ‘column density correction
 292 map’.

293 New to the 4FGL model, we incorporated a template representing the contribution of unresolved
 294 Galactic sources. This was derived from the model spatial distribution and luminosity function
 295 developed based on the distribution of Galactic sources in Acero et al. (2015) and an analytical
 296 evaluation of the flux limit for source detection as a function of direction on the sky.

297 As for the 3FGL model, we iteratively determined and re-fit a model component that represents
 298 non-template diffuse γ -ray emission, primarily Loop I and the *Fermi* bubbles. To avoid overfitting
 299 the residuals, and possibly suppressing faint Galactic sources, we spectrally and spatially smoothed
 300 the residual template.

301 The model fitting was performed using Gardian (Ackermann et al. 2012d), as a summed log-
 302 likelihood analysis. This procedure involves transforming the ring maps described above into spatial-
 303 spectral templates evaluated in GALPROP. We used model $^{\text{S}}\text{L}^{\text{Z}}6^{\text{R}}30^{\text{T}}150^{\text{C}}2$ from Ackermann et al.
 304 (2012d). The model is a linear combination of these templates, with free scaling functions of various
 305 forms for the individual templates. For components with the largest contributions, a piecewise
 306 continuous function, linear in the logarithm of energy, with nine degrees of freedom was used. Other
 307 components had a similar scaling function with five degrees of freedom, or power-law scaling, or
 308 overall scale factors, chosen to give the model adequate freedom while reducing the overall number
 309 of free parameters. The model also required a template for the point and small-extended sources in
 310 the sky. We iterated the fitting using preliminary versions of the 4FGL catalog. This template was
 311 also given spectral degrees of freedom. Other diffuse templates, described below and not related to
 312 Galactic emission, were included in the model fitting.

313 2.4.2. Isotropic background

314 The isotropic diffuse background was derived over 45 energy bins covering the energy range 30 MeV
 315 to 1 TeV, from the eight-year data set excluding the Galactic plane ($|b| > 15^\circ$). To avoid the Earth
 316 limb emission (more conspicuous around the celestial poles), we applied a zenith angle cut at 80° and
 317 also excluded declinations higher than 60° below 300 MeV. The isotropic background was obtained

⁵ <http://galprop.stanford.edu>

⁶ COM_CompMap_Dust-GNILC-Model-Opacity_2048_R2.01.fits, Planck Collaboration et al. (2016)

318 as the residual between the spatially-averaged data and the sum of the Galactic diffuse emission
 319 model described above, a preliminary version of the 4FGL catalog and the solar and lunar templates
 320 (§ 2.4.3), so it includes charged particles misclassified as γ rays. We implicitly assume that the
 321 acceptance for these residual charged particles is the same as for γ rays in treating these diffuse
 322 background components together. To obtain a continuous model, the final spectral template was
 323 obtained by fitting the residuals in the 45 energy bins to a multiply broken power law with 18 breaks.
 324 For the analysis we derived the contributions to the isotropic background separately for each event
 325 type.

326 2.4.3. *Solar and lunar template*

327 The quiescent Sun and the Moon are fairly bright γ -ray sources. The Sun moves in the ecliptic
 328 but the solar γ -ray emission is extended because of cosmic-ray interactions with the solar radiation
 329 field; detectable emission from inverse Compton scattering of cosmic-ray electrons on the radiation
 330 field of the Sun extends several degrees from the Sun (Orlando & Strong 2008; Abdo et al. 2011).
 331 The Moon is not an extended source in this way but the lunar orbit is inclined somewhat relative to
 332 the ecliptic and the Moon moves through a larger fraction of the sky than the Sun. Averaged over
 333 time, the γ -ray emission from the Sun and Moon trace a region around the ecliptic. Without any
 334 correction this can seriously affect the spectra and light curves, so starting with 3FGL we model that
 335 emission.

336 The Sun and Moon emission are modulated by the solar magnetic field which deflects cosmic rays
 337 more (and therefore reduces γ -ray emission) when the Sun is at maximum activity. For that reason
 338 the model used in 3FGL (based on the first 18 months of data when the Sun was near minimum)
 339 was not adequate for 8 years. We used the improved model of the lunar emission (Ackermann et al.
 340 2016a) and a data-based model of the solar disk and inverse Compton scattering on the solar light
 341 (S. Raino, private communication).

342 We combined those models with calculations of their motions and of the exposure of the observations
 343 by the LAT to make templates for the equivalent diffuse component over 8 years using *gtsuntemp*
 344 (Johannesson et al. 2013). For 4FGL we used two different templates: one for the inverse Compton
 345 emission on the solar light (pixel size $0^\circ:25$) and one for the sum of the solar and lunar disks. For the
 346 latter we reduced the pixel size to $0^\circ:125$ to describe the disks accurately, and computed a specific
 347 template for each event type / maximum zenith angle combination of Table 2 (because their exposure
 348 maps are not identical). As in 3FGL those components have no free parameter.

349 2.4.4. *Residual Earth limb template*

350 For 3FGL we reduced the low-energy Earth limb emission by selecting zenith angles less than 100° ,
 351 and modeled the residual contamination approximately. For 4FGL we chose to cut harder on zenith
 352 angle at low energies and select event types with the best PSF (§ 2.3). That procedure eliminates
 353 the need for a specific Earth limb component in the model.

354 3. CONSTRUCTION OF THE CATALOG

355 The procedure used to construct the 4FGL catalog has a number of improvements relative to that
 356 of the 3FGL catalog. In this section we review the procedure, emphasizing what was done differently.
 357 The significances (§ 3.2) and spectral parameters (§ 3.3) of all catalog sources were obtained using

the standard *pyLikelihood* framework (Python analog of *gtlike*) in the LAT Science Tools⁷ (version v11r7p0). The localization procedure (§ 3.1), which relies on *pointlike* (Kerr 2010), provided the source positions, the starting point for the spectral fitting in § 3.2, and a comparison for estimating the reliability of the results (§ 3.7.2).

Throughout the text we denote as RoIs, for Regions of Interest, the regions in which we extract the data. We use the Test Statistic $TS = 2 \log(\mathcal{L}/\mathcal{L}_0)$ (Mattox et al. 1996) to quantify how significantly a source emerges from the background, comparing the maximum value of the likelihood function \mathcal{L} over the RoI including the source in the model with \mathcal{L}_0 , the value without the source. Here and everywhere else in the text \log denotes the natural logarithm.

3.1. Detection and Localization

This section describes the generation of a list of candidate sources, with locations and initial spectral fits. This initial stage uses *pointlike*. Compared with the *gtlike*-based analysis described in § 3.2 to 3.7, it uses the same time range and IRFs, but the partitioning of the sky, the weights, the computation of the likelihood function and its optimization are independent. The zenith angle cut is set to 100° . Energy dispersion is neglected for the sources (we show in § 4.2.2 that it is a small effect). Events below 100 MeV are not useful for source detection and localization, and are ignored at this stage.

3.1.1. Detection settings

The process started with an initial set of sources, from the 8-year FL8Y analysis, including the 75 spatially extended sources listed in § 3.4, and the three-component representation of the Crab (§ 3.3). The same spectral models were considered for each source as in § 3.3, but the favored model (power law, curved, or pulsar-like) was not necessarily the same. The point-source locations were also re-optimized.

The generation of a candidate list of additional sources, with locations and initial spectral fits, is substantially the same as for 3FGL. The sky was partitioned using HEALPix⁸ (Górski et al. 2005) with $N_{\text{side}} = 12$, resulting in 1728 tiles of $\sim 24 \text{ deg}^2$ area. (Note: references to N_{side} in the following refer to HEALPix.) The RoIs included events in cones of 5° radius about the center of the tiles. The data were binned according to energy, 16 energy bands from 100 MeV to 1 TeV (up from 14 bands to 316 GeV in 3FGL), *Front* or *Back* event types, and angular position using HEALPix, but with N_{side} varying from 64 to 4096 according to the PSF. Only *Front* events were used for the two bands below 316 MeV, to avoid the poor PSF and contribution of the Earth limb. Thus the log-likelihood calculation, for each RoI, is a sum over the contributions of 30 energy and event type bands.

All point sources within the RoI and those nearby, such that the contribution to the RoI was at least 1% (out to 11° for the lowest energy band), were included. Only the spectral model parameters for sources within the central tile were allowed to vary to optimize the likelihood. To account for correlations with fixed nearby sources, and a factor of three overlap for the data (each photon contributes to ~ 3 RoIs), the following iteration process was followed. All 1728 RoIs were optimized independently. Then the process was repeated, until convergence, for all RoIs for which the log-likelihood had changed by more than 10. Their nearest neighbors (presumably affected by the modified sources) were iterated as well.

⁷ See <http://fermi.gsfc.nasa.gov/ssc/data/analysis/documentation/Cicerone/>.

⁸ <http://healpix.sourceforge.net>.

398 Another difference from 3FGL was that the diffuse contributions were adjusted globally. We fixed
 399 the isotropic diffuse source to be actually constant over the sky, but globally refit its spectrum
 400 up to 10 GeV, since point-source fits are insensitive to diffuse energies above this. The Galactic
 401 diffuse emission component also was treated quite differently. Starting with a version of the Galactic
 402 diffuse model (§ 2.4.1) without its non-template diffuse γ -ray emission, we derived an alternative
 403 adjustment by optimizing the Galactic diffuse normalization for each RoI and the eight bands below
 404 10 GeV. These values were turned into an 8-layer map which was smoothed, then applied to the
 405 PSF-convolved diffuse model predictions for each band. Then the corrections were remeasured. This
 406 process converged after two iterations, such that no further corrections were needed. The advantage
 407 of the procedure, compared to fitting the diffuse spectral parameters in each RoI (§ 3.2), is that the
 408 effective predictions do not vary abruptly from an RoI to its neighbors, and are unique for each point.
 409 Also it does not constrain the spectral adjustment to be a power law.

410 After a set of iterations had converged, the localization procedure was applied, and source positions
 411 updated for a new set of iterations. At this stage, new sources were occasionally added using the
 412 residual TS procedure described in § 3.1.2. The detection and localization process resulted in 7841
 413 candidate point sources with $TS > 10$, of which 3179 were new. The fit validation and likelihood
 414 weighting were done as in 3FGL, except that, due to the improved representation of the Galactic
 415 diffuse, the effect of the weighting factor was less severe.

416 The *pointlike* unweighting scheme is slightly different from that described in the 3FGL paper
 417 (§ 3.1.2). A measure of the sensitivity to the Galactic diffuse component is the average count density
 418 for the RoI divided by the peak value of the PSF, N_{diff} , which represents a measure of the diffuse
 419 background under the point source. For the RoI at the Galactic center, and the lowest energy band,
 420 this is 4.15×10^4 counts. We unweight the likelihood for all energy bands by effectively limiting
 421 this implied precision to 2%, corresponding to 2500 counts. As before, we divide the log-likelihood
 422 contribution from this energy band by $\max(1, N_{\text{diff}}/2500)$. For the aforementioned case, this value
 423 is 16.6. A consequence is to increase the spectral fit uncertainty for the lowest energy bins for every
 424 source in the RoI. The value for this unweighting factor was determined by examining the distribution
 425 of the deviations between fluxes fitted in individual energy bins and the global spectral fit (similar to
 426 what is done in § 3.5). The 2% precision was set such that the RMS for the distribution of positive
 427 deviations in the most sensitive lowest energy band was near the statistical expectation. (Negative
 428 deviations are distorted by the positivity constraint, resulting in an asymmetry of the distribution.)

429 An important validation criterion is the all-sky counts residual map. Since the source overlaps and
 430 diffuse uncertainties are most severe at the lowest energy, we present, in Figure 3, the distribution
 431 of normalized residuals per pixel, binned with $N_{\text{side}} = 64$, in the 100 – 177 MeV *Front* energy band.
 432 There are 49,920 such pixels, with data counts varying from 92 to 1.7×10^4 . For $|b| > 10^\circ$, the
 433 agreement with the expected Gaussian distribution is very good, while it is clear that there are
 434 issues along the plane. These are of two types. First, around very strong sources, such as Vela, the
 435 discrepancies are perhaps a result of inadequacies of the simple spectral models used, but the (small)
 436 effect of energy dispersion and the limited accuracy of the IRFs may contribute. Regions along the
 437 Galactic ridge are also evident, a result of the difficulty modeling the emission precisely, the reason
 438 we unweight contributions to the likelihood.

439

3.1.2. Detection of additional sources

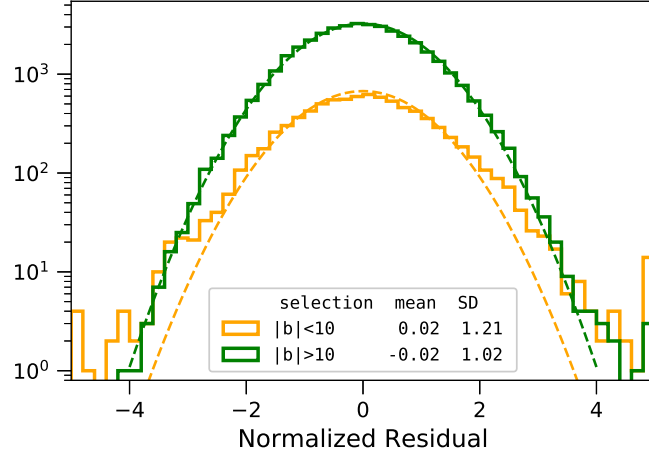


Figure 3. Photon count residuals with respect to the model per $N_{\text{side}} = 64$ bin, for energies 100 – 177 MeV, normalized by the Poisson uncertainty, that is, $(N_{\text{data}} - N_{\text{model}})/\sqrt{N_{\text{model}}}$. Histograms are shown for the values at high latitude ($|b| > 10^\circ$) and low latitude ($|b| < 10^\circ$) (capped at $\pm 5\sigma$). Dashed lines are the Gaussian expectations for the same number of sources. The legend shows the mean and standard deviation for the two subsets.

440 As in 3FGL, the same implementation of the likelihood used for optimizing source parameters was
 441 used to test for the presence of additional point sources. This is inherently iterative, in that the
 442 likelihood is valid to the extent that the model used to calculate it is a fair representation of the
 443 data. Thus, the detection of the faintest sources depends on accurate modeling of all nearby brighter
 444 sources and the diffuse contributions.

445 The FL8Y source list from which this started represented several such additions from the 4-year
 446 3FGL. As before, an iteration starts with choosing a HEALPix $N_{\text{side}} = 512$ grid, 3.1 M points with
 447 average separation 0.15 degrees. But now, instead of testing a single power-law spectrum, we try five
 448 spectral shapes; three are power laws with different indices, two with significant curvature. Table 3
 449 lists the spectral shapes used for the templates. They are shown in Figure 4.

450 For each trial position, and each of the five templates, the normalizations were optimized, and
 451 the resulting TS associated with the pixel. Then, as before, but independently for each template, a
 452 cluster analysis selected groups of pixels with $TS > 16$, as compared to $TS > 10$ for 3FGL. Each
 453 cluster defined a seed, with a position determined by weighting the TS values. Finally, the five sets
 454 of potential seeds were compared and, for those within 1° , the seed with the largest TS was selected
 455 for inclusion.

456 Each candidate was added to its respective RoI, then fully optimized, including localization, during
 457 a full likelihood optimization including all RoIs. The combined results of two iterations of this
 458 procedure, starting from a *pointlike* model including only sources imported from the FL8Y source
 459 list, are summarized in Table 3, which shows the number for each template that was successfully
 460 added to the *pointlike* model, and the number finally included in 4FGL. The reduction is mostly due
 461 to the $TS > 25$ requirement in 4FGL, as applied to the *gtlike* calculation (§ 3.2), which uses different
 462 data and smaller weights. The selection is even stricter ($TS > 34$, § 3.3) for sources with curved
 463 spectra. Several candidates at high significance were not accepted because they were too close to
 464 even brighter sources, or inside extended sources, and thus unlikely to be independent point sources.

Table 3. Spectral shapes for source search

α	β	E_0 (GeV)	Template	Generated	Accepted
1.7	0.0	50.00	Hard	471	101
2.2	0.0	1.00	Intermediate	889	177
2.7	0.0	0.25	Soft	476	84
2.0	0.5	2.00	Peaked	686	151
2.0	0.3	1.00	Pulsar-like	476	84

NOTE—The spectral parameters α , β and E_0 refer to the LogParabola spectral shape (Eq. 2). The last two columns show the number, for each shape, that were successfully added to the *pointlike* model, and the number accepted for the final 4FGL list.

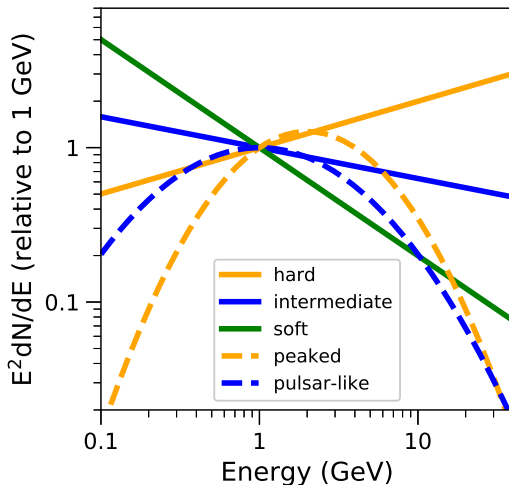


Figure 4. Spectral shape templates used in source finding.

465

3.1.3. Localization

466 The position of each source was determined by maximizing the likelihood with respect to its position
 467 only. That is, all other parameters are kept fixed. The possibility that a shifted position would affect
 468 the spectral models or positions of nearby sources is accounted for by iteration. In the ideal limit
 469 of large statistics the log-likelihood is a quadratic form in any pair of orthogonal angular variables,
 470 assuming small angular offsets. We define LTS, for Localization Test Statistic, to be twice the log
 471 of the likelihood ratio of any position with respect to the maximum; the LTS evaluated for a grid
 472 of positions is called an LTS map. We fit the distribution of LTS to a quadratic form to determine
 473 the uncertainty ellipse (position, major and minor axes, and orientation). The fitting procedure
 474 starts with a prediction of the LTS distribution from the current elliptical parameters. From this,
 475 it evaluates the LTS for eight positions in a circle of a radius corresponding to twice the geometric
 476 mean of the two Gaussian sigmas. We define a measure, the localization quality (LQ), of how well

477 the actual LTS distribution matches this expectation as the sum of squares of differences at those
 478 eight positions. The fitting procedure determines a new set of elliptical parameters from the eight
 479 values. In the ideal case, this is a linear problem and one iteration is sufficient from any starting
 480 point. To account for finite statistics or distortions due to inadequacies of the model, we iterate until
 481 changes are small. The procedure effectively minimizes LQ.

482 We flagged apparently significant sources that do not have good localization fits ($LQ > 8$) with Flag
 483 9 (§ 3.7.3) and for them estimated the position and uncertainty by performing a moment analysis of
 484 an LTS map instead of fitting a quadratic form. Some sources that did not have a well-defined peak
 485 in the likelihood were discarded by hand, on the consideration that they were most likely related to
 486 residual diffuse emission. Another possibility is that two adjacent sources produce a dumbbell-like
 487 shape; for a few of these cases we added a new source by hand.

488 As in 3FGL, we checked the sources spatially associated with 984 AGN counterparts, comparing
 489 their locations with the well-measured positions of the counterparts. Better statistics allowed
 490 examination of the distributions of the differences separately for bright, dim, and moderate-brightness
 491 sources. From this we estimate the absolute precision Δ_{abs} (at the 95% confidence level) more
 492 accurately at $\sim 0^{\circ}0068$, up from $\sim 0^{\circ}005$ in 3FGL. The systematic factor f_{rel} was 1.06, slightly up
 493 from 1.05 in 3FGL. Eq. 1 shows how the statistical errors Δ_{stat} are transformed into total errors Δ_{tot} :

$$\Delta_{\text{tot}}^2 = (f_{\text{rel}} \Delta_{\text{stat}})^2 + \Delta_{\text{abs}}^2 \quad (1)$$

494 which is applied to both ellipse axes.

495

3.2. Significance and Thresholding

496 The framework for this stage of the analysis is inherited from the 3FGL catalog. It splits the sky
 497 into RoIs, varying typically half a dozen sources near the center of the RoI at the same time. Each
 498 source is entered into the fit with the spectral shape and parameters obtained by *pointlike* (§ 3.1),
 499 the brightest sources first. Soft sources from *pointlike* within $0^{\circ}2$ of bright ones were intentionally
 500 deleted. They appear because the simple spectral models we use are not sufficient to account for the
 501 spectra of bright sources, but including them would bias the spectral parameters. There are 1748
 502 RoIs for 4FGL, listed in the ROIs extension of the catalog (Appendix A). The global best fit is reached
 503 iteratively, injecting the spectra of sources in the outer parts of the RoI from the previous step or
 504 iteration. In this approach, the diffuse emission model (§ 2.4) is taken from the global templates
 505 (including the spectrum, unlike what is done with *pointlike* in § 3.1) but it is modulated in each RoI
 506 by three parameters: normalization (at 1 GeV) and small corrective slope of the Galactic component,
 507 and normalization of the isotropic component.

508 Among the more than 8,000 seeds coming from the localization stage, we keep only sources with
 509 $TS > 25$, corresponding to a significance of just over 4σ evaluated from the χ^2 distribution with 4
 510 degrees of freedom (position and spectral parameters of a power-law source, [Mattox et al. 1996](#)). The
 511 model for the current RoI is readjusted after removing each seed below threshold. The low-energy
 512 flux of the seeds below threshold (a fraction of which are real sources) can be absorbed by neighboring
 513 sources closer than the PSF radius. As in 3FGL, we manually added known LAT pulsars that could
 514 not be localized by the automatic procedure without phase selection. However none of those reached
 515 $TS > 25$ in 4FGL.

516 We introduced a number of improvements with respect to 3FGL (by decreasing order of
 517 importance):

- 518 1. In 3FGL we had already noted that systematic errors due to an imperfect modeling of diffuse
519 emission were larger than statistical errors in the Galactic plane, and at the same level over
520 the entire sky. With twice as much exposure and an improved effective area at low energy
521 with Pass 8, the effect now dominates. The approach adopted in 3FGL (comparing runs
522 with different diffuse models) allowed characterizing the effect globally and flagging the worst
523 offenders, but left purely statistical errors on source parameters. In 4FGL we introduce weights
524 in the maximum likelihood approach (Appendix B). This allows obtaining directly (although in
525 an approximate way) smaller TS and larger parameter errors, reflecting the level of systematic
526 uncertainties. We estimated the relative spatial and spectral residuals in the Galactic plane
527 where the diffuse emission is strongest. The resulting systematic level $\epsilon \sim 3\%$ was used to
528 compute the weights. This is by far the most important improvement, which avoids reporting
529 many dubious soft sources.
- 530 2. The automatic iteration procedure at the next-to-last step of the process was improved. There
531 are now two iteration levels. In a standard iteration the sources and source models are fixed
532 and only the parameters are free. An RoI and all its neighbors are run again until $\log \mathcal{L}$ does
533 not change by more than 10 from the previous iteration. Around that we introduce another
534 iteration level (superiterations). At the first iteration of a given superiteration we reenter all
535 seeds and remove (one by one) those with $TS < 16$. We also systematically check a curved
536 spectral shape versus a power-law fit to each source at this first iteration, and keep the curved
537 spectral shape if the fit is significantly better (§ 3.3). At the end of a superiteration an RoI
538 (and its neighbors) enters the next superiteration until $\log \mathcal{L}$ does not change by more than 10
539 from the last iteration of the previous superiteration. This procedure stabilizes the spectral
540 shapes, particularly in the Galactic plane. Seven superiterations were required to reach full
541 convergence.
- 542 3. The fits are now performed from 50 MeV to 1 TeV, and the overall significances (`Signif_Avg`)
543 as well as the spectral parameters refer to the full band. The total energy flux, on the other
544 hand, is still reported between 100 MeV and 100 GeV. For hard sources with photon index less
545 than 2 integrating up to 1 TeV would result in much larger uncertainties. The same is true for
546 soft sources with photon index larger than 2.5 when integrating down to 50 MeV.
- 547 4. We considered the effect of energy dispersion in the approximate way implemented in the
548 Science Tools. The effect of energy dispersion is calculated globally for each source, and applied
549 to the whole 3D model of that source, rather than accounting for energy dispersion separately
550 in each pixel. This approximate rescaling captures the main effect (which is only a small
551 correction, see § 4.2.2) at a very minor computational cost. In evaluating the likelihood function,
552 the effects of energy dispersion were not applied to the isotropic background and the Sun/Moon
553 components whose spectra were obtained from the data without considering energy dispersion.
- 554 5. We used smaller RoIs at higher energy because we are interested in the core region only, which
555 contains the sources whose parameters come from that RoI (sources in the outer parts of the
556 RoI are entered only as background). The core region is the same for all energy intervals, and
557 the RoI is obtained by adding a ring to that core region, whose width adapts to the PSF and
558 therefore decreases with energy (Table 2). This does not significantly affect the result because

the outer parts of the RoI would not have been correlated to the inner sources at high energy anyway, but saves memory and CPU time.

6. At the last step of the fitting procedure we tested all spectral shapes described in § 3.3 (including log-normal for pulsars and cutoff power law for other sources), readjusting the parameters (but not the spectral shapes) of neighboring sources.

We used only binned likelihood analysis in 4FGL because unbinned mode is much more CPU intensive, and does not support weights or energy dispersion. We split the data into fifteen components, selected according to PSF event type and described in Table 2. As explained in § 2.4.4 at low energy we kept only the event types with the best PSF. Each event type selection has its own isotropic diffuse template (because it includes residual charged-particle background, which depends on event type). A single component is used above 10 GeV to save memory and CPU time: at high energy the background under the PSF is small, so keeping the event types separate does not markedly improve significance; it would help for localization, but this is done separately (§ 3.1.3).

A known inconsistency in acceptance exists between Pass 8 PSF event types. It is easy to see on bright sources or the entire RoI spectrum and peaks at the level of 10% between PSF0 (positive residuals, underestimated effective area) and PSF3 (negative residuals, overestimated effective area) at a few GeV. In that range all event types were considered so the effect on source spectra average out. Below 1 GeV the PSF0 event type was discarded but the discrepancy is lower at low energy. We checked by comparing with preliminary corrected IRFs that the energy fluxes indeed tend to be underestimated, but by only 3%. The bias on power-law index is less than 0.01.

3.3. Spectral Shapes

The spectral representation of sources largely follows what was done in 3FGL, considering three spectral models (power law, power law with subexponential cutoff, and log-normal). We changed two important aspects of how we parametrize the cutoff power law:

- The cutoff energy was replaced by an exponential factor (a in Eq. 4) which is allowed to be positive. This makes the simple power law a special case of the cutoff power law and allows fitting that model to all sources, even those with negligible curvature.
- We set the exponential index (b in Eq. 4) to $2/3$ (instead of 1) for all pulsars that are too faint for it to be left free. This recognizes the fact that $b < 1$ (subexponential) in all six bright pulsars that have b free in 4FGL. Three have $b \sim 0.55$ and three have $b \sim 0.75$. We chose $2/3$ as a simple intermediate value.

For all three spectral representations in 4FGL, the normalization (flux density K) is defined at a reference energy E_0 chosen such that the error on K is minimal. E_0 appears as `Pivot_Energy` in the FITS table version of the catalog (Appendix A). The 4FGL spectral forms are thus:

- a log-normal representation (`LogParabola` under `SpectrumType` in the FITS table) for all significantly curved spectra except pulsars, 3C 454.3 and the Small Magellanic Cloud (SMC):

$$\frac{dN}{dE} = K \left(\frac{E}{E_0} \right)^{-\alpha - \beta \log(E/E_0)}. \quad (2)$$

The parameters K , α (spectral slope at E_0) and the curvature β appear as `LP_Flux_Density`, `LP_Index` and `LP_beta` in the FITS table, respectively. No significantly negative β (spectrum

597 curved upwards) was found. The maximum allowed β was set to 1 as in 3FGL. Those parameters
 598 were used for fitting because they allow minimizing the correlation between K and the other
 599 parameters, but a more natural representation would use the peak energy E_{peak} at which the
 600 spectrum is maximum (in νF_ν representation)

$$E_{\text{peak}} = E_0 \exp\left(\frac{2 - \alpha}{2\beta}\right). \quad (3)$$

- 601 • a subexponentially cutoff power law for all significantly curved pulsars (`PLSuperExpCutoff`
 602 under `SpectrumType` in the FITS table):

$$\frac{dN}{dE} = K \left(\frac{E}{E_0}\right)^{-\Gamma} \exp(a(E_0^b - E^b)) \quad (4)$$

603 where E_0 and E in the exponential are expressed in MeV. The parameters K , Γ (low-
 604 energy spectral slope), a (exponential factor in MeV^{-b}) and b (exponential index) appear as
 605 `PLEC_Flux_Density`, `PLEC_Index`, `PLEC_Expfactor` and `PLEC_Exp_Index` in the FITS table,
 606 respectively. Note that in the Science Tools that spectral shape is called `PLSuperExpCutoff2`
 607 and no E_0^b term appears in the exponential, so the error on K (`Unc_PLEC_Flux_Density` in the
 608 FITS table) was obtained from the covariance matrix. The minimum Γ was set to 0 (in 3FGL
 609 it was set to 0.5, but a smaller b results in a smaller Γ). No significantly negative a (spectrum
 610 curved upwards) was found.

- 611 • a simple power-law form (Eq. 4 without the exponential term) for all sources not significantly
 612 curved. For those parameters K and Γ appear as `PL_Flux_Density` and `PL_Index` in the FITS
 613 table.

614 The power law is a mathematical model that is rarely sustained by astrophysical sources over as
 615 broad a band as 50 MeV to 1 TeV. All bright sources in 4FGL are actually significantly curved
 616 downwards. Another drawback of the power-law model is that it tends to exceed the data at both
 617 ends of the spectrum, where constraints are weak. It is not a worry at high energy, but at low
 618 energy (broad PSF) the collection of faint sources modeled as power laws generates an effectively
 619 diffuse excess in the model, which will make the curved sources more curved than they should be.
 620 Using a `LogParabola` spectral shape for all sources would be physically reasonable, but the very large
 621 correlation between sources at low energy due to the broad PSF makes that unstable.

622 We use the curved representation in the global model (used to fit neighboring sources) if $TS_{\text{curv}} > 9$
 623 (3σ significance) where $TS_{\text{curv}} = 2 \log(\mathcal{L}(\text{curved spectrum})/\mathcal{L}(\text{power-law}))$. This is a step down from
 624 3FGL or FL8Y, where the threshold was at 16, or 4σ , while preserving stability. The curvature
 625 significance is reported as `LP_SigCurv` or `PLEC_SigCurv`, replacing the former unique `Signif_Curve`
 626 column of 3FGL. Both values were derived from TS_{curv} and corrected for systematic uncertainties on
 627 the effective area following Eq. 3 of 3FGL. As a result, 52 `LogParabola` sources (with $TS_{\text{curv}} > 9$)
 628 have `LP_SigCurv` less than 3.

629 Sources with curved spectra are considered significant whenever $TS > 25 + 9 = 34$. This is similar
 630 to the 3FGL criterion, which requested $TS > 25$ in the power-law representation, but accepts a few
 631 more strongly curved faint sources (pulsar-like).

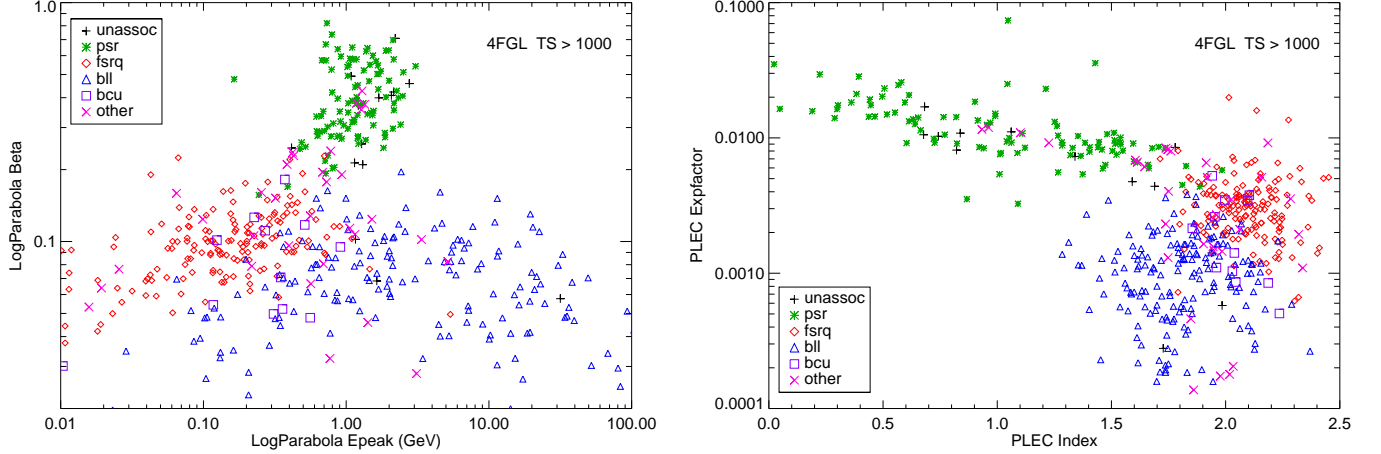


Figure 5. Spectral parameters of all bright sources ($TS > 1000$). The different source classes (§ 6) are depicted by different symbols and colors. Left: log-normal shape parameters E_{peak} (Eq. 3) and β . Right: subexponentially cutoff power-law shape parameters Γ and a (Eq. 4).

632 One more pulsar (PSR J1057–5226) was fit with a free exponential index, besides the six sources
 633 modeled in this way in 3FGL. The Crab was modeled with three spectral components as in 3FGL,
 634 but the inverse Compton emission of the nebula (now an extended source, § 3.4) was represented as a
 635 log-normal instead of a simple power law. The parameters of that component were fixed to $\alpha = 1.75$,
 636 $\beta = 0.08$, $K = 5.5 \times 10^{-13}$ ph cm $^{-2}$ MeV $^{-1}$ s $^{-1}$ at 10 GeV, mimicking the broken power-law fit by
 637 Buehler et al. (2012). They were unstable (too much correlation with the pulsar) without phase
 638 selection. Four extended sources had fixed parameters in 3FGL. The parameters in these sources
 639 (Vela X, MSH 15–52, γ Cygni and the Cygnus X cocoon) were freed in 4FGL.

640 Overall in 4FGL seven sources (the six brightest pulsars and 3C 454.3) were fit as `PLSuperExpCutoff`
 641 with free b (Eq. 4), 215 pulsars were fit as `PLSuperExpCutoff` with $b = 2/3$, the SMC was fit as
 642 `PLSuperExpCutoff` with $b = 1$, 1332 sources were fit as `LogParabola` (including the fixed inverse
 643 Compton component of the Crab and 38 other extended sources) and the rest were represented as
 644 power laws. The larger fraction of curved spectra compared to 3FGL is due to the lower TS_{curv}
 645 threshold.

646 The way the parameters are reported has changed as well:

- 647 • The spectral shape parameters are now explicitly associated to the spectral model they come
 648 from. They are reported as `Shape_Param` where `Shape` is one of `PL` (`PowerLaw`), `PLEC`
 649 (`PLSuperExpCutoff`) or `LP` (`LogParabola`) and `Param` is the parameter name. Columns
 650 `Shape_Index` replace `Spectral_Index` which was ambiguous.
- 651 • All sources were fit with the three spectral shapes, so all fields are filled. The curvature
 652 significance is calculated twice by comparing power law with both log-normal and exponentially
 653 cutoff power law (although only one is actually used to switch to the curved shape in the
 654 global model, depending on whether the source is a pulsar or not). There are also three
 655 `Shape_Flux_Density` columns referring to the same `Pivot_Energy`. The preferred spectral
 656 shape (reported as `SpectrumType`) remains what is used in the global model, when the source

is part of the background (i.e., when fitting the other sources). It is also what is used to derive the fluxes, their uncertainties and the significance.

This additional information allows comparing unassociated sources with either pulsars or blazars using the same spectral shape. This is illustrated on Figure 5. Pulsar spectra are more curved than AGN, and among AGN flat-spectrum radio quasars (FSRQ) peak at lower energy than BL Lacs (BLL). It is clear that when the error bars are small (bright sources) any of those plots is very discriminant for classifying sources. They complement the variability versus curvature plot (Figure 8 of the 1FGL paper). We expect most of the (few) bright remaining unassociated sources (black plus signs) to be pulsars, from their location on those plots. The same reasoning implies that most of the unclassified blazars (bcu) should be flat-spectrum radio quasars, although the distinction with BL Lacs is less clear-cut than with pulsars. Unfortunately most unassociated sources are faint ($TS < 100$) and for those the same plots are very confused, because the error bars become comparable to the ranges of parameters.

3.4. Extended Sources

As in the 3FGL catalog, we explicitly model as spatially extended those LAT sources that have been shown in dedicated analyses to be spatially resolved by the LAT. The catalog process does not involve looking for new extended sources, testing possible extension of sources detected as point-like, nor refitting the spatial shapes of known extended sources.

Most templates are geometrical, so they are not perfect matches to the data and the source detection often finds residuals on top of extended sources, which are then converted into additional point sources. As in 3FGL those additional point sources were intentionally deleted from the model, except if they met two of the following criteria: associated with a plausible counterpart known at other wavelengths, much harder than the extended source (`Pivot_Energy` larger by a factor e or more), or very significant ($TS > 100$). Contrary to 3FGL, that procedure was applied inside the Cygnus X cocoon as well.

The latest compilation of extended *Fermi*-LAT sources prior to this work consists of the 55 extended sources entered in the 3FHL catalog of sources above 10 GeV (Ajello et al. 2017). This includes the result of the systematic search for new extended sources in the Galactic plane ($|b| < 7^\circ$) above 10 GeV (FGES, Ackermann et al. 2017b). Two of those were not propagated to 4FGL:

- FGES J1800.5–2343 was replaced by the W 28 template from 3FGL, and the nearby excesses (Hanabata et al. 2014) were left to be modeled as point sources.
- FGES J0537.6+2751 was replaced by the radio template of S 147 used in 3FGL, which fits better than the disk used in the FGES paper (S 147 is a soft source, so it was barely detected above 10 GeV).

The supernova remnant (SNR) MSH 15-56 was replaced by two morphologically distinct components, following Devin et al. (2018): one for the SNR (SNR mask in the paper), the other one for the pulsar wind nebula (PWN) inside it (radio template). We added back the W 30 SNR on top of FGES J1804.7–2144 (coincident with HESS J1804–216). The two overlap but the best localization clearly moves with energy from W 30 to HESS J1804–216.

Eighteen sources were added, resulting in 75 extended sources in 4FGL:

- 697 • The Rosette nebula and Monoceros SNR (too soft to be detected above 10 GeV) were
698 characterized by [Katagiri et al. \(2016b\)](#). We used the same templates.
- 699 • The systematic search for extended sources outside the Galactic plane above 1 GeV (FHES,
700 [Ackermann et al. 2018](#)) found sixteen reliable extended sources. Three of them were already
701 known as extended sources. Two were extensions of the Cen A lobes, which appear larger in γ
702 rays than the WMAP template that we use following [Abdo et al. \(2010b\)](#). We did not consider
703 them, waiting for a new morphological analysis of the full lobes. We ignored two others: M 31
704 (extension only marginally significant, both in FHES and [Ackermann et al. 2017a](#)) and CTA
705 1 (SNR G119.5+10.2) around PSR J0007+7303 (not significant without phase gating). We
706 introduced the nine remaining FHES sources, including the inverse Compton component of the
707 Crab nebula and the ρ Oph star-forming region (= FHES J1626.9–2431). One of them (FHES
708 J1741.6–3917) was reported by [Araya \(2018a\)](#) as well, with similar extension.
- 709 • Four HESS sources were found to be extended sources in the *Fermi*-LAT range as well: HESS
710 J1534–571 ([Araya 2017](#)), HESS J1808–204 ([Yeung et al. 2016](#)), HESS J1809–193 and HESS
711 J1813–178 ([Araya 2018b](#)).
- 712 • Three extended sources were discovered in the search for GeV emission from magnetars ([Li
713 et al. 2017a](#)). They contain SNRs (Kes 73, Kes 79 and G42.8+0.6) but are much bigger than
714 the radio SNRs. One of them (around Kes 73) was also noted by [Yeung et al. \(2017\)](#).

715 Table 4 lists the source name, origin, spatial template and the reference for the dedicated analysis.
716 These sources are tabulated with the point sources, with the only distinction being that no position
717 uncertainties are reported and their names end in e (see Appendix A). Unidentified point sources
718 inside extended ones are indicated as “xxx field” in the ASSOC2 column of the catalog.

Table 4. Extended Sources Modeled in the 4FGL Analysis

4FGL Name	Extended Source	Origin	Spatial Form	Extent [deg]	Reference
J0058.0–7245e	SMC Galaxy	Updated	Map	1.5	Caputo et al. (2016)
J0221.4+6241e	HB 3	New	Disk	0.8	Katagiri et al. (2016a)
J0222.4+6156e	W 3	New	Map	0.6	Katagiri et al. (2016a)
J0322.6–3712e	Fornax A	3FHL	Map	0.35	Ackermann et al. (2016c)
J0427.2+5533e	SNR G150.3+4.5	3FHL	Disk	1.515	Ackermann et al. (2017b)
J0500.3+4639e	HB 9	New	Map	1.0	Araya (2014)
J0500.9–6945e	LMC FarWest	3FHL	Map ^a	0.9	Ackermann et al. (2016d)
J0519.9–6845e	LMC Galaxy	New	Map ^a	3.0	Ackermann et al. (2016d)
J0530.0–6900e	LMC 30DorWest	3FHL	Map ^a	0.9	Ackermann et al. (2016d)
J0531.8–6639e	LMC North	3FHL	Map ^a	0.6	Ackermann et al. (2016d)
J0534.5+2201e	Crab nebula IC	New	Gaussian	0.03	Ackermann et al. (2018)
J0540.3+2756e	S 147	3FGL	Disk	1.5	Katsuta et al. (2012)
J0617.2+2234e	IC 443	2FGL	Gaussian	0.27	Abdo et al. (2010c)
J0634.2+0436e	Rosette	New	Map	(1.5, 0.875)	Katagiri et al. (2016b)
J0639.4+0655e	Monoceros	New	Gaussian	3.47	Katagiri et al. (2016b)
J0822.1–4253e	Puppis A	3FHL	Disk	0.443	Ackermann et al. (2017b)
J0833.1–4511e	Vela X	2FGL	Disk	0.91	Abdo et al. (2010d)

Table 4 continued on next page

Table 4 (*continued*)

4FGL Name	Extended Source	Origin	Spatial Form	Extent [deg]	Reference
J0851.9–4620e	Vela Junior	3FHL	Disk	0.978	Ackermann et al. (2017b)
J1023.3–5747e	Westerlund 2	3FHL	Disk	0.278	Ackermann et al. (2017b)
J1036.3–5833e	FGES J1036.3–5833	3FHL	Disk	2.465	Ackermann et al. (2017b)
J1109.4–6115e	FGES J1109.4–6115	3FHL	Disk	1.267	Ackermann et al. (2017b)
J1208.5–5243e	SNR G296.5+10.0	3FHL	Disk	0.76	Acero et al. (2016b)
J1213.3–6240e	FGES J1213.3–6240	3FHL	Disk	0.332	Ackermann et al. (2017b)
J1303.0–6312e	HESS J1303–631	3FGL	Gaussian	0.24	Aharonian et al. (2005)
J1324.0–4330e	Centaurus A (lobes)	2FGL	Map	(2.5, 1.0)	Abdo et al. (2010b)
J1355.1–6420e	HESS J1356–645	3FHL	Disk	0.405	Ackermann et al. (2017b)
J1409.1–6121e	FGES J1409.1–6121	3FHL	Disk	0.733	Ackermann et al. (2017b)
J1420.3–6046e	HESS J1420–607	3FHL	Disk	0.123	Ackermann et al. (2017b)
J1443.0–6227e	RCW 86	3FHL	Map	0.3	Ajello et al. (2016)
J1501.0–6310e	FHES J1501.0–6310	New	Gaussian	1.29	Ackermann et al. (2018)
J1507.9–6228e	HESS J1507–622	3FHL	Disk	0.362	Ackermann et al. (2017b)
J1514.2–5909e	MSH 15–52	3FHL	Disk	0.243	Ackermann et al. (2017b)
J1533.9–5712e	HESS J1534–571	New	Disk	0.4	Araya (2017)
J1552.4–5612e	MSH 15–56 PWN	New	Map	0.08	Devin et al. (2018)
J1552.9–5607e	MSH 15–56 SNR	New	Map	0.3	Devin et al. (2018)
J1553.8–5325e	FGES J1553.8–5325	3FHL	Disk	0.523	Ackermann et al. (2017b)
J1615.3–5146e	HESS J1614–518	3FGL	Disk	0.42	Lande et al. (2012)
J1616.2–5054e	HESS J1616–508	3FGL	Disk	0.32	Lande et al. (2012)
J1626.9–2431e	FHES J1626.9–2431	New	Gaussian	0.29	Ackermann et al. (2018)
J1631.6–4756e	FGES J1631.6–4756	3FHL	Disk	0.256	Ackermann et al. (2017b)
J1633.0–4746e	FGES J1633.0–4746	3FHL	Disk	0.61	Ackermann et al. (2017b)
J1636.3–4731e	SNR G337.0–0.1	3FHL	Disk	0.139	Ackermann et al. (2017b)
J1642.1–5428e	FHES J1642.1–5428	New	Disk	0.696	Ackermann et al. (2018)
J1652.2–4633e	FGES J1652.2–4633	3FHL	Disk	0.718	Ackermann et al. (2017b)
J1655.5–4737e	FGES J1655.5–4737	3FHL	Disk	0.334	Ackermann et al. (2017b)
J1713.5–3945e	RX J1713.7–3946	3FHL	Map	0.56	H. E. S. S. Collaboration et al. (2018a)
J1723.5–0501e	FHES J1723.5–0501	New	Gaussian	0.73	Ackermann et al. (2018)
J1741.6–3917e	FHES J1741.6–3917	New	Disk	1.65	Ackermann et al. (2018)
J1745.8–3028e	FGES J1745.8–3028	3FHL	Disk	0.528	Ackermann et al. (2017b)
J1801.3–2326e	W 28	2FGL	Disk	0.39	Abdo et al. (2010e)
J1804.7–2144e	HESS J1804–216	3FHL	Disk	0.378	Ackermann et al. (2017b)
J1805.6–2136e	W 30	2FGL	Disk	0.37	Ajello et al. (2012)
J1808.2–2028e	HESS J1808–204	New	Disk	0.65	Yeung et al. (2016)
J1810.3–1925e	HESS J1809–193	New	Disk	0.5	Araya (2018b)
J1813.1–1737e	HESS J1813–178	New	Disk	0.6	Araya (2018b)
J1824.5–1351e	HESS J1825–137	2FGL	Gaussian	0.75	Grondin et al. (2011)
J1834.1–0706e	SNR G24.7+0.6	3FHL	Disk	0.214	Ackermann et al. (2017b)
J1834.5–0846e	W 41	3FHL	Gaussian	0.23	Abramowski et al. (2015)
J1836.5–0651e	FGES J1836.5–0651	3FHL	Disk	0.535	Ackermann et al. (2017b)
J1838.9–0704e	FGES J1838.9–0704	3FHL	Disk	0.523	Ackermann et al. (2017b)
J1840.8–0453e	Kes 73	New	Disk	0.32	Li et al. (2017a)
J1840.9–0532e	HESS J1841–055	3FGL	2D Gaussian	(0.62, 0.38)	Aharonian et al. (2008)
J1852.4+0037e	Kes 79	New	Disk	0.63	Li et al. (2017a)
J1855.9+0121e	W 44	2FGL	2D Ring	(0.30, 0.19)	Abdo et al. (2010f)

Table 4 continued on next page

Table 4 (*continued*)

4FGL Name	Extended Source	Origin	Spatial Form	Extent [deg]	Reference
J1857.7+0246e	HESS J1857+026	3FHL	Disk	0.613	Ackermann et al. (2017b)
J1908.6+0915e	SNR G42.8+0.6	New	Disk	0.6	Li et al. (2017a)
J1923.2+1408e	W 51C	2FGL	2D Disk	(0.375, 0.26)	Abdo et al. (2009b)
J2021.0+4031e	γ Cygni	3FGL	Disk	0.63	Lande et al. (2012)
J2028.6+4110e	Cygnus X cocoon	3FGL	Gaussian	3.0	Ackermann et al. (2011a)
J2045.2+5026e	HB 21	3FGL	Disk	1.19	Pivato et al. (2013)
J2051.0+3040e	Cygnus Loop	2FGL	Ring	1.65	Katagiri et al. (2011)
J2129.9+5833e	FHES J2129.9+5833	New	Gaussian	1.09	Ackermann et al. (2018)
J2208.4+6443e	FHES J2208.4+6443	New	Gaussian	0.93	Ackermann et al. (2018)
J2301.9+5855e	CTB 109	3FHL	Disk	0.249	Ackermann et al. (2017b)
J2304.0+5406e	FHES J2304.0+5406	New	Gaussian	1.58	Ackermann et al. (2018)

^aEmissivity model.

NOTE— List of all sources that have been modeled as spatially extended. The Origin column gives the name of the *Fermi*-LAT catalog in which that spatial template was introduced. The Extent column indicates the radius for Disk (flat disk) sources, the 68% containment radius for Gaussian sources, the outer radius for Ring (flat annulus) sources, and an approximate radius for Map (external template) sources. The 2D shapes are elliptical; each pair of parameters (a, b) represents the semi-major (a) and semi-minor (b) axes.

719

3.5. Flux Determination

720 Thanks to the improved statistics, the source photon fluxes in 4FGL are reported in seven energy
721 bands (1: 50 to 100 MeV; 2: 100 to 300 MeV; 3: 300 MeV to 1 GeV; 4: 1 to 3 GeV; 5: 3 to 10 GeV; 6:
722 10 to 30 GeV; 7: 30 to 300 GeV) extending both below and above the range (100 MeV to 100 GeV)
723 covered in 3FGL. Up to 10 GeV, the data files were exactly the same as in the global fit (Table 2).
724 To get the best sensitivity in band 6 (10 to 30 GeV), we split the data into 4 components per event
725 type, using pixel size 0°04 for PSF3, 0°05 for PSF2, 0°1 for PSF1 and 0°2 for PSF0. Above 30 GeV
726 (band 7) we used unbinned likelihood, which is as precise while using much smaller files. It does not
727 allow correcting for energy dispersion, but this is not an important issue in that band. The fluxes
728 were obtained by freezing the power-law index to that obtained in the fit over the full range and
729 adjusting the normalization in each spectral band. For the curved spectra (§ 3.3) the photon index
730 in a band was set to the local spectral slope at the logarithmic mid-point of the band $\sqrt{E_n E_{n+1}}$,
731 restricted to be in the interval [0,5].

732 In each band, the analysis was conducted in the same way as for the 3FGL catalog. To adapt more
733 easily to new band definitions, the results (photon fluxes and uncertainties, νF_ν differential fluxes, and
734 significances) are reported in a set of four vector columns (Appendix A: Flux_Band, Unc_Flux_Band,
735 nuFnu_Band, Sqrt_TS_Band) instead of a set of four columns per band as in previous FGL catalogs.
736 The spectral fit quality is computed in a more precise way than in 3FGL from twice the sum of
737 log-likelihood differences, as we did for the variability index (Sect. 3.6 of the 2FGL paper). The
738 contribution from each band S_i^2 also accounts for systematic uncertainties on effective area via

$$S_i^2 = \frac{2\sigma_i^2}{\sigma_i^2 + (f_i^{\text{rel}} F_i^{\text{fit}})^2} \log \left[\mathcal{L}_i(F_i^{\text{best}}) / \mathcal{L}_i(F_i^{\text{fit}}) \right] \quad (5)$$

739 where i runs over all bands, F_i^{fit} is the flux predicted by the global model, F_i^{best} is the flux fitted to
740 band i alone, σ_i is the statistical error (upper error if $F_i^{\text{best}} \leq F_i^{\text{fit}}$, lower error if $F_i^{\text{best}} > F_i^{\text{fit}}$) and

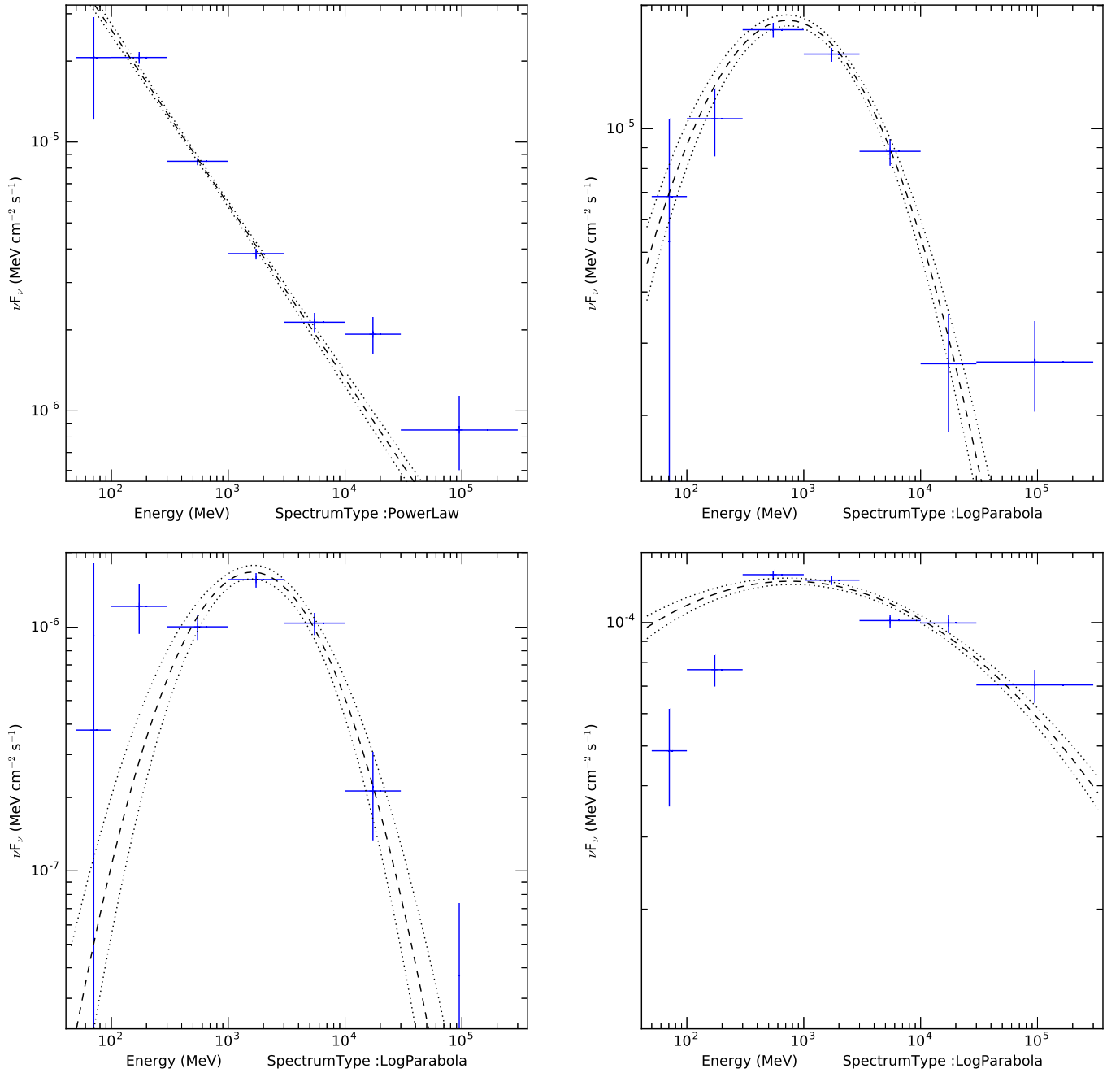


Figure 6. Spectral energy distributions of four sources flagged with bad spectral fit quality (Flag 10 in Table 5). On all plots the dashed line is the best fit from the analysis over the full energy range, and the dotted lines show the uncertainty obtained from the covariance matrix on the spectral parameters. The vertical scale is not the same in all plots. Top left, the Cen A radio galaxy (4FGL J1325.5–4300) fit by a power law with $\Gamma = 2.65$: it is a good representation up to 10 GeV, but the last two points deviate from the power-law fit. Top right, the Large Magellanic Cloud (4FGL J0519.9–6845e): the fitted LogParabola spectrum appears to drop too fast at high energy. Bottom left, the unassociated source 4FGL J0336.0+7502: the low-energy points deviate from the LogParabola fit. Bottom right, the Cygnus X cocoon (4FGL J2028.6+4110e): the deviation from the LogParabola fit at the first two points is probably spurious, due to source confusion

741 the spectral fit quality is simply $\sum_i S_i^2$. The systematic uncertainties⁹ f_i^{rel} are set to 0.15 in the first
 742 band, 0.1 in the second and the last bands, and 0.05 in bands 3 to 6. The uncertainty is larger in
 743 the first band because only PSF3 events are used.

744 Too large values of spectral fit quality are flagged (Flag 10 in Table 5). Since there are 7 bands and
 745 (for most sources, which are fit with the power-law model) 2 free parameters, the flag is set when
 746 $\sum_i S_i^2 > 20.5$ (probability 10^{-3} for a χ^2 distribution with 5 degrees of freedom). Only 6 sources
 747 trigger this. We also set the same flag whenever any individual band is off by more than 3σ ($S_i^2 > 9$).
 748 This occurs in 26 sources. Among the 27 sources flagged with Flag 10 (examples in Figure 6), the
 749 Vela and Geminga pulsars are very bright sources for which our spectral representation is not good
 750 enough. A few show signs of a real second component in the spectrum, such as Cen A (H. E. S. S.
 751 Collaboration et al. 2018b). Several would be better fit by a different spectral model: the Large
 752 Magellanic Cloud (LMC) probably decreases at high energy as a power law like our own Galaxy, and
 753 4FGL J0336.0+7502 is better fit by a PLSuperExpCutoff model. The latter is an unassociated source
 754 at 15° latitude, which has a strongly curved spectrum and is not variable: it is a good candidate
 755 for a millisecond pulsar. Other sources show deviations at low energy and are in confused regions
 756 or close to a brighter neighbor, such as the Cygnus X cocoon. This extended source contains many
 757 point sources inside it and the PSF below 300 MeV is too broad to provide a reliable separation.

758 The fluxes in the 50 to 100 MeV band are very hard to estimate because of the enormous confusion.
 759 The average distance between sources (1.7°) is about equal to the half width at half maximum of
 760 PSF3 events in that band, so it is nearly always possible to set a source to 0 and compensate by a
 761 suitable combination of flux adjustments in its neighbors. This is why only 34 sources have $TS > 25$
 762 in that band (all are bright sources with global $TS > 700$). This is far fewer than the 198 low-energy
 763 (30 - 100 MeV) Fermi-LAT sources reported by Principe et al. (2018, 1FLE). The reason is that in
 764 4FGL we consider that even faint sources in the catalog can have strong low-energy emission, so the
 765 total source flux is distributed over 5000 sources, whereas 1FLE focused on finding individual peaks.

766 At the other extreme, 618 sources have $TS > 25$ in the 30 to 300 GeV band, which is entirely
 767 limited by photon counting ($TS > 25$ in that band corresponds to about 5 events). Only 13 of those
 768 are not associated to a 3FHL or FHES source. The brightest of them (at $TS = 54$ in that band) is
 769 a hard source associated with 1RXS J224123.5+294244, mostly significant in the last year, after the
 770 3FHL time range.

771 As in past FGL catalogs, the photon fluxes between 1 and 100 GeV as well as the energy fluxes
 772 between 100 MeV and 100 GeV were derived from the full-band analysis assuming the best spectral
 773 shape, and their uncertainties come from the covariance matrix. Even though the full analysis is
 774 carried out down to 50 MeV and up to 1 TeV in 4FGL, we have not changed the energy range over
 775 which we quote fluxes so that they can be easily compared with fluxes in past catalogs. The photon
 776 fluxes above 100 GeV are negligible except in the very hardest power-law sources, and the energy
 777 fluxes below 100 MeV and above 100 GeV are not precisely measured (even for soft and hard sources,
 778 respectively).

779 3.6. Variability

780 3.6.1. One-year intervals

⁹ See https://fermi.gsfc.nasa.gov/ssc/data/analysis/LAT_caveats.html.

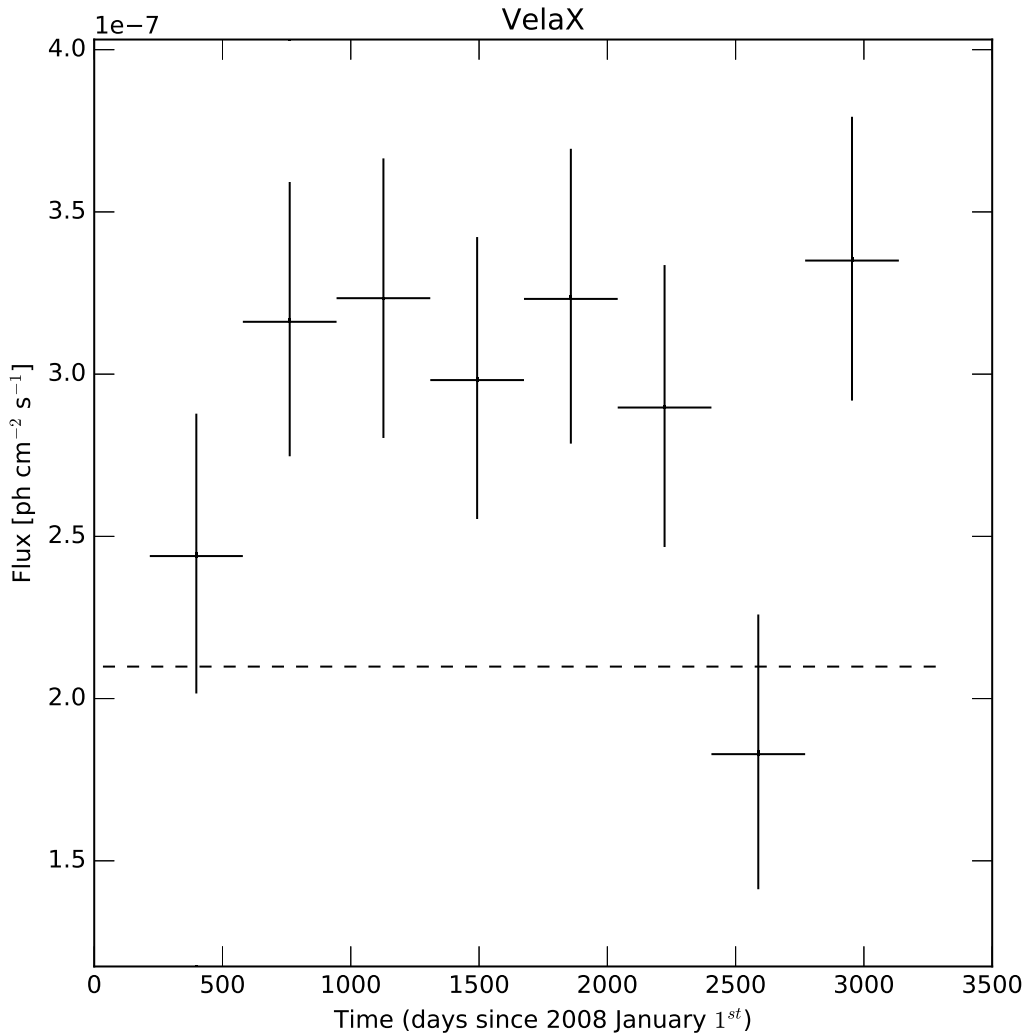


Figure 7. Light curve of Vela X in the 0.1 to 100 GeV band. It is an extended source that should not be variable. Indeed the yearly fluxes are compatible with a constant (the average flux is 2.9×10^{-7} ph cm^{-2} s^{-1}), but not with the flux extracted over the full eight years (dashed line, too low). That inconsistency is due to differences in the data analysis settings between the global fit and the fits per year (the weights in particular). Vela X is very close to the very bright Vela pulsar, so it is strongly attenuated by the weights. For most sources the average flux is much closer to the global flux.

781 We started by computing light curves over 1-year intervals. This is much faster and more stable
 782 than fitting smaller time intervals, and provides a good variability assessment already. We used
 783 binned likelihood and the same data as in the main run up to 10 GeV (Table 2), but to save disk
 784 space and CPU time we merged event types together. Above 10 GeV we used unbinned likelihood
 785 (more efficient when there are few events). We ignored events above 100 GeV (unimportant for
 786 variability).

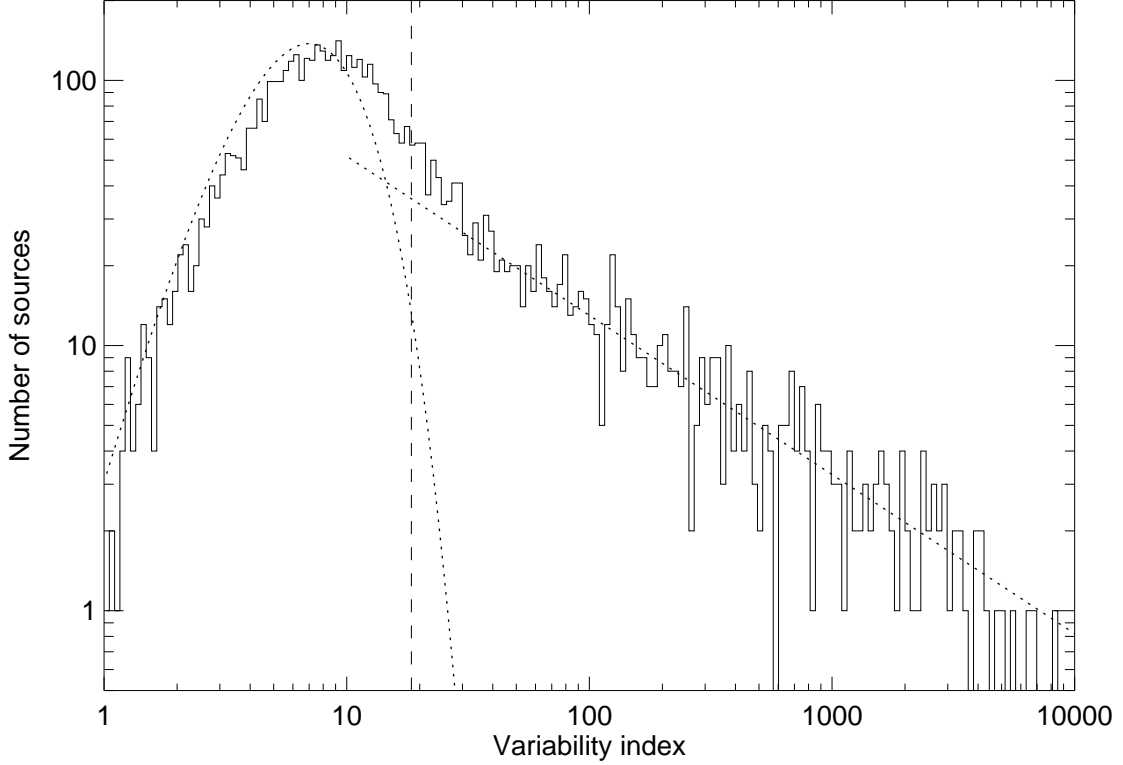


Figure 8. Distribution of the variability index (Eq. 6) over one-year intervals. The dotted line at left is the χ^2 distribution for 7 degrees of freedom, expected for a set of non-variable sources. The dotted line at right is a power-law decreasing as $TS_{\text{var}}^{-0.6}$. The vertical dashed line is the threshold above which we consider that a source is likely variable.

787 As in 3FGL the fluxes in each interval were obtained by freezing the spectral parameters to those
 788 obtained in the fit over the full range and adjusting the normalization. As in previous FGL catalogs,
 789 the fluxes in each interval are reported as photon fluxes between 0.1 and 100 GeV.

790 The weights appropriate for one year were computed using the procedure explained in Appendix B,
 791 entering the same data cube divided by 8 (we use the same weights in each year), and ignoring the
 792 last steps specific to splitting event types. The weights are of course much larger than those for 8
 793 years, but remain a significant correction (the weights are less than 0.2 in the Galactic Ridge up
 794 to 300 MeV). We used the same Sun/Moon model for each year. This amounts to neglecting the
 795 modulation of their intrinsic flux along the 11-year solar cycle.

796 Because of the different weights between the full analysis and that in 1-year intervals, the average
 797 flux from the light curve F_{av} can differ somewhat from the flux in the total analysis F_{glob} (low energies
 798 are less attenuated in the analysis over 1-year intervals). This is illustrated in Figure 7. In 4FGL we
 799 compute the variability index TS_{var} (reported as `Variability_Index` in the FITS file) as

$$TS_{\text{var}} = 2 \sum_i \log [\mathcal{L}_i(F_i) / \mathcal{L}_i(F_{\text{glob}})] - \max(\chi^2(F_{\text{glob}}) - \chi^2(F_{\text{av}}), 0) \quad (6)$$

$$\chi^2(F) = \sum_i \frac{(F_i - F)^2}{\sigma_i^2} \quad (7)$$

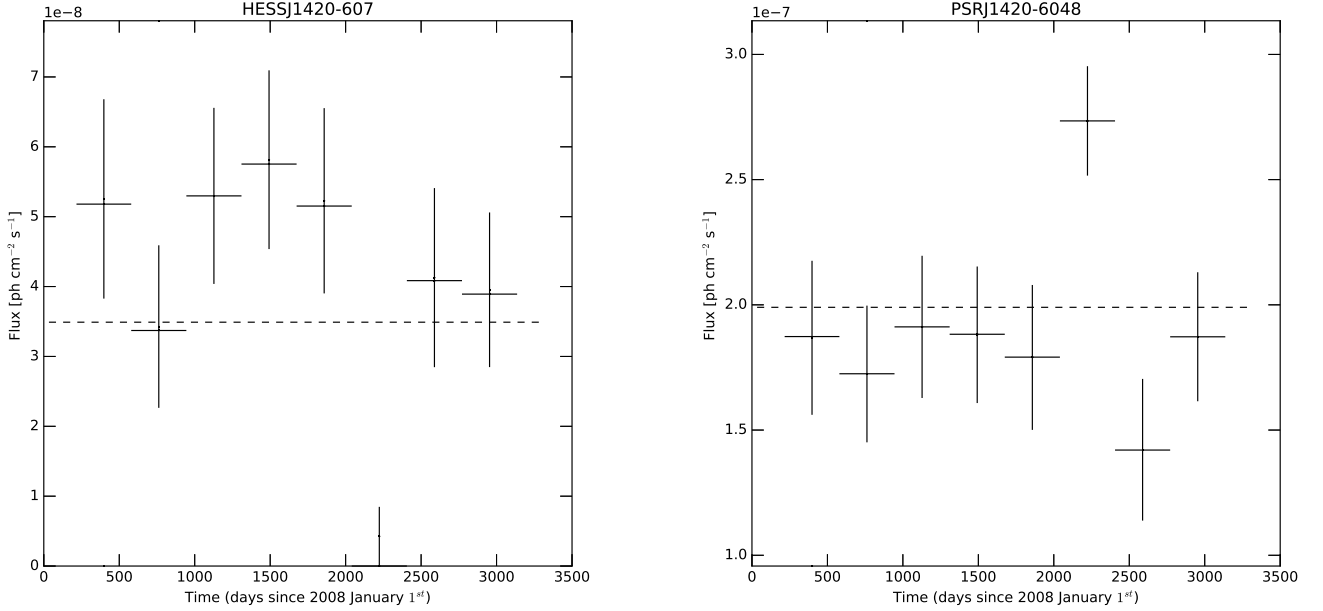


Figure 9. Light curves of the pulsar wind nebula HESS J1420–607 at $TS_{\text{var}} = 23.4$ over one-year intervals and its parent pulsar PSR J1420–6048. The apparent variability of HESS J1420–607 is due to the low point in the 6th year, which corresponds to a high point in the light curve of PSR J1420–6048. This is clearly a case of incorrect flux transfer due to the strong spatial confusion (the nebula is only $0^{\circ}12$ in radius), despite the spectral difference between the two sources. The perturbation of the pulsar (brighter than the nebula) is not enough to exceed the variability threshold.

800 where F_i are the individual flux values, $\mathcal{L}_i(F)$ the likelihood in interval i assuming flux F and σ_i the
 801 errors on F_i (upper error if $F_i \leq F$, lower error if $F_i > F$). The first term in Eq. 6 is the same as
 802 Eq. 4 of 2FGL. The second term corrects (in the Gaussian limit) for the difference between F_{glob} and
 803 F_{av} (since the average flux is known only at the very end, it could not be entered when computing
 804 $\mathcal{L}_i(F)$). We subtract the second term only when it is positive (it is not necessarily positive because
 805 the best χ^2 is reached at the average weighted by σ_i^{-2} , not the straight average). On the other hand,
 806 we did not correct the variability index for the relative systematic error, which is already accounted
 807 for in the weighting procedure.

808 The distribution of observed TS_{var} is shown in Figure 8. It looks like a composite of a power-law
 809 distribution and a $\chi^2(7)$ distribution with $N_{\text{int}} - 1 = 7$ degrees of freedom, where N_{int} is the number
 810 of intervals. The left branch corresponds both to constant sources (such as most pulsars) and sources
 811 too faint to have measurable variability. There are many blazars among them, which are most likely
 812 just as variable as brighter blazars. This contribution of real variability to TS_{var} is the reason why the
 813 histogram is a little offset to the right of the $\chi^2(7)$ distribution (that offset is absent in the Galactic
 814 plane, and stronger off the plane).

815 Variability is considered probable when $TS_{\text{var}} > 18.48$, corresponding to 99% confidence in a $\chi^2(7)$
 816 distribution. We find 1327 variable sources with that criterion. After the χ^2 -based correction of Eq. 6,
 817 Vela X remains below that threshold. One extended source still exceeds the variability threshold.
 818 This is HESS J1420–607 (Figure 9), confused with its parent pulsar PSR J1420–6048. A similar

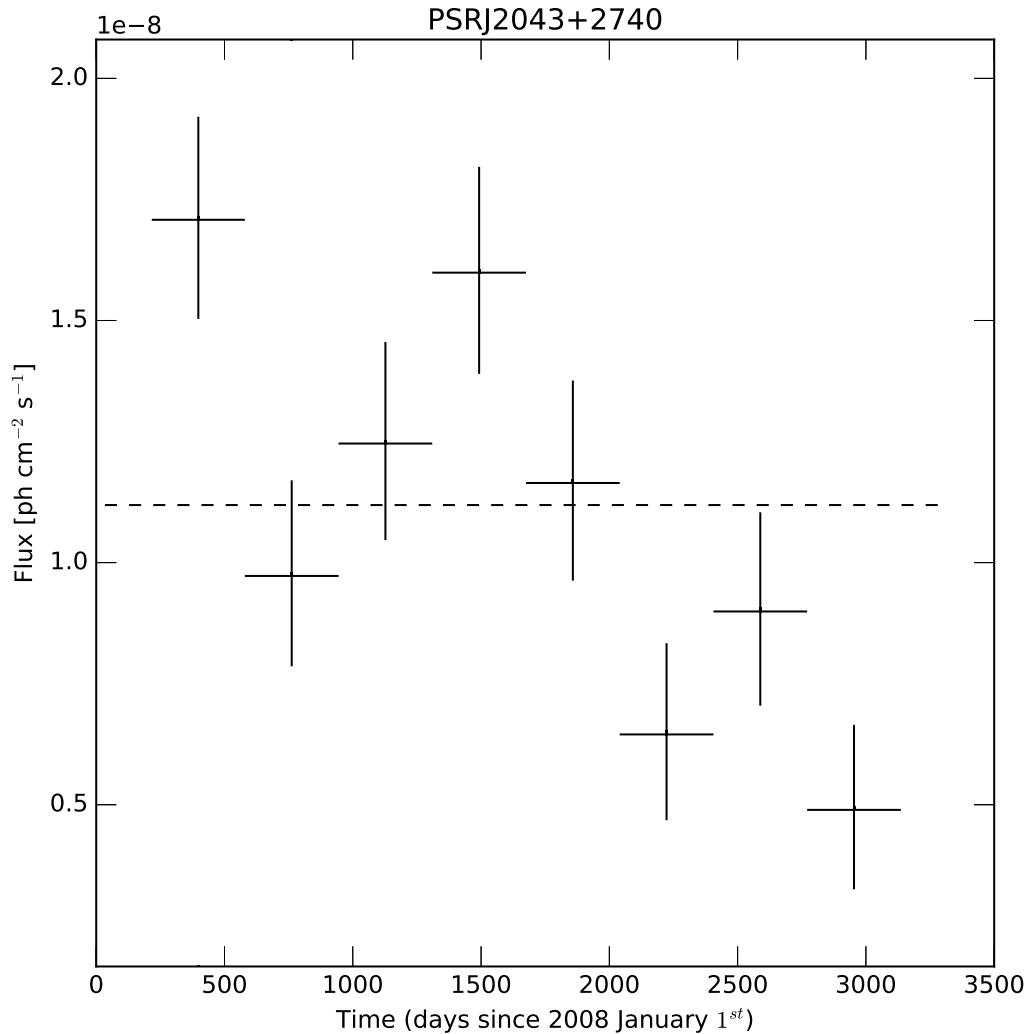


Figure 10. Light curve of the pulsar PSR J2043+2740, at $TS_{\text{var}} = 33$ over one-year intervals. The flux of this pulsar appears to be decreasing secularly.

819 flux transfer occurred in the third year between the Crab pulsar and the Crab Nebula. This can be
 820 understood because the synchrotron emission of the nebula becomes much harder during flares, while
 821 our pipeline assumes the soft power-law fit over the full interval applies throughout. None of those
 822 variabilities are real.

823 Besides the Crab and the known variable pulsars PSR J1227–4853 (Johnson et al. 2015) and PSR
 824 J2021+4026 (Allafort et al. 2013), three other pulsars are above the variability threshold. Two are
 825 just above it and can be chance occurrences (there are more than 200 pulsars, so we expect two
 826 above the 1% threshold). The last one is PSR J2043+2740 (Figure 10), which looks like a case of
 827 real variability (secular flux decrease by a factor of 3).

828 In 4FGL we report the fractional variability of the sources in the FITS file as `Frac_Variability`.
 829 It is defined for each source from the excess variance on top of the statistical and systematic

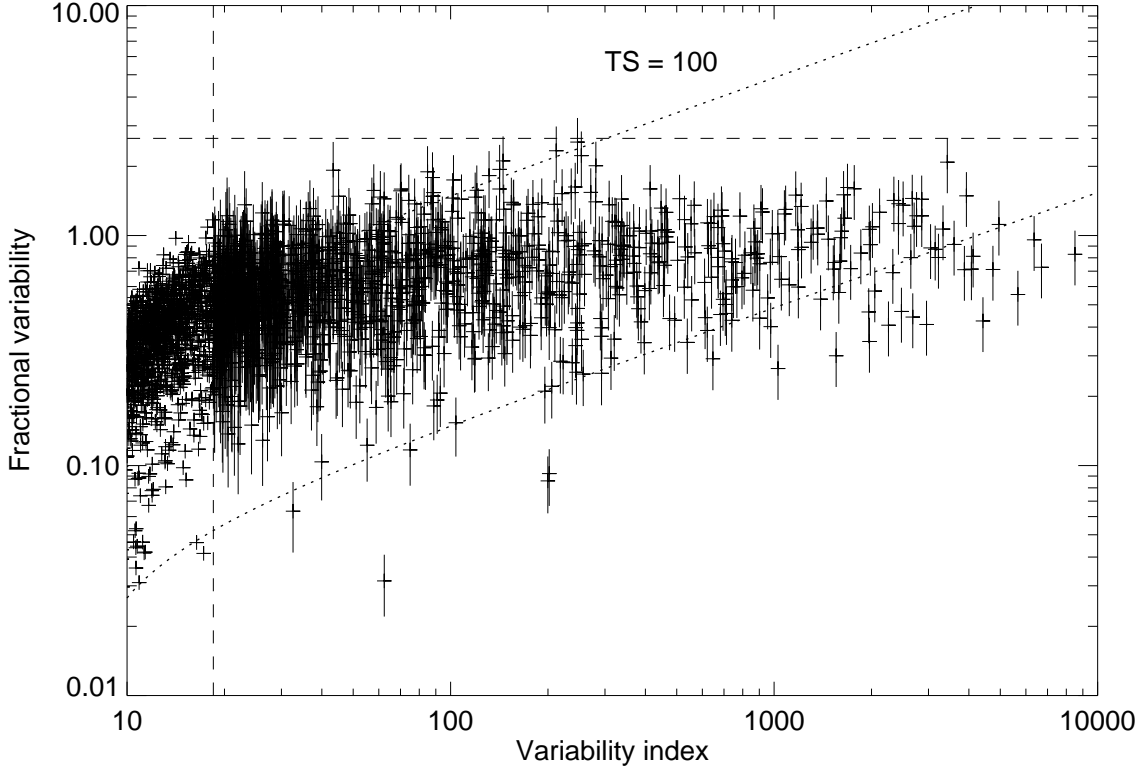


Figure 11. Fractional variability of all sources plotted as a function of variability index, over one-year intervals. The vertical dashed line (below which the points have no error bar) is the variability threshold. The horizontal dashed line is the maximum fractional variability that can be reached ($\sqrt{N_{\text{int}} - 1}$). The dotted lines show how the variability index depends on $\delta F/F$ at $TS = 100$ and at $TS = 10,000$. At a given TS threshold, the lower right part of the diagram is not accessible. The error bars are omitted below the variability threshold for clarity.

830 fluctuations:

$$Var = \frac{1}{N_{\text{int}} - 1} \sum_i (F_i - F_{\text{av}})^2 \quad (8)$$

$$\delta F = \sqrt{\max\left(Var - \frac{\sum_i \sigma_i^2}{N_{\text{int}}}, 0\right)} \quad (9)$$

$$\frac{\sigma_F}{F} = \max\left(\frac{1}{\sqrt{2(N_{\text{int}} - 1)}} \frac{V_i}{F_{\text{av}} \delta F}, 10\right) \quad (10)$$

831 where the fractional variability itself is simply $\delta F/F_{\text{av}}$. This is similar to Eq. 3 of 1FGL, except we
 832 omit the systematic error term because it is now incorporated in the σ_i^2 via the weights. The error
 833 σ_F/F is estimated from the expected scatter on the sample variance Var , which is the dominant
 834 source of uncertainty. We cap it at 10 to avoid reporting meaningless high uncertainties. Figure 11
 835 can be compared to Figure 8 of [Abdo et al. \(2009c\)](#), which was based on 1-week intervals (and
 836 contained many fewer sources, of course). The fractional variability is similar in the two figures,
 837 going up to 1, reflecting the absence of a preferred variability time scale in blazars. The criterion we

838 use is not sensitive to relative variations smaller than 50% at $TS = 100$, so only bright sources can
 839 populate the lower part of the plot. There is no indication that fainter sources are less variable than
 840 brighter ones, but we simply cannot measure their variability.

841 3.6.2. Two-month intervals

842 To characterize variability, it is of course useful to have information on shorter time scales than one
 843 year. Rather than use monthly bins as in 3FGL (which would have resulted in many upper limits),
 844 we have chosen to keep the same number of intervals and build light curves over 48 two-month
 845 bins. Because the analysis is not limited by systematics at low energy over two months, we tried to
 846 optimize the data selection differently. We used binned likelihood up to 3 GeV and the same zenith
 847 angle cuts as in Table 2, but included PSF2 events between 50 and 100 MeV (not only PSF3), and
 848 added PSF1 events between 100 and 300 MeV to our standard PSF2+3 selection. This improves the
 849 average source significance over one bin, and the Earth limb contamination remains minor. Similarly
 850 to the one-year analyses, to save disk space and CPU time we merged event types together in the
 851 binned data sets. We used unbinned likelihood above 3 GeV and again ignored events above 100 GeV
 852 (unimportant for variability).

853 The weights appropriate for two months were computed using the same procedure (Appendix B),
 854 entering the total data cube divided by 48 (same weights in each interval). The weights are of course
 855 larger than those for one year, but remain a significant correction in the Galactic plane. Up to
 856 100 MeV the weights range from 0.2 in the Galactic Ridge to 0.85 at high latitude. At 300 MeV
 857 they increase to 0.55 in the Galactic Ridge and 0.99 at high latitude. We used a different Sun/Moon
 858 model for each interval (the Sun averages out only over one year), but again assuming constant flux.
 859 Variability is considered probable when $TS_{\text{var}} > 72.44$, corresponding to 99% confidence in a χ^2
 860 distribution with $N_{\text{int}} - 1 = 47$ degrees of freedom. We find 1173 variable sources with that criterion,
 861 1057 of which were also considered variable with one-year intervals. Among the 116 sources considered
 862 variable only with 2-month light curves, 37 (1% of 3738) would be expected by chance, so more than
 863 two thirds must be really variable. Similarly, 270 sources are considered variable only with one-year
 864 intervals (39 expected by chance).

865 Two extended sources exceed the two-month variability threshold. They are the Monoceros SNR
 866 and the Cen A lobes. Both are very extended (several degrees). It is likely that their variability is
 867 due to a flaring background source that was missed by the global source detection over eight years.
 868 Indeed the peak in the light curve of the Monoceros SNR is in June - July 2012, at the time of
 869 Nova V959 Mon 2012 (Ackermann et al. 2014b). Another unexpected variable source is the Geminga
 870 pulsar. We think that its variability is not real but due to the direct pointings triggered toward the
 871 Crab when it was flaring (Geminga is 15° away), combined with details of the effective area or PSF
 872 dependence on off-axis angle, that normally average out in scanning mode.

873 Because the source fluxes are not allowed to be negative, the distribution of fluxes for a given source
 874 is truncated at 0. For faint sources, this results in a slight overestimate of the average flux (of no
 875 consequence) but also an underestimate of the sample variance (Eq. 8). As a result, the fractional
 876 variability (Eq. 9) is underestimated for faint sources and is often zero for weakly variable sources
 877 (below threshold). This even happens for two sources considered variable (just above threshold).

878 More sources are found to be variable using one-year intervals than using two-month intervals. The
 879 reason is illustrated in Figure 12, which shows the variability indices divided by $N_{\text{int}} - 1$ (so that
 880 they become directly comparable). If the sources behaved like white noise (as the statistical errors)

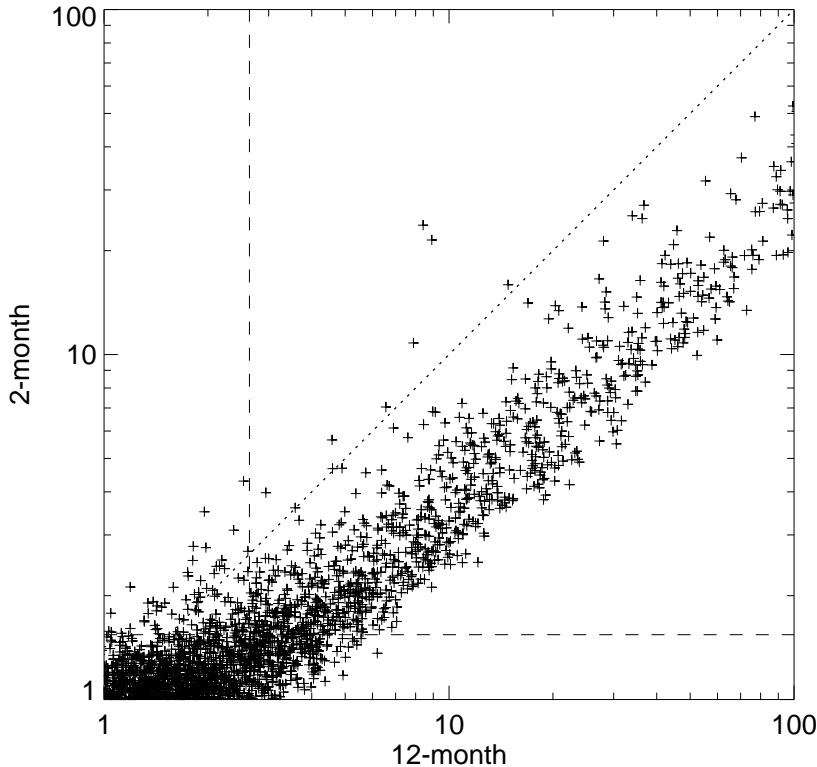


Figure 12. Comparison of the reduced variability index (divided by $N_{\text{int}} - 1$) from two-month intervals with that for one-year intervals. This illustrates that, for the majority of sources (AGN characterized by red noise) using longer intervals detects variability better. The dotted line is the diagonal (expected for white noise). The dashed lines show the two variability thresholds.

881 then the correlation would be expected to follow the diagonal. But blazars behave as red noise (more
 882 variability on longer time scales) so the correlation is shifted to the right and it is more advantageous
 883 to use longer intervals to detect variability with that criterion, because statistical errors decrease
 884 more than intrinsic variability.

885 Extending this relation to even shorter intervals, the 2FAV catalog of *Fermi*-LAT flaring sources
 886 (Abdollahi et al. 2017), which used 1-week intervals, found 518 significantly varying sources. The
 887 methodology was completely different (it didn't start from a catalog over many years) and the
 888 duration a little shorter (7.4 years) but the same trend remains to find fewer variable sources on
 889 shorter intervals. Not all sources are dominated by red noise however, and a fraction are above the
 890 diagonal in Figure 12. An example is provided in Figure 13 (left). In all cases, the variability is of
 891 course much better characterized with smaller intervals. An extreme example is provided in Figure 13
 892 (right).

893 *3.7. Limitations and Systematic Uncertainties*

894 *3.7.1. Diffuse emission model*

895 The model of diffuse emission is the main source of uncertainties for faint sources. Contrary to the
 896 effective area, it does not affect all sources equally: its effects are smaller outside the Galactic plane
 897 where the diffuse emission is fainter and varying on larger angular scales. It is also less of a concern

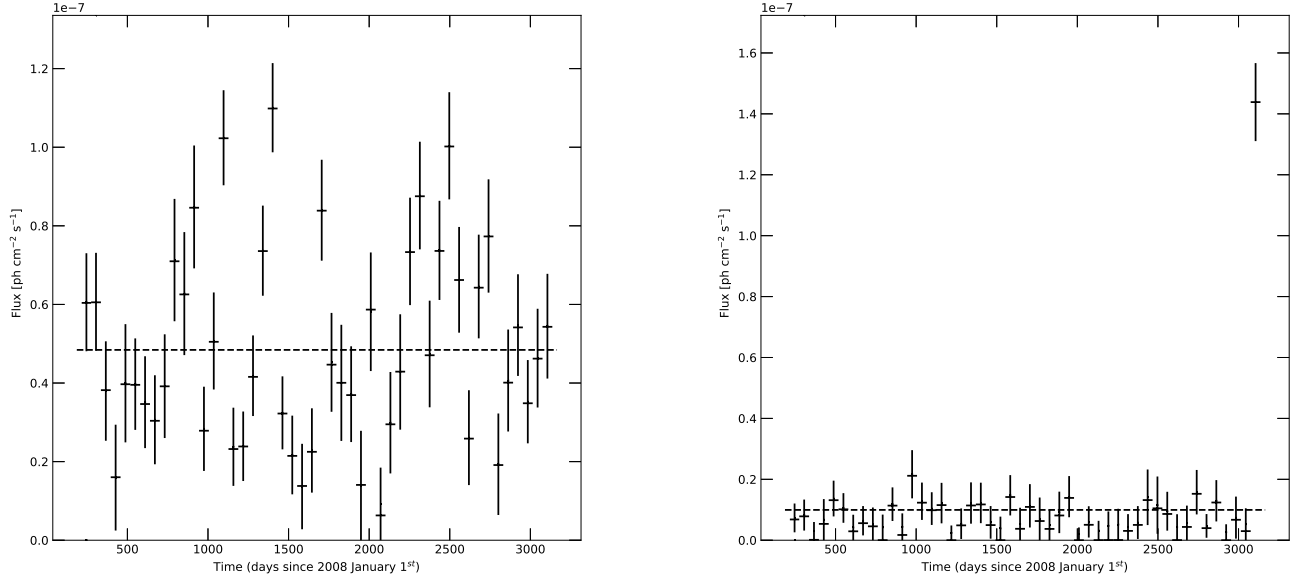


Figure 13. Light curves over two-month intervals of two blazars showing fast variability. Left: unclassified blazar PMN J0427–3900 at $TS_{\text{var}} = 202$. This is the highest TS_{var} among sources considered non-variable over one-year intervals ($TS_{\text{var}} = 17.8$). Its variability is very fast (more like white noise than red noise) and averages out over one-year intervals. Right: flat-spectrum radio quasar RX J0011.5+0058 at $TS_{\text{var}} = 278$, showing a single flare in the last 2-month bin. This source was detected as variable with one-year intervals ($TS_{\text{var}} = 79$).

898 at high energy (> 3 GeV) where the core of the PSF is narrow enough that the sources dominate the
 899 background under the PSF. But it is a serious concern inside the Galactic plane at low energy ($<$
 900 1 GeV) and particularly inside the Galactic ridge ($|l| < 60^\circ$) where the diffuse emission is strongest
 901 and very structured, following the molecular cloud distribution. It is not easy to assess precisely how
 902 large the uncertainties are, because they relate to uncertainties in the distributions of interstellar gas,
 903 the interstellar radiation field, and cosmic rays, which depend in detail on position on the sky.

904 We estimate, from the residuals over the entire Galactic plane, that the systematics are at the
 905 3% level. This is already an achievement, but the statistical Poisson errors corresponding to the
 906 diffuse emission integrated over the PSF (as described in Appendix B) are much smaller than this.
 907 Integrating energies up to twice the current one in the Galactic ridge, the statistical precision is 0.2,
 908 0.4, 1, 2, 5% above 100, 200, 500 MeV, 1, 2 GeV respectively.

909 The weights are able to mitigate the systematic effects globally, but cannot correct the model locally.
 910 In particular, underestimating the mass of an interstellar cloud will always tend to create spurious
 911 sources on top of it, and overestimating diffuse emission at a particular place tends to make the
 912 sources on top of it harder than they should be (because the model creates negative residuals there,
 913 and those are felt mostly at low energy). For an approximate local assessment, we have compared the
 914 4FGL catalog with a version of the FL8Y source list (which used the 3FGL Galactic diffuse model
 915 `g11_iem_v06`) obtained with the same setup as 4FGL (see § 4.2.2). Flags 1, 2 and 3 in Table 5 reflect
 916 that.

917 As we did for the 2FGL and 3FGL catalogs, we have checked which unidentified, non-variable
 918 sources with detection $TS < 150$ can be biased by large uncertainties in the modeling of the
 919 underlying Galactic interstellar emission. As described in more detail in the 2FGL paper, we have
 920 flagged sources that are potentially confused with complex small-scale structures in the interstellar
 921 emission. Their positions, fluxes, and spectral characteristics may not be reliable because of the
 922 uncertain contributions of the different gas components in their direction. Most flagged sources
 923 have $TS < 100$, but a large TS value does not guarantee their reliability since a deficit in the bright
 924 interstellar background is necessarily compensated by one bright, statistically significant, point source
 925 (or several of them). Most of the flagged sources have power-law indices above 2.2, but nine of them
 926 are harder. This is possible if the interstellar deficit is at sub-degree angular scales. The diffuse
 927 model can adapt spectrally up to the energy at which the PSF is at the same angular scale as the
 928 interstellar deficit, leaving only a high-energy excess. Those sources are assigned Flag 6 in the catalog
 929 (Table 5). We also append `c` to the source names (except the extended ones). Most (64, $\sim 70\%$)
 930 of those suspect sources have no association with a counterpart at other wavelengths, 10 have class
 931 UNK and 7 have class SPP (§ 5).

932 3.7.2. Analysis method

933 As in 3FGL, we use the *pointlike*-based method described in § 3.1 to estimate systematic errors due
 934 to the way the main *gtlike*-based method (§ 3.2) is set up in detail. Many aspects differ between the
 935 two methods: the code, the weights implementation, the RoIs, and the diffuse model adjustments.
 936 The *pointlike*-based method does not remove faint sources (with $TS < 25$) from the model. Even
 937 the data differ, since the *pointlike*-based method uses *Front* and *Back* event types whereas the
 938 *gtlike*-based method uses PSF event types with a different zenith angle cut. Both methods reject a
 939 fraction of the events below 1 GeV, but not the same one.

940 Because of all those differences, we expect that comparing the results of the two methods source
 941 by source can provide an estimate of the sensitivity of the source list to details of the analysis.
 942 In particular we use it to flag sources whose spectral characterization differs strongly with the two
 943 methods (Flags 1 and 3 in Table 5).

944 3.7.3. Analysis Flags

945 As in 3FGL we identified a number of conditions that should be considered cautionary regarding
 946 the reality of a source or the magnitude of the systematic uncertainties of its measured properties.
 947 They are described in Table 5, together with the number of sources flagged for each reason. Flags 1,
 948 2 and 3 alert to a different result with *pointlike* or the previous diffuse model. Flag 4 indicates a low
 949 source-to-background ratio. Flag 5 alerts to confusion, Flag 6 to a possible contamination by diffuse
 950 emission, Flag 9 to a bad localization, Flag 10 to a bad spectral representation and Flag 12 to a very
 951 highly curved spectrum. We have changed slightly the definition of Flag 5 on the conservative side.
 952 For any source, we define its best band k_0 as before (*i.e.*, the highest-energy band in which it has
 953 $TS > 25$, or the band with highest TS if none reaches 25). Defining TS_0 as the TS of the source in
 954 that band, we now consider that a neighbor is brighter whenever it has $TS > TS_0$ in band k_0 or in
 955 any higher-energy band. This catches soft sources close to a harder neighbor only somewhat more
 956 significant. The localization check with *gtfindsrc* (Flag 7 in 3FGL) was not done because unbinned
 957 likelihood is very slow and does not support energy dispersion nor weights. The Sun check (Flag 11
 958 in 3FGL) is no longer necessary since we now have a good model of the solar emission.

Table 5. Definitions of the Analysis Flags

Flag ^a	N_{sources}	Meaning
1	215	Source with $TS > 35$ which went to $TS < 25$ when changing the diffuse model (§ 3.7.1) or the analysis method (§ 3.7.2). Sources with $TS \leq 35$ are not flagged with this bit because normal statistical fluctuations can push them to $TS < 25$.
2	216	Moved beyond its 95% error ellipse when changing the diffuse model.
3	342	Flux (> 1 GeV) or energy flux (> 100 MeV) changed by more than 3σ when changing the diffuse model or the analysis method. Requires also that the flux change by more than 35% (to not flag strong sources).
4	212	Source-to-background ratio less than 10% in highest band in which $TS > 25$. Background is integrated over πr_{68}^2 or 1 square degree, whichever is smaller.
5	399	Closer than θ_{ref}^b from a brighter neighbor.
6	92	On top of an interstellar gas clump or small-scale defect in the model of diffuse emission; equivalent to the c designator in the source name (§ 3.7.1).
7	...	Not used.
8	...	Not used.
9	136	Localization Quality > 8 in <i>pointlike</i> (§ 3.1) or long axis of 95% ellipse $> 0^\circ 25$.
10	27	$\sum_i S_i^2 > 20.5$ or $S_i^2 > 9$ in any band (Eq. 5).
11	...	Not used.
12	102	Highly curved spectrum; LP_beta fixed to 1 or PLEC_Index fixed to 0 (see § 3.3).

^aIn the FITS version (see Appendix A) the values are encoded as individual bits in a single column, with Flag n having value $2^{(n-1)}$.

^b θ_{ref} is defined in the highest band in which source $TS > 25$, or the band with highest TS if all are < 25 . θ_{ref} is set to $3^\circ 77$ below 100 MeV, $1^\circ 68$ between 100 and 300 MeV (FWHM), $1^\circ 03$ between 300 MeV and 1 GeV, $0^\circ 76$ between 1 and 3 GeV (in-between FWHM and $2 r_{68}$), $0^\circ 49$ between 3 and 10 GeV and $0^\circ 25$ above 10 GeV ($2 r_{68}$).

959 In total 1163 sources are flagged in 4FGL (about 23%, similar to 3FGL). Only 15% of the sources
960 with power-law index $\Gamma < 2.5$ are flagged, but 47% of the soft sources with $\Gamma \geq 2.5$. This attests to
961 the exacerbated sensitivity of soft sources to the underlying background emission and nearby sources.
962 For the same reason, and also because of more confusion, 52% of sources close to the Galactic plane
963 (latitude less than 10°) are flagged while only 12% outside that region are. Only 15% of associated
964 sources are flagged but 45% of the non-associated ones are flagged. This is in part because the
965 associated sources tend to be brighter, therefore more robust, and also because many flagged sources
966 are close to the Galactic plane where the association rate is low.

967 4. THE 4FGL CATALOG

968 4.1. Catalog Description

969 The catalog is available online¹⁰, together with associated products. It contains 5065 sources¹¹.
970 The source designation is 4FGL JHHMM.m+DDMM where the 4 indicates that this is the fourth LAT
971 catalog, FGL represents *Fermi* Gamma-ray LAT. Sources confused with interstellar cloud complexes
972 are singled out by a c appended to their names, where the c indicates that caution should be used
973 in interpreting or analyzing these sources. The 75 sources that were modeled as extended for 4FGL
974 (§ 3.4) are singled out by an e appended to their names. The catalog columns are described in

¹⁰ See https://fermi.gsfc.nasa.gov/ssc/data/access/lat/8yr_catalog/.

¹¹ The file has 5066 entries because the Crab PWN is represented by two components (§ 3.3).

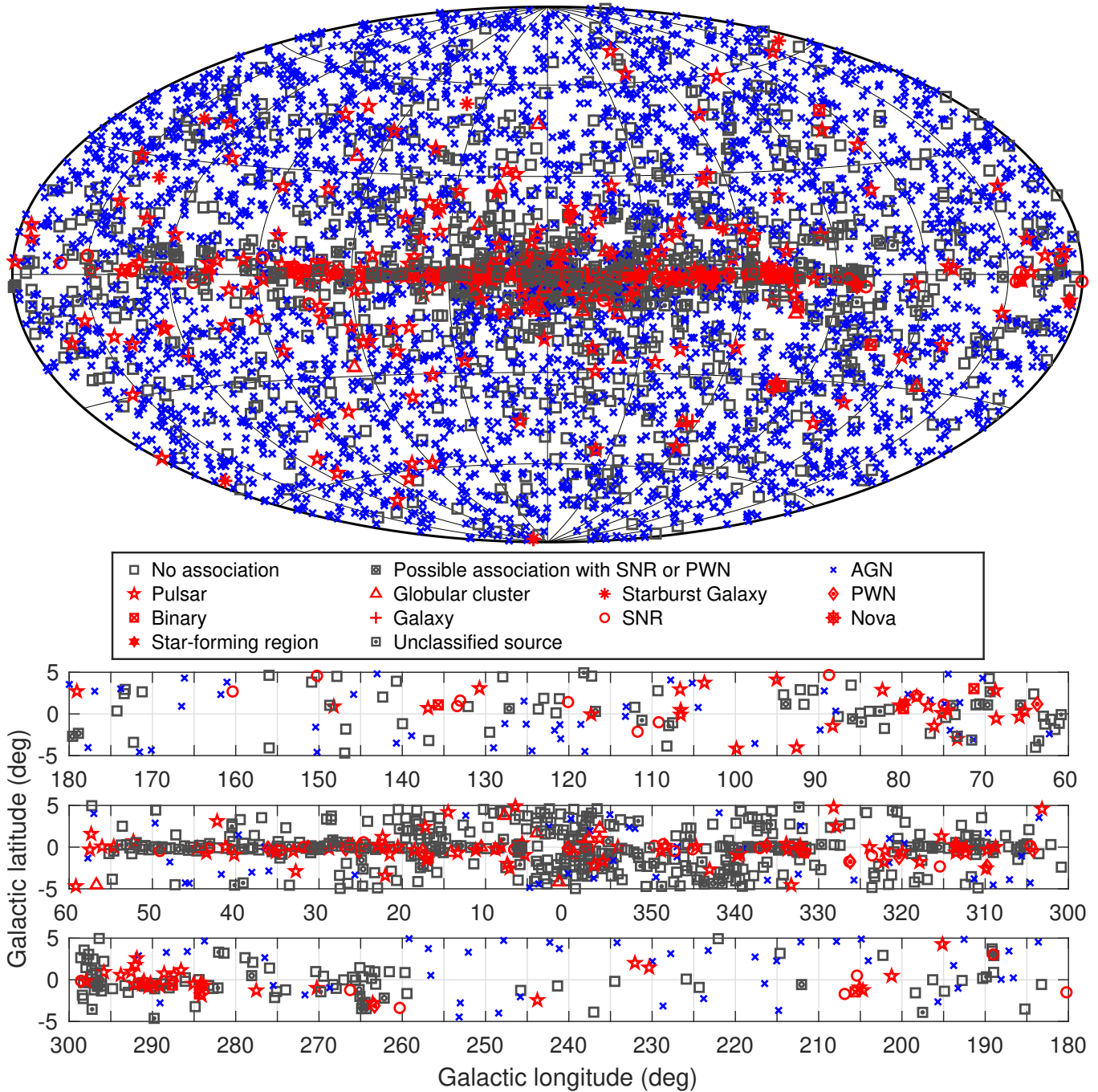


Figure 14. Full sky map (top) and blow-up of the Galactic plane split into three longitude bands (bottom) showing sources by source class (see § 6, no distinction is made between associations and identifications). All AGN classes are plotted with the same blue symbol for simplicity. Other associations to a well-defined class are plotted in red. Unassociated sources and sources associated to counterparts of unknown nature are plotted in black.

⁹⁷⁵ Appendix A. Figure 14 illustrates the distribution of the 4FGL sources over the sky, separately for
⁹⁷⁶ AGN (blue) and other (red) classes.

⁹⁷⁷

4.2. Comparison with 3FGL and earlier

4.2.1. General comparison

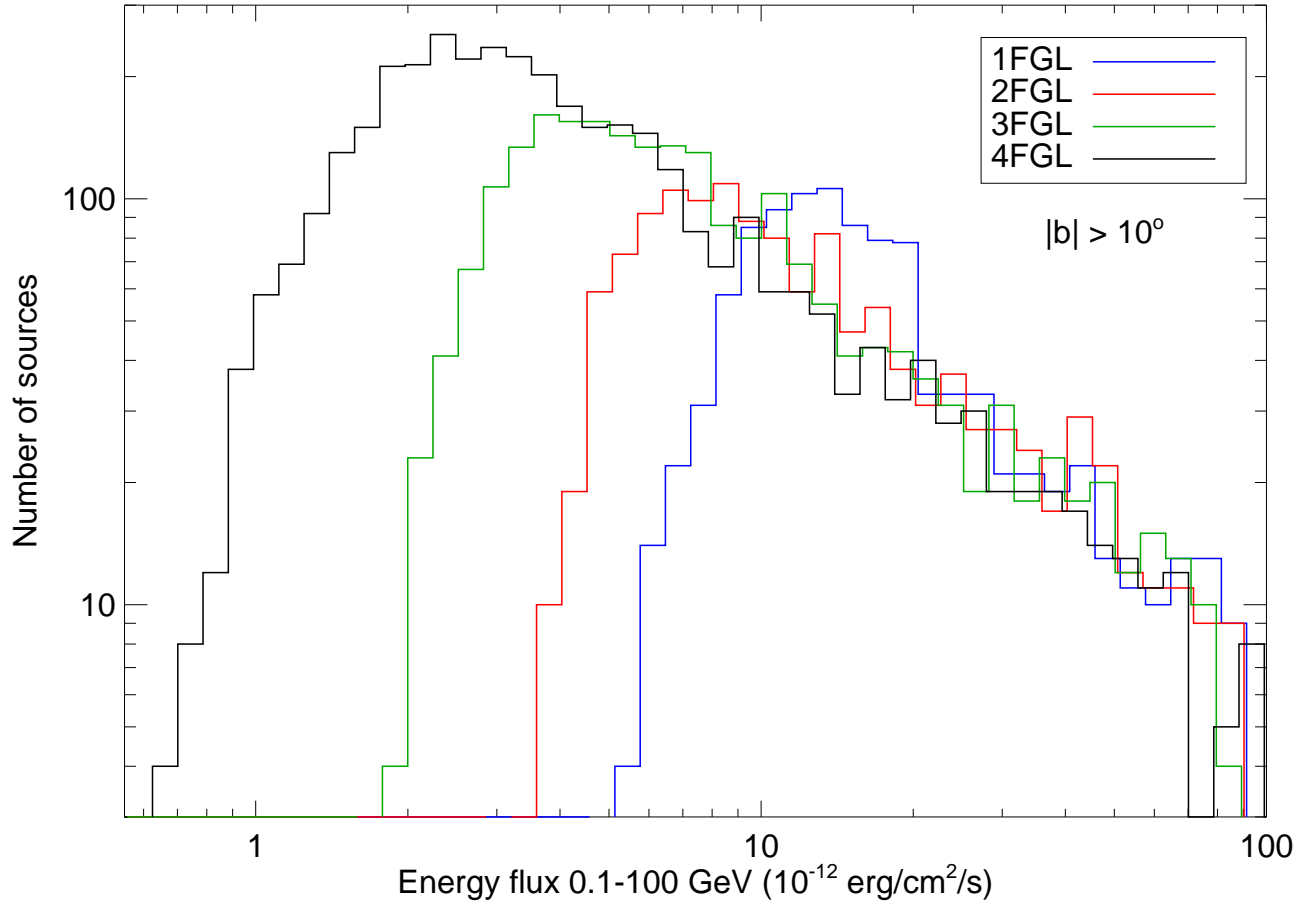


Figure 15. Distributions of the energy flux for the high-latitude sources ($|b| > 10^\circ$) in the 1FGL (1043 sources, blue), 2FGL (1319 sources, red), 3FGL (2193 sources, green) and 4FGL (3647 sources, black) catalogs, illustrating the approximate detection threshold.

979 Figure 15 shows the energy flux distribution in 1FGL, 2FGL, 3FGL and 4FGL. Comparing the
 980 current flux threshold with those published in previous LAT Catalog papers we see that in 4FGL the
 981 threshold is down to $\simeq 2 \times 10^{-12}$ erg cm $^{-2}$ s $^{-1}$, quantifying the gain from 3FGL. Above 10^{-11} erg cm $^{-2}$
 982 s $^{-1}$ the 2FGL and 3FGL distributions are entirely compatible with 4FGL. The 1FGL distribution
 983 shows a distinct bump between 1 and 2×10^{-11} erg cm $^{-2}$ s $^{-1}$. That accumulation of fluxes was clearly
 984 incorrect. We attribute it primarily to overestimating significances and fluxes due to the unbinned
 985 likelihood bias in the 1FGL analysis, and also to the less accurate procedure then used to extract
 986 source flux (see discussion in the 2FGL paper).

987 The threshold at low flux is less sharp in 4FGL than it was in 2FGL or 3FGL. This reflects a larger
 988 dependence of the detection threshold on the power-law index (Figure 16). The expected detection
 989 threshold is computed from Eq. A1 of Abdo et al. (2010a). The systematic limitation ϵ (entered in
 990 the weighted log-likelihood as described in Appendix B) is accounted for approximately by limiting
 991 the integral over angles to $\theta_{max}(E)$ such that $g(\theta_{max}, E) = \epsilon$, since $g(\theta_{max}, E)$ in that equation is

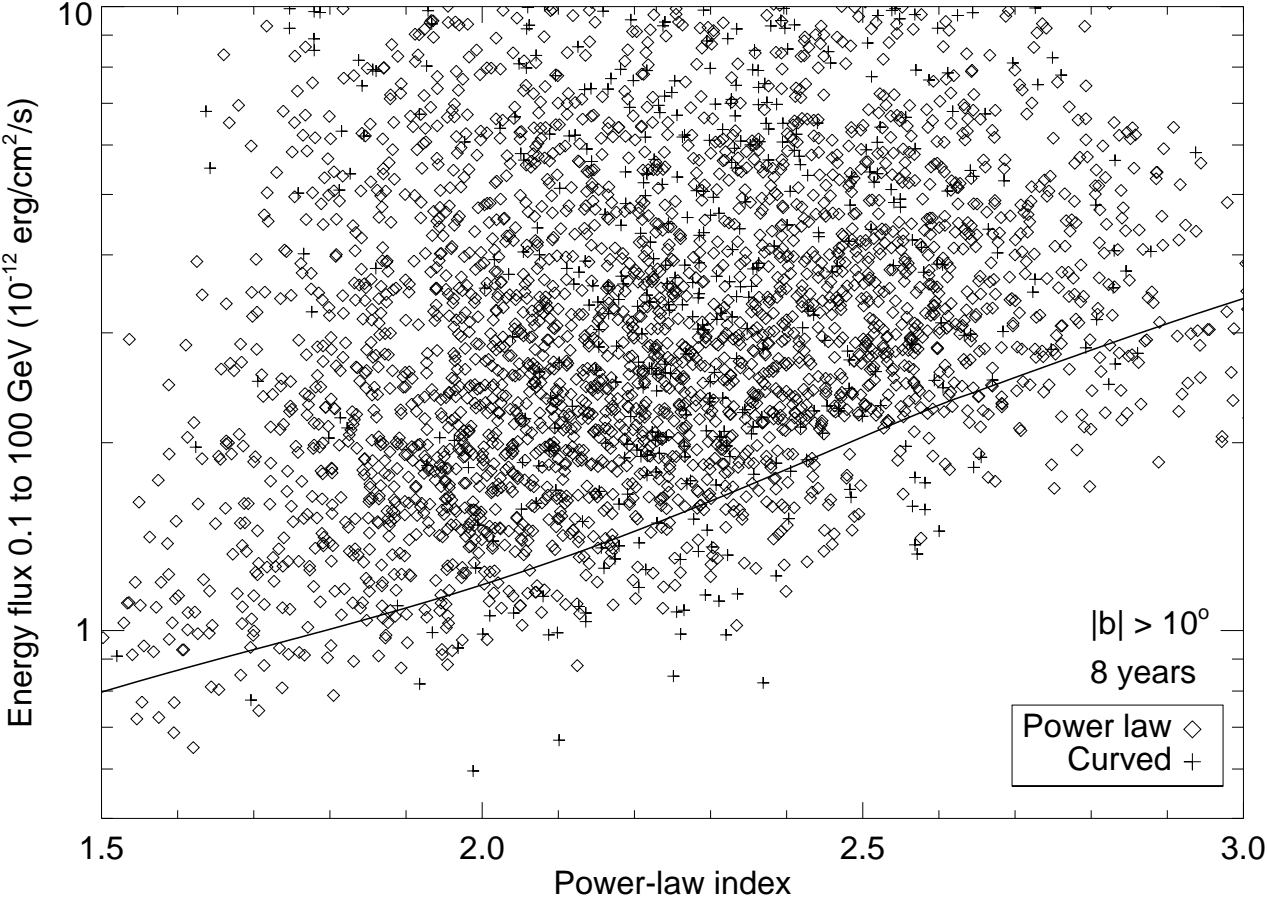


Figure 16. Energy flux and power-law index of all sources outside the Galactic plane ($|b| > 10^\circ$). The solid line shows the expected detection threshold for a power-law spectrum. It is consistent with the fluxes of detected power-law sources (diamonds). The four sources furthest below the line are all curved (+ signs). Indeed the detection threshold (in terms of energy flux from 0.1 to 100 GeV) is lower for curved sources.

992 exactly the source to background ratio. The detection threshold for soft sources decreases only slowly
 993 with exposure due to that.

994 The power-law index Γ is a way to compare all sources over all catalog generations, ignoring
 995 the complexities of the curved models. Figure 17 shows the four distributions of the power-law
 996 indices of the sources at high Galactic latitude are very similar. Their averages and widths are
 997 $\Gamma_{1\text{FGL}} = 2.22 \pm 0.33$, $\Gamma_{2\text{FGL}} = 2.17 \pm 0.30$, $\Gamma_{3\text{FGL}} = 2.22 \pm 0.31$ and $\Gamma_{4\text{FGL}} = 2.23 \pm 0.30$.

998 Small differences in the power-law index distributions could be related to slightly different
 999 systematic uncertainties in the effective area between the IRFs used respectively for 4FGL, 3FGL,
 1000 2FGL, and 1FGL (Table 1). There is actually no reason why the distribution should remain the
 1001 same, since the detection threshold depends on the index and the log N-log S of flat-spectrum radio
 1002 quasars, which are soft *Fermi*-LAT sources, differs from that of BL Lacs, whose spectra are hard in
 1003 the LAT band (Ackermann et al. 2015, Fig. 7). The apparent constancy may largely be the result of
 1004 competing effects.

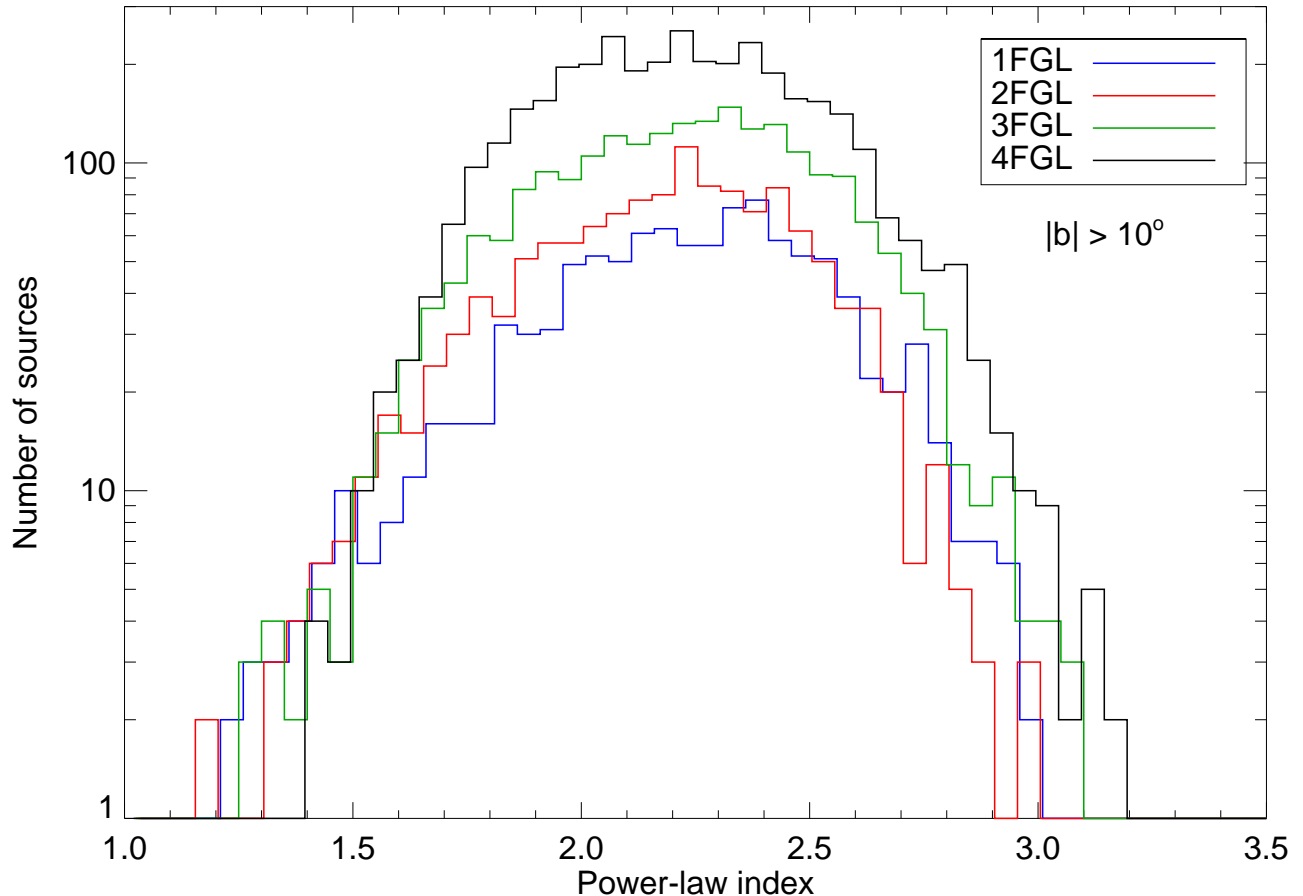


Figure 17. Distributions of the power-law index for the high-latitude sources in the 1FGL (blue), 2FGL (red), 3FGL (green) and 4FGL (black) catalogs. The sources are the same as in Fig 15.

1005 We have compared the distribution of error radii (defined as the geometric mean of the semi-
 1006 major and semi-minor axes of the 95% confidence error ellipse) of the 1FGL, 2FGL, 3FGL and 4FGL
 1007 sources at high Galactic latitude. Overall the source localization improves with time as more photons
 1008 are added to previously detected sources. We concentrate instead on what happens specifically for
 1009 faint sources. Figure 18 shows the distribution of 95% confidence error radii for those sources with
 1010 $25 < TS < 100$ in any of the catalogs. The improvement at a given TS level is partly due to the
 1011 event-level analysis (from Pass 6 to 7 and 8, see Table 1) and partly to the fact that, at a given
 1012 significance level and for a given spectrum, fainter sources over longer exposures are detected with
 1013 more photons. This improvement is key to preserving a high rate of source associations (§ 6) even
 1014 though the source density increases.

1015

4.2.2. Step-by-step from 3FGL to 4FGL

1016 To understand the improvements of the 4FGL analysis with respect to 3FGL, we have considered
 1017 the effects of changing the analysis and the data set without changing the time range (i.e., leaving
 1018 it as four years). To that end we started with the same seeds as the 3FGL catalog, changed each

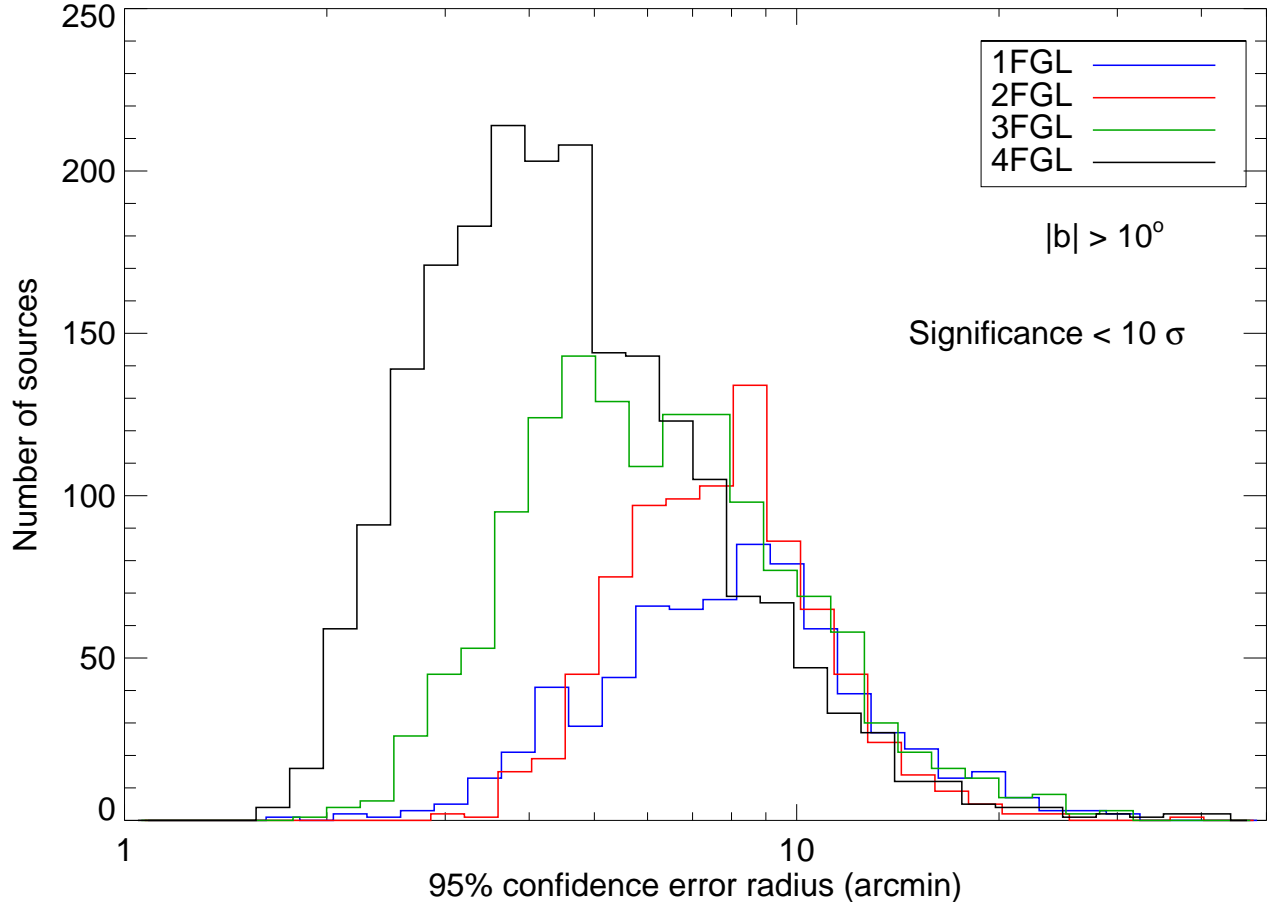


Figure 18. Distributions of the 95% confidence error radii for high-latitude sources with significance $< 10\sigma$ in 1FGL (713 sources, blue), 2FGL (843 sources, red), 3FGL (1387 sources, green) and 4FGL (2091 sources, black), illustrating the improvement of localizations for sources of equivalent detection significances.

1019 element in sequence (in the order of the list below) and compared each intermediate result with the
 1020 previous one. The effect of introducing energy dispersion was described in § 3.2.

- 1021 • We first switched from P7REP to Pass 8 (P8R3), eliminating the Earth limb by cutting zenith
 1022 angles $> 90^\circ$ at 100 to 300 MeV and $> 97.5^\circ$ at 300 MeV to 1 GeV for Front, $> 80^\circ$ at 100 to
 1023 300 MeV and $> 95^\circ$ at 300 MeV to 1 GeV for Back. The resulting TS increased by 27%, in
 1024 keeping with the effective area increase (the number of sources at $TS > 25$ did not rise, for lack of
 1025 seeds). Energy flux decreased by 7% in faint sources. In the Galactic plane, source spectra
 1026 tended to soften, with power-law indices increasing by 0.04 on average. Both effects appear to
 1027 be due to the diffuse emission modeling, because they are absent in the bright sources. The
 1028 isotropic spectrum was recomputed, and even though the Galactic diffuse model was the same,
 1029 its effects differed because the effective area increase with Pass 8 is stronger at low energy.
 1030 Those offsets are accompanied by a large scatter: only 72% of P7REP γ rays are still in P8R3,
 1031 and even for those the reconstructed direction differs.

- 1032 • Accounting for energy dispersion increased energy flux on average by 2.4%. The effect was
1033 larger for soft sources (3% at $\Gamma > 2.1$). The average power-law index did not change, but
1034 hard sources got a little softer and soft sources a little harder (with shifts no larger than
1035 0.02), reducing the width of the power-law index distribution. Spectra became more curved as
1036 expected (energy dispersion can only broaden the spectra): the curvature β increased by 0.014
1037 on average. None of these trends depends on Galactic latitude. The logLikelihood improved,
1038 but only by a few tens.
- 1039 • Switching from Front/Back to PSF event types increased TS by 10% (140 more sources). This
1040 was the intended effect (not diluting good events with bad ones should increase significance).
1041 No systematic effect was noted on energy flux. Soft sources got somewhat softer with PSF event
1042 types (power-law indices larger than 2.7 increased by 0.1 on average), but the bias averaged over
1043 all sources was only +0.01. The number of curved sources decreased by 50 and the curvature β
1044 by 0.025 (this is the same effect: low energies moved up, so spectra got closer to a power law).
- 1045 • Applying the weights results in a general decrease of TS and increase of errors, as expected.
1046 However, because source detection is dominated by energies above 1 GeV even without weights,
1047 the effect is modest (the number of sources decreased by only 40). The difference is of course
1048 largest for soft sources and in the Galactic plane, where the background is larger and the weights
1049 are smaller. There are a few other side effects. The number of curved sources decreased by 30.
1050 This is because the lever arm is less as the contributions from low-energy γ rays are unweighted.
1051 The pivot energy tended to increase for the same reason, and this resulted in a softening of
1052 the power-law index of curved sources (not exceeding 0.1). Overall in the Galactic ridge the
1053 power-law index increased by 0.025.

1054 We evaluated the other two changes on eight years of data:

- 1055 • Changing the energy range to start at 50 MeV did not improve TS , as expected (the PSF is
1056 too broad below 100 MeV to contribute to significance). The energy flux (defined in the same
1057 100 MeV to 100 GeV band) tended to decrease in the Galactic plane (by as much as -10% in
1058 the Galactic ridge) and the power-law index tended to become harder (by as much as -0.05
1059 in the Galactic ridge). This is because the low-energy information tends to stabilize artificially
1060 soft sources. Neither effect was noticeable outside the Galactic plane. The other consequence
1061 was to increase the number of significantly curved sources by 80, because the broader energy
1062 range made it easier to detect curvature (this was true everywhere in the sky).
- 1063 • Changing the Galactic diffuse emission model from `gll_iem_v06` used in 3FGL to that used
1064 here (§ 2.4), without changing the analysis or the data, had a noticeable effect. The flags in
1065 § 3.7.3 are based on the comparison to a version of the FL8Y source list (using `gll_iem_v06`)
1066 extending the energy range to start at 50 MeV, and using the same extended sources and TS_{curv}
1067 threshold as 4FGL. The source significance is lower in 4FGL by 0.1σ on average and the number
1068 of sources decreased by 10%. The energy flux is lower in 4FGL by 2%, the power-law index is
1069 smaller (harder) by 0.02 and there are more curved sources than in FL8Y. This is all because
1070 the intensity of the new diffuse model is somewhat higher below 100 MeV. Because this is a
1071 background-related effect, it affects primarily the faint sources. The strong overprediction west
1072 of Carina in `gll_iem_v06` is gone but overall the residuals are at a similar level.

1073 In conclusion, to first order the resulting net changes are not very large, consistent with the general
 1074 comparison between 4FGL and 3FGL in § 4.2.1. Systematic effects are collectively visible but within
 1075 calibration errors, and within statistical errors of individual sources.

1076

5. AUTOMATED SOURCE ASSOCIATIONS

Table 6. Catalogs Used for the Automatic Source Association Methods

Name	Objects ^a	Ref.
High \dot{E}/d^2 pulsars	313	Manchester et al. (2005) ^b
Other normal pulsars	2248	Manchester et al. (2005) ^b
Millisecond pulsars	240	Manchester et al. (2005) ^b
Pulsar wind nebulae	69	Collaboration internal
High-mass X-ray binaries	137	Garcia et al. (2019)
Low-mass X-ray binaries	187	Liu et al. (2007)
Point-like SNR	158	Green (2014) ^c
Extended SNR ^f	295	Green (2014) ^c
Globular clusters	160	Harris (1996)
Dwarf galaxies ^f	100	McConnachie (2012)
Nearby galaxies	276	Schmidt et al. (1993)
IRAS bright galaxies	82	Sanders et al. (2003)
BZCAT (Blazars)	3561	Massaro et al. (2009)
BL Lac	1371	Véron-Cetty & Véron (2010)
AGN	10066	Véron-Cetty & Véron (2010)
QSO	129,853	Véron-Cetty & Véron (2010)
Seyfert galaxies	27651	Véron-Cetty & Véron (2010)
Narrow-line Seyfert galaxies	18	Berton et al. (2015)
Narrow-line Seyfert galaxies	556	Rakshit et al. (2017)
FRICAT (Radiogalaxies)	233	Capetti, A. et al. (2017a)
FRICAT (Radiogalaxies)	123	Capetti, A. et al. (2017b)
Giant Radio Source	349	Kuźmicz et al. (2018)
2WHSP	1691	Chang et al. (2017)
WISE blazar catalog	12319	D’Abrusco et al. (2014)
Radio Fundamental Catalog (2019a)	14786	http://astrogeo.org/rfc
CGRaBS	1625	Healey et al. (2008)
CRATES	11499	Healey et al. (2007)
ATCA 20 GHz southern sky survey	5890	Murphy et al. (2010)
105-month <i>Swift</i> /BAT catalog	1632	Oh et al. (2018)
4 th IBIS catalog	939	Bird et al. (2016)
2nd <i>AGILE</i> catalog ^e	175	Bulgarelli et al. (2019)
3rd EGRET catalog ^e	271	Hartman et al. (1999)
EGR catalog ^e	189	Casandjian & Grenier (2008)
0FGL list ^e	205	Abdo et al. (2009c, 0FGL)
1FGL catalog ^e	1451	Abdo et al. (2010a, 1FGL)
2FGL catalog ^e	1873	Nolan et al. (2012, 2FGL)
3FGL catalog ^e	3033	Acero et al. (2015, 3FGL)
1FHL catalog ^e	514	Ackermann et al. (2013, 1FHL)

Table 6 continued on next page

Table 6 (*continued*)

Name	Objects ^a	Ref.
2FHL catalog ^e	360	Ackermann et al. (2016b, 1FHL)
3FHL catalog ^e	1556	Ajello et al. (2017, 1FHL)
TeV point-like source catalog ^{e,f}	108	http://tevcat.uchicago.edu/
TeV extended source catalog ^g	72	http://tevcat.uchicago.edu/
LAT pulsars	234	Collaboration internal ^d
LAT identified	145	Collaboration internal

^aNumber of objects in the catalog.

^bversion 1.56, <http://www.atnf.csiro.au/research/pulsar/psrcat>

^cGreen D. A., 2017, ‘A Catalogue of Galactic Supernova Remnants (2017 June version)’, Cavendish Laboratory, Cambridge, United Kingdom (available at <http://www.mrao.cam.ac.uk/surveys/snrs/>)

^d<https://confluence.slac.stanford.edu/display/GLAMCOG/Public+List+of+LAT-Detected+Gamma-Ray+Pulsars>

^eFor these catalogs, the association is performed according to Eq. 11.

^fVersion of 2018 November 30.

^gFor these catalogs of extended sources, the association is performed by requiring that the separation from the 4FGL sources is less than the quadratic sum of the 95% confidence error radii.

1077 The Bayesian source association method (Abdo et al. 2010a) for the *Fermi*-LAT, implemented
 1078 with the *gtsrcid* tool¹², was developed following the prescription devised by Mattox et al. (1997)
 1079 for EGRET. It relies on the fact that the angular distance between a LAT source and a candidate
 1080 counterpart is driven by i) the position uncertainty in the case of a real association and ii) the
 1081 counterpart density in the case of a false (random) association. In addition to the angular-distance
 1082 probability density functions for real and false associations, the posterior probability depends on a
 1083 prior. This prior is calibrated via Monte Carlo simulations so that the number of false associations,
 1084 N_{false} is equal to the sum of the association-probability complements. For a given counterpart catalog,
 1085 the so-obtained prior is found to be close to $N_{\text{assoc}}/N_{\text{tot}}$, where N_{assoc} is the number of associations
 1086 from this catalog and N_{tot} is the number of catalog sources. The sum of the association probabilities
 1087 over all pairs (γ -ray source, potential counterpart) gives the total number of real associations for a
 1088 particular catalog, allowing the number of subthreshold associations to be estimated. The total
 1089 numbers of associations are reported in § 6 for the various classes, where the overlap between
 1090 associations from different catalogs is taken into account. A uniform threshold of $P \geq 0.8$ is
 1091 applied to the posterior probability for the association to be retained. The reliability of the Bayesian
 1092 associations is assessed by verifying that the distribution of the angular offset between γ -ray source
 1093 and counterpart matches well the expected one in the case of a true association, i.e., a Rayleigh
 1094 function with its width parameter given by the sources’ positional uncertainties.

1095 The counterpart catalogs (Table 6) include known γ -ray-emitting source classes: Active Galactic
 1096 Nuclei (AGNs, Ackermann et al. 2015), galaxies (Abdo et al. 2010g), pulsars (Abdo et al. 2013),
 1097 pulsar-wind nebulae (PWNe, Ackermann et al. 2011c), supernova remnants (SNRs, Acero et al.
 1098 2016b), globular clusters (GLCs, Abdo et al. 2010h), low- and high-mass X-ray binaries (Abdo et al.

¹² <https://fermi.gsfc.nasa.gov/ssc/data/analysis/scitools/overview.html>

1099 2010i, 2009d) or surveys of candidate blazars at other frequencies (radio, IR, X-rays). The reported
1100 source classes are derived in the same way as in 3FGL. For non-AGN sources, this classification is
1101 based on the nature of the association catalogs. For AGNs, the subclasses as flat-spectrum radio
1102 quasars (FSRQs), BL Lac-type objects (BLLs), blazar candidates of uncertain type (BCUs), radio
1103 galaxies (RDGs), narrow-line Seyfert 1 (NLSY1s), steep spectrum radio quasars (SSRQs), Seyfert
1104 galaxies (SEYs) or simply AGNs (if no other particular subclass can be assigned), have been selected
1105 according to the counterpart properties at other wavelengths. Please note that we did not use the
1106 blazar classes from the Simbad database¹³ since some of them correspond to predictions based on the
1107 *WISE*-strip approach (D’Abrusco et al. 2014) and not to assessment with the measured strengths of
1108 the emission lines.

1109 In complement to the Bayesian method, the Likelihood-Ratio (LR) method (Ackermann et al.
1110 2011b, 2015), following de Ruiter et al. (1977) provides supplementary associations with blazar
1111 candidates based on large radio and X-ray surveys: NVSS (Condon et al. 1998), SUMSS (Mauch et al.
1112 2003), *ROSAT* (Voges et al. 1999, 2000) and AT20G (Murphy et al. 2010). This method is similar in
1113 essence to the Bayesian method but the false association rate is derived from the density of objects
1114 brighter than the considered candidate, assessed from the survey log N-log S distribution. While the
1115 LR method is able to handle large surveys, its fraction of false associations is notably larger than
1116 for the Bayesian method (typically 10% vs. 2%). The overlap between the results of the Bayesian
1117 and LR methods is about 75% for blazars. Because the surveys include a large number of Galactic
1118 sources at low Galactic latitudes, the class of $|b| < 10^\circ$ sources associated solely via the LR-method
1119 has been set to UNK (standing for unknown) as opposed to the BCU class used by default for sources
1120 at higher latitudes.

1121 Firm identifications are based on periodic variability for LAT-detected pulsars or X-ray binaries,
1122 correlated variability at other wavelengths for AGNs or spatial morphology related to that found in
1123 another band for extended sources.

1124 The association and classification procedures greatly benefited from data of recent intensive follow-
1125 up programs, motivated by the study of the unidentified/unassociated γ -ray sources. This study
1126 was recognized as one of the major scientific goals of the *Fermi* mission. Many groups carried out
1127 follow-up observations and/or applied statistical procedures to investigate and discern the nature of
1128 the unassociated sources from their gamma-ray properties (see, e.g., Ackermann et al. 2012c; Hassan
1129 et al. 2013; Doert & Errando 2014). In particular, follow-up campaigns were carried out at different
1130 wavelengths with both ground-based and space telescopes above GHz frequencies (see, e.g., Kovalev
1131 2009; Petrov et al. 2011, 2013; Hovatta et al. 2012, 2014; Schinzel et al. 2015, 2017) and below (see,
1132 e.g., Massaro et al. 2013; Nori et al. 2014; Giroletti et al. 2016), or using sub-millimeter (see, e.g.,
1133 Giommi et al. 2012; López-Caniego et al. 2013) and infrared observations (see, e.g., Massaro et al.
1134 2011, 2012b,a; Arsioli et al. 2015; Massaro & D’Abrusco 2016; D’Abrusco et al. 2014) up to the
1135 X-rays with *Swift* (e.g., Mirabal & Halpern 2009; Paggi et al. 2013; Takeuchi et al. 2013; Stroh &
1136 Falcone 2013; Acero et al. 2013; Landi et al. 2015; Paiano et al. 2017b) as well as with *Chandra*
1137 and *Suzaku* (e.g., Maeda et al. 2011; Cheung et al. 2012; Kataoka et al. 2012; Takahashi et al. 2012;
1138 Takeuchi et al. 2013). Over the years, these observations allowed additions to the lists of potential
1139 counterparts, which were then used with the methods previously described. In addition, to assess

¹³ <http://simbad.u-strasbg.fr/simbad/>

Table 7. LAT 4FGL Source Classes

Description	Identified		Associated	
	Designator	Number	Designator	Number
Pulsar, identified by pulsations	PSR	229
Pulsar, no pulsations seen in LAT yet	psr	10
Pulsar wind nebula	PWN	11	pwn	6
Supernova remnant	SNR	24	snr	16
Supernova remnant / Pulsar wind nebula	SPP	0	spp	78
Globular cluster	GLC	0	glc	30
Star-forming region	SFR	3	sfr	0
High-mass binary	HMB	5	hmb	3
Low-mass binary	LMB	1	lmb	1
Binary	BIN	1	bin	0
Nova	NOV	1	nov	0
BL Lac type of blazar	BLL	22	bll	1109
FSRQ type of blazar	FSRQ	42	fsrq	652
Radio galaxy	RDG	6	rdg	36
Non-blazar active galaxy	AGN	1	agn	10
Steep spectrum radio quasar	SSRQ	0	ssrq	2
Compact Steep Spectrum radio source	CSS	0	css	5
Blazar candidate of uncertain type	BCU	2	bcu	1310
Narrow-line Seyfert 1	NLSY1	4	nlsy1	5
Seyfert galaxy	SEY	0	sey	1
Starburst galaxy	SBG	0	sbg	7
Normal galaxy (or part)	GAL	2	gal	1
Unknown	UNK	0	unk	92
Total	...	354	...	3374
Unassociated	1337

NOTE—The designation ‘spp’ indicates potential association with SNR or PWN. Designations shown in capital letters are firm identifications; lower case letters indicate associations.

1140 the real nature and classify all newly associated sources, it has been crucial to perform additional
1141 spectroscopic optical observations, which for extragalactic objects were also able to provide estimates
1142 of their cosmological distances (see, e.g., Shaw et al. 2013b,a; Paggi et al. 2014; Massaro et al. 2015b;
1143 Ricci et al. 2015; Massaro et al. 2015a; Landoni et al. 2015b,a; Chiaro et al. 2016; Álvarez Crespo
1144 et al. 2016a,b; Landoni et al. 2018; Paiano et al. 2017a,c,d; Peña-Herazo et al. 2017; Marchesi et al.
1145 2018; Marchesini et al. 2019). These campaigns are continuously updated including searches in the
1146 optical databases of the major surveys (see, e.g., Cowperthwaite et al. 2013; Massaro et al. 2014;
1147 Maselli et al. 2015; Álvarez Crespo et al. 2016c; Massaro et al. 2016).

1148 The false-association rate is difficult to estimate for the new associations resulting from these
1149 follow-up observations, preventing them from being treated on the same footing as those obtained as
1150 described above. The most-recent Radio Fundamental Catalog¹⁴ (RFC) includes many new entries
1151 that came from dedicated follow-up observations. Applying the Bayesian method to the whole catalog
1152 and retaining associations with $P \geq 0.8$, the association probability attached to the recent additions
1153 (181 sources) are reported as NULL to distinguish them from the others.

¹⁴ Available at <http://astrogeo.org/rfc>

1154

6. ASSOCIATION SUMMARY

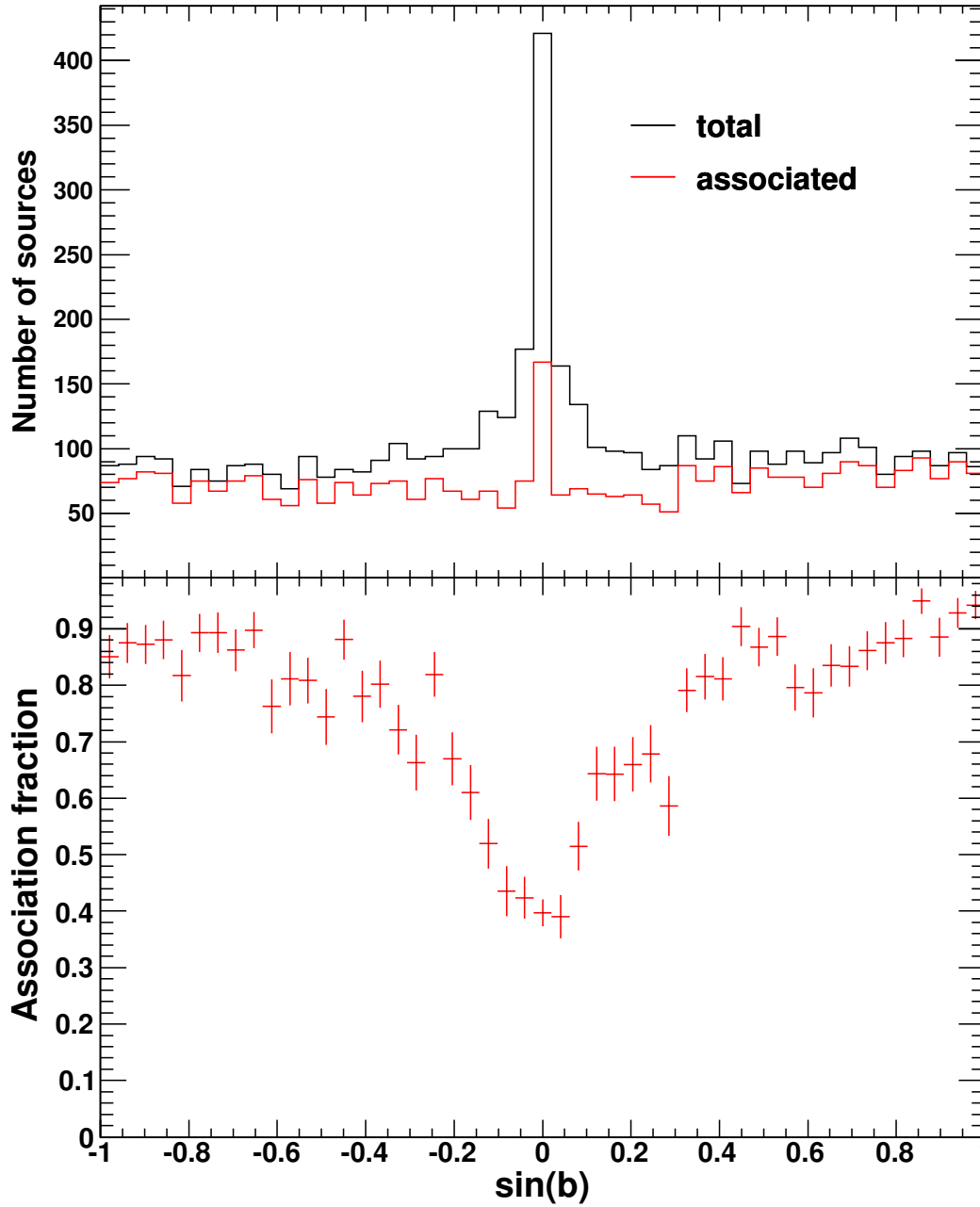


Figure 19. Upper panel: Distributions in Galactic latitude b of 4FGL sources (black histogram) and associated sources (red histogram). Lower panel: Association fraction as a function of Galactic latitude.

1155 The association summary is given in Table 7. Out of 5065 LAT sources in 4FGL, 1337 are
 1156 unassociated (26.4%). Some 92 others are classified as UNKs, and 78 as SPPs (sources of unknown
 1157 nature but overlapping with known SNRs or PWNe and thus candidates to these classes), representing
 1158 3.3% in total. Some 3463 sources are associated with the Bayesian method (1069 associations from

Table 8. 3FGL sources with different counterparts in 4FGL

3FGL name	3FGL counterpart	3FGL class	4FGL name	4FGL counterpart	4FGL class
J0500.3+5237	...	spp	J0500.2+5237	GB6 J0500+5238	bcu
J0618.0+7819	1REX J061757+7816.1	fsrq	J0618.1+7819	NGC 2146	sbg
J0647.1-4415	SUMSS J064648-441929	bcu	J0647.7-4418	RX J0648.0-4418	hmb
J0941.6+2727	MG2 J094148+2728	fsrq	J0941.9+2724	GB6 J0941+2721	bll
J1048.6+2338	NVSS J104900+233821	bll	J1048.6+2340	PSR J1048+2339	PSR
J1111.9-6038	...	spp	J1111.8-6039	PSR J1111-6039	PSR
J1132.8+1015	4C +10.33	fsrq	J1130.8+1016	2MASS J11303636+1018245	bcu
J1741.1-3053	MSH 17-39	snr	J1741.4-3046	NVSS J174122-304712	unk
J1811.3-1927c	...	spp	J1811.5-1925	PSR J1811-1925	psr
J1817.2-1739	...	spp	J1817.1-1742	PSR J1817-1742	PSR
J2022.2+3840	...	spp	J2022.3+3840	PSR J2022+3842	PSR
J2224.6-1122	PKS 2221-116	bll	J2225.5-1114	PKS 2223-114	bll

1159 this method only, overall $N_{\text{false}}=36.6$), 2604 sources with the LR method (210 associations from this
 1160 method only, $N_{\text{false}}=22.2$ for the latter). The overall association fraction, 70%, is similar to that
 1161 obtained in previous LAT catalogs. The association fraction is lower for fainter sources (essentially
 1162 all $TS > 500$ sources are associated), in particular due to their larger error regions. This fraction
 1163 also decreases as sources lie closer to the Galactic plane as illustrated in Figure 19. It decreases from
 1164 about 85% at high Galactic latitudes to $\simeq 40\%$ close to the Galactic plane. The reason for such
 1165 an effect is twofold. First, the number of unassociated Galactic sources is large. Secondly, the flux
 1166 limits of some extragalactic-counterpart catalogs are larger due to extinction effects for the optical
 1167 and X-ray bands in these directions. The properties of the unassociated sources are discussed below.
 1168 Sources reported as new below were not in previous FGL catalogs, although their detections may
 1169 have been reported in other works (e.g., Zhang et al. 2016; Arsioli & Polenta 2018) or in specialized
 1170 LAT catalogs. Table 8 lists the 12 3FGL sources that have different counterparts in 4FGL. Pulsations
 1171 have been detected for 5 sources previously classified as SPPs. As discussed below, the association of
 1172 4FGL J0647.7-4418 with RX J0648.0-4418 instead of SUMSS J064648-441929 remains uncertain.

1173 6.1. Extragalactic sources

1174 6.1.1. Active Galactic Nuclei

1175 The largest source population in 4FGL is that of AGNs, with 3137 blazars, 42 radio galaxies and
 1176 28 other AGNs. The blazar sample comprises 694 FSRQs, 1131 BLLs and 1312 BCUs. The detailed
 1177 properties of the 4FGL AGNs, including redshifts and fitted synchrotron-peak positions, will be the
 1178 subject of the 4LAC companion catalog. We note here that the separation in γ -ray spectral hardness
 1179 between FSRQs and BL Lacs already reported in previous LAC AGN catalogs is confirmed: 93% of
 1180 FSRQs and 81% of BL Lacs have power-law photon indices greater and lower than 2.2 respectively.
 1181 Among the 70 non-blazar AGNs, 35 were present in 3FGL. Note that the location of the γ -ray source
 1182 associated with Cen B is not coincident with that of the radio-galaxy core but points to the southern
 1183 radio jet. Twenty-three radio galaxies, listed in Table 9, are new. Four 3FGL sources have changed
 1184 classes to radio galaxies: three former BCU (IC 1531, TXS 0149+710, PKS 1304-215) and one
 1185 former BLL (B3 1009+427). The 28 other AGNs include five compact steep spectrum radio sources
 1186 (CSS, three are new: 3C 138, 3C 216, 3C 309.1), two steep spectrum radio quasars (SSRQ, new is 3C

Table 9. New radio galaxies in 4FGL

4FGL name	4FGL counterpart
J0038.7–0204	3C 17
J0057.7+3023	NGC 315
J0237.7+0206	PKS 0235+017
J0312.9+4119	B3 0309+411B
J0433.0+0522	3C 120
J0708.9+4839	NGC 2329
J0931.9+6737	NGC 2892
J1116.6+2915	B2 1113+29
J1149.0+5924	NGC 3894
J1236.9–7232	PKS 1234–723
J1306.3+1113	TXS 1303+114
1449.5+2746	B2 1447+27
J1516.5+0015	PKS 1514+00
J1518.6+0614	TXS 1516+064
J1521.1+0421	PKS B1518+045
J1724.2–6501	NGC 6328
J1843.4–4835	PKS 1839–48
J2156.0–6942	PKS 2153–69
J2227.9–3031	PKS 2225–308
J2302.8–1841	PKS 2300–18
J2326.9–0201	PKS 2324–02
J2329.7–2118	PKS 2327–215
J2341.8–2917	PKS 2338–295

1187 212), 9 narrow-line Seyferts 1 (NLSY1), one Seyfert galaxy (the Circinus galaxy, SEY) and 11 AGNs
 1188 of other types (AGN). Three NLSY1 are new: IERS B1303+515, B3 1441+476, TXS 2116–077.

1189

6.1.2. *Other galaxies*

1190 No other nearby galaxies, besides the SMC, LMC, and M 31, are detected. Seven starburst galaxies
 1191 in the *IRAS* catalog (Sanders et al. 2003) are associated with 4FGL sources. Two sources, Arp 220
 1192 (Peng et al. 2016; Griffin et al. 2016; Yoast-Hull et al. 2017) and NGC 2146 (Tang et al. 2014), have
 1193 been reported as LAT detections since the 3FGL release. Yoast-Hull et al. (2017) found an excess
 1194 of γ rays over the expected starburst contribution in Arp 220, similar to the case of the Circinus
 1195 galaxy (Hayashida et al. 2013). NGC 2146 being close ($0^{\circ}1$) to the FSRQ 1REX J061757+7816.1,
 1196 the association is ambiguous. We favor the NGC 2146 association as no evidence for variability is
 1197 found and the 4FGL photon index (2.17 ± 0.17) is somewhat low for a FSRQ. Another source, NGC
 1198 3424, was not present in 3FGL. The *IRAS* source UGC 11041, which could have been classified as sbg
 1199 shows significant variability in the LAT band, so the γ -ray emission most likely arises from an AGN
 1200 (there is a flat-spectrum radio source, MG2 J175448+3442 at a distance of $2.4'$) and it is classified as
 1201 such. In addition to these seven associations, the Bayesian method predicts that three more 4FGL
 1202 sources should be starburst galaxies. Some 4FGL sources are positionally consistent with known
 1203 galaxy clusters, but these clusters host radio galaxies which are the most likely emitters. No dwarf
 1204 galaxies have been detected.

6.2. Galactic sources

1205

1206 The Galactic sources include:

1207

1208

1209

1210

1211

1212

1213

1214

1215

1216

1217

1218

1219

1220

1221

1222

1223

1224

1225

1226

1227

1228

1229

1230

1231

1232

1233

1234

1235

1236

1237

1238

1239

1240

1241

- 239 pulsars (PSR). The public list of LAT-detected pulsars is regularly updated¹⁵. Some 229 pulsars in this list are included in 4FGL (65 would have been missed by the association pipeline using the ATNF catalog), while 6 are absent because they did not pass the $TS > 25$ criterion. These pulsars represent by far the largest population of identified sources in 4FGL. Another 10 pulsars from the ATNF database are associated with 4FGL sources with high-confidence via the Bayesian method that we consider γ -ray pulsar candidates. This method predicts that about 30 other 4FGL sources are ATNF pulsars. Note that out of the 24 pulsar candidates presented in 3FGL, pulsations have now been detected for 19 of them. The other 5 are not associated with pulsars in 4FGL.
- 40 supernova remnants (SNR). Out of them, 24 are extended and thus firmly identified. The other 16 are not resolved. SNR G150.3+4.5 has a log-normal spectral shape with a very hard photon index Γ of 1.6, which indicates that the emission is most likely leptonic and makes this source an excellent candidate for the Cherenkov Telescope Array (CTA). In contrast, the softer spectrum of the LMC SNR N 132D (photon index=2.07) makes the hypothesis of a dominant hadronic emission likely. The significant spectral curvature seen in Puppis A is consistent with its non-detection in the TeV domain.
- 17 pulsar wind nebulae (PWN), 15 of them being extended. New associations are N 157B, PWN G63.7+1.1, HESS J1356–645, FGES J1631.6–4756, FGES J1836.5–0651, FGES J1838.9–0704, HESS J1857+026. The median photon index of the 4FGL PWNe is 2.31. N 157B, located in the LMC, has a photon index of 2.0, hinting at an additional contribution from a (yet-undetected) pulsar at low energy on top of the PWN.
- 78 unassociated sources overlapping with known PWNe or SNRs (SPP). Estimation of missed associations of SNR, PWN and SPP sources is made difficult by the intrinsic spatial extension of the sources; no attempts have thus been made along this line.
- 30 globular clusters (GLC). Missing relative to 3FGL is 2MS–GC01. The 16 new associations are NGC 362, NGC 1904, NGC 5286, NGC 5904, NGC 6139, NGC 6218, NGC 6304, NGC 6341, NGC 6397, NGC 6402, NGC 6838, NGC 7078, Terzan 1, Terzan 2, GLIMPSE C01, GLIMPSE C02. Only two other 4FGL sources are estimated to be GLCs.
- Six high-mass X-ray binaries (HMB). The three new sources are HESS J0632+057, which has a reported LAT detection after 3FGL (Li et al. 2017b), Cyg X-1, an archetypical black-hole binary reported after the 3FGL (Zdziarski et al. 2017; Zanin et al. 2016), and RX J0648.0–4418/HD 49798, which is a peculiar X-ray binary (Mereghetti et al. 2011; Popov et al. 2018). The association probability of RX J0648.0–4418/HD 49798 is just barely larger (0.85 vs 0.80) than that of the blazar candidate SUMSS J064744–441946. Three other 4FGL sources are estimated to be HMBs according to the Bayesian method.

¹⁵ See <https://confluence.slac.stanford.edu/display/GLAMCOG/Public+List+of+LAT-Detected+Gamma-Ray+Pulsars>

- 1242 • Three star-forming regions; new since 3FHL is the association of the extended source FHES
1243 J1626.9–2431 (§ 3.4) with the ρ Ophiuchi star-forming region. Positional coincidences between
1244 4FGL sources and two of the brightest extended H II regions present in the catalog of [Paladini
1245 et al. \(2003\)](#) have been found. They are reported here as candidate associations: one region
1246 corresponds to NGC 6618 in M17, whose extension of 6′ at 2.7 GHz encompasses 4FGL
1247 J1820.4–1609; the second one corresponds to NGC 4603, which has a similar extension of
1248 6′ at 2.7 GHz and encompasses 4FGL J1115.1–6118.
- 1249 • Two low-mass X-ray binaries (LMB). PSR J1023+0038 is a known binary millisecond
1250 pulsar/LMB transition system, with a change in γ -ray flux detected ([Stappers et al. 2014](#))
1251 simultaneously with a state change, and was previously detected as 2FGL J1023.6+0040 (but
1252 not detected in 3FGL). The LMB 2S 0921–630 (V395 Car) is a well-studied binary involving
1253 a neutron star and a K0 III star with an orbital period of 9 days ([Shahbaz & Watson 2007](#))
1254 and is a new LAT detection.
- 1255 • One binary star system (BIN), η Carinae ([Abdo et al. 2010i](#); [Reitberger et al. 2015](#)).
- 1256 • One nova, V5668 Sagittarii ([Cheung et al. 2016](#)). Other novae detected by the LAT are missing.
1257 Novae have short durations, and most are below the significance threshold because their signal
1258 is diluted over the eight years of 4FGL data. As discussed in Section 3.6.2, Nova V959 Mon
1259 2012 is confused with the SNR Monoceros.

1260 6.3. *Low-probability associations*

1261 As a new feature relative to previous catalogs, the most probable counterpart to a 4FGL
1262 unassociated source is given in a separate column of the FITS table, along with the corresponding
1263 association probability (applying a threshold of 0.1 on that probability). This additional information,
1264 to be used with care given its low confidence, is meant to foster further investigations regarding the
1265 nature of these 4FGL sources and to help clarify why detections claimed in other works are sometimes
1266 missing in 4FGL. We report 124 low-confidence ($0.1 < P < 0.8$) associations with the Bayesian method.
1267 Note that the relative distances between γ -ray and counterpart sources remain quite small (53 are
1268 within r_{95} and all within $1.85 r_{95}$). This quite small number of low-association sources illustrates
1269 how quickly the Bayesian association probability drops with increasing relative distance in the case
1270 of 4FGL. Except for rare exceptions, the other 1199 4FGL sources (having not even low-confidence
1271 associations) will not get associated with any of the tested sources (i.e., belonging to the catalogs
1272 listed in Table 6) in a future LAT catalog. We also report 42 matches (classified as UNK) with
1273 sources from the *Planck* surveys (with $0.1 < P \leq 1$) to guide future investigations.

1274 6.4. *Unassociated sources*

1275 Out of the 1337 sources unassociated in 4FGL, 368 already present in 3FGL had no associations
1276 there. Another 27 sources previously associated in 3FGL have now lost their associations because of
1277 a shift in their locations relative to 3FGL.

1278 About half of the unassociated sources are located less than 10° away from the Galactic plane.
1279 Their wide latitude extension is hard to reconcile with those of known classes of Galactic γ -ray
1280 sources. For instance, Figure 20 compares this latitude distribution with that of LAT pulsars. In
1281 addition to nearby millisecond pulsars, which have a quasi isotropic distribution, the LAT detects

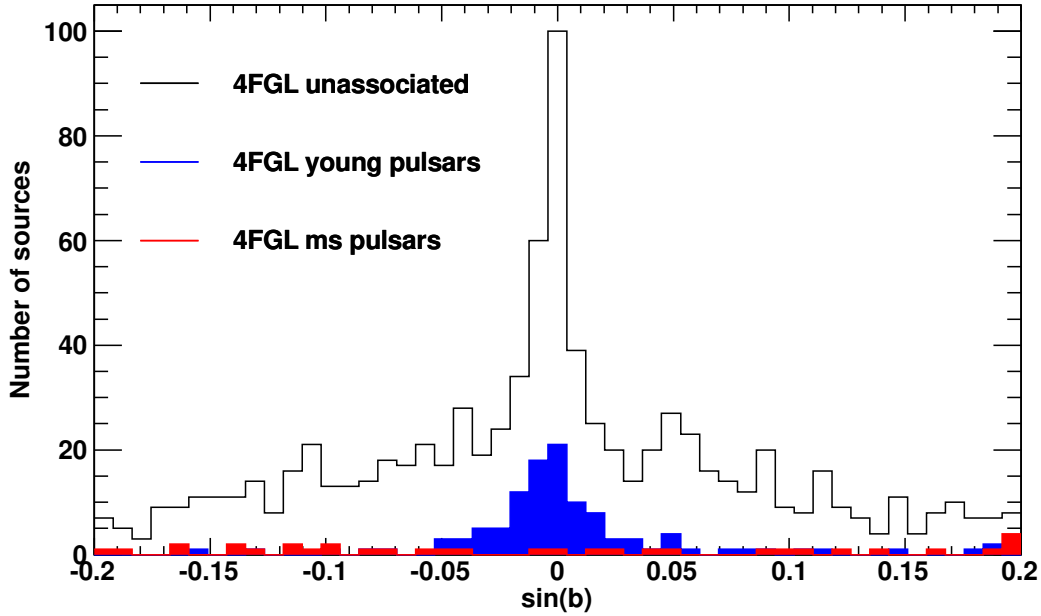


Figure 20. Distributions in Galactic latitude b of 4FGL low-latitude, unassociated sources (black histogram), compared to those of LAT-detected pulsars (young pulsars: blue histogram, millisecond pulsars (MSP): red histogram).

1282 only young isolated pulsars (age $< 10^6$ y) which are by nature clustered close to the plane. Older
 1283 pulsars, which have had time to drift further off the plane, show a wider Galactic-latitude distribution,
 1284 more compatible with the observed distribution of the unassociated sources, but these pulsars have
 1285 crossed the ‘ γ -ray death line’ (see [Abdo et al. 2013](#)) and are hence undetectable. Attempts to
 1286 spatially cross correlate the unassociated population with other potential classes, e.g., LMBs ([Liu
 1287 et al. 2007](#)), O stars¹⁶, and Be stars¹⁷ have been unsuccessful. The observed clustering of these
 1288 unassociated sources in high-density ‘hot spots’ may be a clue that they actually correspond to
 1289 yet-to-be identified, relatively nearby extended sources. The Galactic latitude distribution near the
 1290 plane is clearly non-Gaussian as visible in [Figure 20](#), which may indicate the presence of several
 1291 components.

1292 The spectral properties of these sources can also provide insight into their nature, as illustrated
 1293 in [Figure 21](#) which shows the latitude distribution of their spectral indices. The change in spectral
 1294 hardness with sky location demonstrates the composite nature of the unassociated population. The
 1295 high-latitude sources have an average photon index compatible with that of blazars of unknown type
 1296 ($\Gamma=2.24$), a hint that these sources could be predominantly blazars. Unassociated sources lying closer
 1297 to the Galactic plane have softer spectra, closer to that expected for young pulsars ($\Gamma=2.42$). Another
 1298 interesting possibility is that some of these unassociated sources actually correspond to WIMP dark
 1299 matter annihilating in Galactic subhalos ([Ackermann et al. 2012e](#); [Coronado-Blázquez et al. 2019](#)).
 1300 Indeed, Λ CDM cosmology predicts the existence of thousands of subhalos below $\sim 10^7 M_\odot$, i.e.,
 1301 not massive enough to retain gas or stars at all. As a result, they are not expected to emit at other

¹⁶ Galactic O-star catalog (GOSC) <https://gosc.cab.inta-csic.es/>

¹⁷ Be Star Spectra (BeSS) <http://basebe.obspm.fr/basebe/>

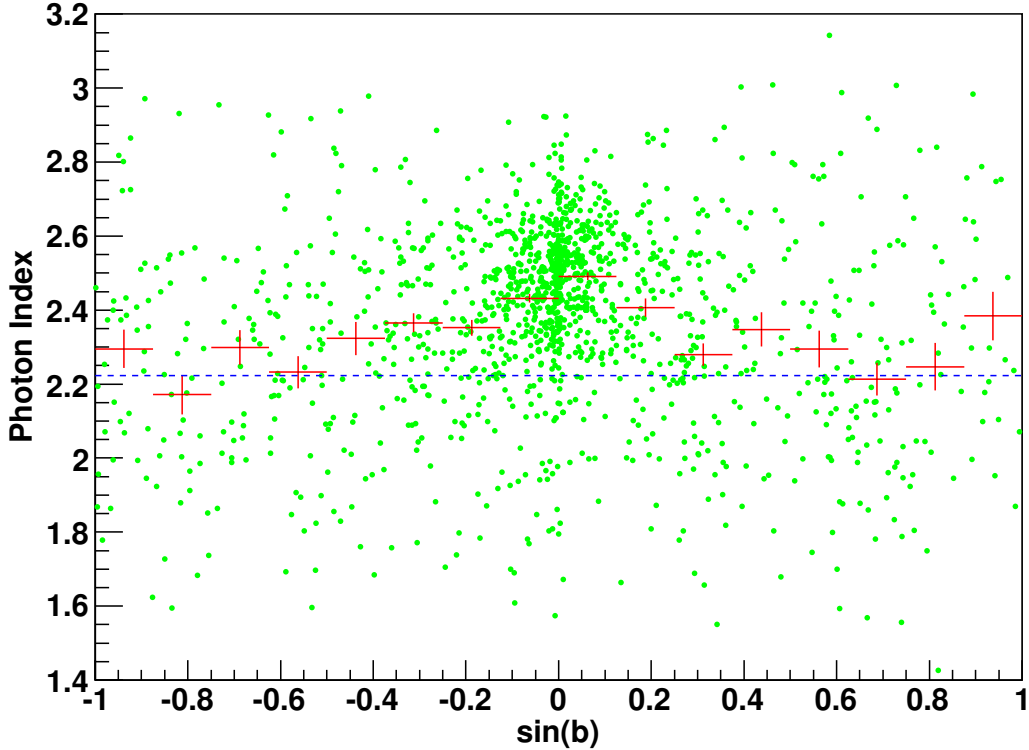


Figure 21. Green symbols: Power-law photon index versus Galactic latitude, b , for the unassociated 4FGL sources. Red bars: average photon index for different bins in b . Dashed blue line: average photon index of 4FGL BCU blazars.

1302 wavelengths and therefore they would not possess astrophysical counterparts. Annihilation of particle
 1303 dark matter may yield a pulsar-like spectrum (Baltz et al. 2007).

1304 *6.5. Sources missing from previous Fermi catalogs*

1305 The correspondence of 4FGL sources with previous *Fermi*-LAT catalogs (reported in the ASSOC_FGL
 1306 and ASSOC_FHL columns) was based, as in 3FGL, on error-circle overlap at the 95% confidence level,
 1307 amounting to

$$\Delta \leq d_{x,a} = \sqrt{\theta_{x,a}^2 + \theta_{x,4FGL}^2} \tag{11}$$

1308 where Δ is the angular distance between a 4FGL source and a source in catalog a , and the θ_x
 1309 are derived from the Conf_95_SemiMajor columns in the two catalogs at the $x\%$ confidence level
 1310 (assuming a 2-D normal distribution). We also considered that a previous LAT source corresponds
 1311 to a 4FGL source whenever they have the same association (the associations can have offsets greater
 1312 than θ_{95} , depending on the density of sources in the catalogs of counterparts at other wavelengths).

1313 We checked all sources that did not have an obvious counterpart in 4FGL inside d_{95} , nor a common
 1314 association. The procedure is described in detail in § 4.2.3 of the 3FGL paper. The result is provided
 1315 in one FITS file per catalog¹⁸, reporting the same information as Table 11 of the 3FGL paper:

¹⁸ The files are available at https://www-glast.stanford.edu/pub_data/1626/.

Table 10. Statistics of previous *Fermi* sources missing in 4FGL

	0FGL	1FGL	2FGL	3FGL	1FHL	2FHL	3FHL
All	16	283	311	469	23	34	33
With flags ^(a)	...	117	229	262
Name-FGL c ^(b)	...	83	97	52
Split into several 4FGL sources ^(c)	13	58	68	65	3	3	5
Within 1° of a 4FGL e ^(d)	11	45	65	93	4	6	5
AGN	1	8	17	55	1	2	10
PSR	0	1	2	3	0	0	0
spp	4	7	19	11	2	0	0
Other class-type	0	1	2	3	0	1	3
Unassociated	11	266	271	397	20	31	20
Present in 0FGL	...	6	2	6	1	1	0
Present in 1FGL	8	...	56	35	4	3	3
Present in 2FGL	4	74	...	78	4	6	1
Present in 3FGL	7	52	91	...	6	4	4
Present in 1FHL	0	12	7	2	...	8	2
Present in 2FHL	1	3	0	2	5	...	1
Present in 3FHL	0	8	4	4	2	4	...
Not in any other <i>Fermi</i> -LAT catalog	4	186	188	369	12	21	27

^aThose are flagged as F in the FITS files.

^bc indicates that based on the region of the sky the source is considered to be potentially confused with Galactic diffuse emission.

^cThose are flagged as S in the FITS files.

^de indicates a source that was modeled as spatially extended. Those are flagged as E in the FITS files.

1316 counterparts up to 1°, whether they are inside $d_{99.9}$ ($= 1.52 d_{95}$) or not, and specific conditions
1317 (flagged, c source, close to an extended source, split into several sources). The number of missed
1318 sources and their nature are provided in Table 6.5.

1319 We have looked at the most-recent catalogs, 3FGL and 3FHL, in more detail. Because the first four
1320 years are in common, we expect the 3FGL and 4FGL positions to be correlated. That correlation
1321 is however less than one might think because the data have changed (from Pass 7 to Pass 8, § 2.2).
1322 We found that the distribution of $\Delta/d_{95,3FGL}$ (when it is less than 1) is narrower by a factor 0.83
1323 than the Rayleigh distribution. This means that, by cutting at $d_{95,3FGL}$, we expect only 1.3% misses
1324 by chance (about 40 sources). With 3FHL the correlation is larger because it used Pass 8 already,
1325 the overlap is 7 years, and for the hard sources present in 3FHL the lower-energy photons do not
1326 contribute markedly to the localization. The distribution of $\Delta/d_{95,3FHL}$ is narrowed by a factor 0.62,
1327 and the number of chance misses by cutting at $d_{95,3FHL}$ should be only 0.04% (about 1 source). The
1328 correlation is similarly large with 2FHL (6 years of Pass 8 data). That correlation effect is less for
1329 earlier catalogs, so for them the fraction of true counterparts that are found outside the combined
1330 95% error circle is closer to 5%. Most of those true sources are expected to have a 4FGL counterpart
1331 at the 99.9% level in the FITS files.

1332 Out of 3033 3FGL sources, 469 are missing in 4FGL for various reasons, including the change of
1333 diffuse emission model, point sources being absorbed into new extended ones, or variability effects.
1334 Most of these missing sources had low significance in 3FGL. Only 72 sources were associated. The

majority are blazars (35 BCUs, 17 FSRQs, one BLL, and one SSRQ) plus one AGN. While BLLs are 36% more numerous relative to FSRQs in 3FGL, only one has gone away in 4FGL, an effect possibly related to the larger variability of FSRQs relative to BLLs observed in the LAT energy band (Ackermann et al. 2015). Other missing sources include 11 SPPs, 3 PSRs, one SNR, and one PWN. The nova V407 Cyg is now missing as it no longer fulfills the average-significance criterion.

Two LAT pulsars are considered lost. PSR J1513–5908 (= 3FGL J1513.9–5908) inside the PWN MSH 15–52 is a pulsar peaking at MeV energies (Kuiper et al. 1999), very soft in the LAT band (Pellizzoni et al. 2009; Abdo et al. 2010j), which has gone below threshold after applying the weights. PSR J1112–6103 (= 3FGL J1111.9–6058) was split into two 4FGL sources. One is still associated to the pulsar, but it is not the one closest to the 3FGL position. The third missing pulsar association was between 3FGL J1632.4–4820 and the non-LAT PSR J1632–4818, in a confused region now covered by the extended source 4FGL J1633.0–4746e. Among the five most significant lost 3FGL sources ($> 20\sigma$), the brightest one (3FGL J1714.5–3832 = CTB 37A) was split into two 4FGL sources, the brighter of which is associated instead to the newly discovered pulsar PSR J1714–3830 (Saz Parkinson et al. 2018) inside the CTB 37A SNR, and hence was not recognized as a common association. Two others (3FGL J1906.6+0720 and 3FGL J0536.4–3347) were also split, and now both members of each pair are associated. This is definitely an improvement. The last two (3FGL J1745.3–2903c and 3FGL J1747.0–2828) were within 0.6° of the Galactic center, a region of the sky where changing the diffuse model had a strong impact. They have no 4FGL counterpart at all.

Concerning sources missing from 3FHL, established with Pass 8 data as 4FGL, they amount to 33, with 17 unassociated, 9 blazars (4 BLLs and 5 BCUs), one AGN, one SNR, four UNKs and the transient HMB PSR B1259–63 (diluted over 8 years). All these sources had a TS close to the $TS = 25$ significance threshold.

6.6. TeV sources

Table 11. Associations of 4FGL with Extended TeV Sources

TeVCat Name ^a	4FGL Name
Boomerang	J2229.0+6114
CTA 1	J0007.0+7303
CTB 37A	J1714.4–3830
CTB 37B	J1714.1–3811
Crab	J0534.5+2201e
G318.2+00.1	J1453.4–5858
Geminga	J0633.9+1746
HESS J1018–589B	J1016.3–5857
HESS J1026–582	J1028.5–5819
HESS J1303–631	J1303.0–6312e
HESS J1356–645	J1355.2–6420e
HESS J1420–607	J1420.3–6046e
HESS J1427–608	J1427.8–6051
HESS J1458–608	J1456.7–6050, J1459.5–6053
HESS J1507–622	J1507.9–6228e
HESS J1534–571	J1533.9–5712e
HESS J1614–518	J1615.3–5146e

Table 11 continued on next page

Table 11 (*continued*)

TeVcat Name ^a	4FGL Name
HESS J1616–508	J1616.2–5054e
HESS J1632–478	J1633.0–4746e
HESS J1640–465	J1640.6–4632
HESS J1702–420	J1705.7–4124
HESS J1718–385	J1718.2–3825
HESS J1729–345	J1730.1–3422
HESS J1745–303	J1745.8–3028e
HESS J1800–240A	J1801.8–2358
HESS J1800–240B	J1800.2–2403, J1800.7–2355, J1800.9–2407
HESS J1804–216	J1804.7–2144e
HESS J1808–204	J1808.2–2028e
HESS J1809–193	J1810.3–1925e
HESS J1813–126	J1813.4–1246
HESS J1813–178	J1813.1–1737e
HESS J1825–137	J1824.5–1351e
HESS J1826–130	J1826.1–1256
HESS J1834–087	J1834.5–0846e
HESS J1841–055	J1840.9–0532e
HESS J1848–018	J1847.2–0141, J1848.6–0202, J1848.7–0129
HESS J1857+026	J1857.7+0246e
HESS J1858+020	J1858.3+0209
HESS J1912+101	J1911.7+1014, J1912.7+0957, J1913.3+1019
IC 443	J0617.2+2234e
Kookaburra (Rabbit)	J1417.7–6057, J1418.7–6057
Kookaburra PWN	J1420.0–6048
MGRO J1908+06	J1906.2+0631, J1907.9+0602
MGRO J2031+41	J2028.6+4110e
MSH 15–52	J1514.2–5909e
RCW 86	J1443.0–6227e
RX J0852.0–4622	J0851.9–4620e
RX J1713.7–3946	J1713.5–3945e
SNR G292.2–00.5	J1119.1–6127
TeV J1626–490	J1628.2–4848
Terzan 5	J1748.0–2446
VER J2019+407	J2021.0+4031e
Vela X	J0833.1–4511e
W 28	J1801.3–2326e
W 51	J1923.2+1408e
Westerlund 1	J1645.8–4533, J1648.4–4611, J1649.2–4513, J1650.3–4600, J1652.2–4516
Westerlund 2	J1023.3–5747e

^aFrom <http://tevcat.uchicago.edu>.

1359 The synergy between the LAT and the Cherenkov telescopes operating in the TeV energy domain
1360 has proven extremely fruitful, in particular by bringing out promising TeV candidates in the LAT
1361 catalogs. This approach, further motivated by the upcoming deployment of the Cherenkov Telescope
1362 Array, has justified the release of LAT source catalogs above 10 GeV, like the 3FHL (Ajello et al. 2017)

1363 based on 7 years of data. The associations of 4FGL sources with extended sources listed in TeVCat¹⁹
 1364 are presented in Table 11. Relative to 3FHL, 9 new extended TeV sources are associated with 4FGL
 1365 extended sources (TeV sources: HESS J1534–571, HESS J1808–204, HESS J1809–193, see § 3.4), or
 1366 (sometimes multiple) 4FGL point sources (TeV sources: HESS J1718–385, HESS J1729–345, HESS
 1367 J1848–018, HESS J1858+020, MGRO J1908+06, HESS J1912+101). All TeV blazars have 4FGL
 1368 counterparts. The median value of Γ for 4FGL point sources associated with TeV point sources is
 1369 1.95, indicating hard spectra as expected. In associations with extended TeV sources, the median Γ
 1370 changes from 2.09 to 2.38 depending on whether the 4FGL sources are extended or not. This fairly
 1371 large difference favors the interpretation that most associations between extended TeV sources and
 1372 non-extended 4FGL sources are accidental.

1373 6.7. Counterpart positions

1374 Whenever a high-confidence association with a point-like counterpart is obtained, we provide the
 1375 most accurate counterpart position available and its uncertainty. In particular, 2541 4FGL AGNs
 1376 have Very Long Baseline Interferometry (VLBI) counterparts. VLBI, i.e., radio interferometry with
 1377 baseline lengths of >1000 km, is sensitive to radio emission from compact regions of AGNs that are
 1378 smaller than 20 milliarcsecond (mas), which corresponds to parsec scales. Such observations allow the
 1379 determination of positions of the AGN jet base with mas level accuracy. We used the RFC catalog
 1380 based on the dedicated on-going observing program (Schinzel et al. 2015, 2017) with the Very Long
 1381 Baseline Array (Napier et al. 1994), as well as VLBI data under other programs. The association
 1382 between γ -ray source and VLBI counterpart was evaluated along a similar, but distinct, scheme as
 1383 that presented in § 5. This scheme (see Petrov et al. 2013, for more details) is based on the strong
 1384 connection between the γ -ray emission and radio emission at parsec scales and on the sky density of
 1385 bright compact radio sources being relatively low. The chance to find a bright background, unrelated
 1386 compact radio source within the LAT positional error ellipse is low enough to establish association.
 1387 The likelihood ratio (with a somewhat different definition from that implemented in the LR-method)
 1388 was required to be greater than 8 to claim an association, with an estimated false association fraction
 1389 of 1%.

1390 For AGNs without VLBI counterparts, the position uncertainties were set to typical values of
 1391 $20''$ for sources associated from the RASS survey and $10''$ otherwise. For identified pulsars, the
 1392 position uncertainties come from the rotation ephemeris used to find γ -ray pulsations, many of which
 1393 were obtained from radio observations (Smith et al. 2019). If the ephemeris does not include the
 1394 uncertainties and for pulsar candidates, we use the ATNF psrcat values. If neither of those exist, we
 1395 use the 0.1° uncertainties from the list maintained by the WVU Astrophysics group²⁰. Ephemeris
 1396 position uncertainties are often underestimated, so we arbitrarily apply a minimum uncertainty of 1
 1397 mas. For GLC from Harris (1996)²¹, the position uncertainties were assigned a typical value of $2''$.

1398 7. CONCLUSIONS

1399 The fourth *Fermi* LAT source catalog is the deepest-yet in the GeV energy range. The increased
 1400 sensitivity relative to the 3FGL catalog is due to both the longer time interval (8 years versus 4
 1401 years) and the use of Pass 8 data, which provides more acceptance over the entire energy range and

¹⁹ <http://tevcat.uchicago.edu/>

²⁰ <http://astro.phys.wvu.edu/GalacticMSPs/GalacticMSPs.txt>

²¹ <https://heasarc.gsfc.nasa.gov/w3browse/all/globclust.html>

1402 a narrower PSF at high energy. The 4FGL catalog also benefits from higher-level improvements in
1403 the analysis, including an improved model for Galactic diffuse emission, a weighted log-likelihood
1404 method to mitigate the systematic effects due to that diffuse emission model, and systematic testing
1405 of three spectral representations, useful to classify unassociated sources.

1406 The 4FGL catalog includes 5065 sources. The sources are detected ($TS > 25$) based on their
1407 average fluxes in the 8-year data set; 1327 of the sources are found to be significantly variable on one-
1408 year timescales, and 1173 on two-month timescales. We mark 92 (1.8%) of the sources as potentially
1409 related to imperfections in the model for Galactic diffuse emission; the character *c* is appended to
1410 their names (except those already marked as *e* for extended). An additional 1071 (21.1%) are flagged
1411 in the catalog for less serious concerns, e.g., for the spectral model having a poor fit or for being close
1412 to a brighter source. Of the 5065 sources in the catalog, 354 (7.0%) are considered identified, based on
1413 pulsations, correlated variability, or correlated angular sizes with observations at other wavelengths.
1414 We find likely lower-energy counterparts for 3374 other sources (66.6%). The remaining 1337 sources
1415 (26.4%) are unassociated.

1416 The identified and associated sources in the 4FGL catalog include many Galactic and extragalactic
1417 source classes. The largest Galactic source class continues to be pulsars, with 229 known γ -ray pulsars
1418 and 10 associations to non-LAT pulsars. Other Galactic source classes have continued to grow; 30
1419 globular clusters, 40 supernova remnants and 17 pulsar wind nebulae are now associated with LAT
1420 sources. Blazars remain the largest class of extragalactic sources, with more than 1800 identified
1421 or associated with BL Lac or FSRQ active galaxies. Non-blazar classes of active galaxies are also
1422 found, including 9 narrow-line Seyfert galaxies, 5 compact steep spectrum radio sources and 42 radio
1423 galaxies. The populations of active galaxies in 4FGL are considered in more detail in the companion
1424 4LAC catalog.

1425 The *Fermi* LAT Collaboration acknowledges generous ongoing support from a number of agencies
1426 and institutes that have supported both the development and the operation of the LAT as well as
1427 scientific data analysis. These include the National Aeronautics and Space Administration and the
1428 Department of Energy in the United States, the Commissariat à l'Énergie Atomique and the Centre
1429 National de la Recherche Scientifique / Institut National de Physique Nucléaire et de Physique des
1430 Particules in France, the Agenzia Spaziale Italiana and the Istituto Nazionale di Fisica Nucleare in
1431 Italy, the Ministry of Education, Culture, Sports, Science and Technology (MEXT), High Energy
1432 Accelerator Research Organization (KEK) and Japan Aerospace Exploration Agency (JAXA) in
1433 Japan, and the K. A. Wallenberg Foundation, the Swedish Research Council and the Swedish National
1434 Space Board in Sweden.

1435 Additional support for science analysis during the operations phase is gratefully acknowledged from
1436 the Istituto Nazionale di Astrofisica in Italy and the Centre National d'Études Spatiales in France.
1437 This work performed in part under DOE Contract DE-AC02-76SF00515.

1438 This work made extensive use of the ATNF pulsar catalog²² (Manchester et al. 2005). This
1439 research has made use of the NASA/IPAC Extragalactic Database (NED) which is operated by
1440 the Jet Propulsion Laboratory, California Institute of Technology, under contract with the National

²² <http://www.atnf.csiro.au/research/pulsar/psrcat>

1441 Aeronautics and Space Administration, and of archival data, software and online services provided
1442 by the ASI Science Data Center (ASDC) operated by the Italian Space Agency.

1443 This research has made use of Aladin²³, TOPCAT²⁴ (Taylor 2005) and APLpy, an open-source
1444 plotting package for Python²⁵ (Robitaille & Bressert 2012). The authors acknowledge the use of
1445 HEALPix²⁶ (Górski et al. 2005). We used the Manitoba SNR catalog (Ferrand & Safi-Harb 2012) to
1446 check recently published extended sources.

1447 *Facility: Fermi-LAT*

REFERENCES

- 1448 Abdo, A. A., Ackermann, M., Ajello, M., et al.
1449 2009a, *Astroparticle Physics*, 32, 193,
1450 doi: [10.1016/j.astropartphys.2009.08.002](https://doi.org/10.1016/j.astropartphys.2009.08.002)
1451 —. 2009b, *ApJL*, 706, L1,
1452 doi: [10.1088/0004-637X/706/1/L1](https://doi.org/10.1088/0004-637X/706/1/L1)
1453 —. 2009c, *ApJS*, 183, 46,
1454 doi: [10.1088/0067-0049/183/1/46](https://doi.org/10.1088/0067-0049/183/1/46)
1455 —. 2009d, *ApJL*, 701, L123,
1456 doi: [10.1088/0004-637X/701/2/L123](https://doi.org/10.1088/0004-637X/701/2/L123)
1457 —. 2010a, *ApJS*, 188, 405,
1458 doi: [10.1088/0067-0049/188/2/405](https://doi.org/10.1088/0067-0049/188/2/405)
1459 —. 2010b, *Science*, 328, 725,
1460 doi: [10.1126/science.1184656](https://doi.org/10.1126/science.1184656)
1461 —. 2010c, *ApJ*, 712, 459,
1462 doi: [10.1088/0004-637X/712/1/459](https://doi.org/10.1088/0004-637X/712/1/459)
1463 —. 2010d, *ApJ*, 713, 146,
1464 doi: [10.1088/0004-637X/713/1/146](https://doi.org/10.1088/0004-637X/713/1/146)
1465 —. 2010e, *ApJ*, 718, 348,
1466 doi: [10.1088/0004-637X/718/1/348](https://doi.org/10.1088/0004-637X/718/1/348)
1467 —. 2010f, *Science*, 327, 1103,
1468 doi: [10.1126/science.1182787](https://doi.org/10.1126/science.1182787)
1469 —. 2010g, *ApJL*, 709, L152,
1470 doi: [10.1088/2041-8205/709/2/L152](https://doi.org/10.1088/2041-8205/709/2/L152)
1471 —. 2010h, *A&A*, 524, A75,
1472 doi: [10.1051/0004-6361/201014458](https://doi.org/10.1051/0004-6361/201014458)
1473 —. 2010i, *ApJ*, 723, 649,
1474 doi: [10.1088/0004-637X/723/1/649](https://doi.org/10.1088/0004-637X/723/1/649)
1475 —. 2010j, *ApJ*, 714, 927,
1476 doi: [10.1088/0004-637X/714/1/927](https://doi.org/10.1088/0004-637X/714/1/927)
1477 —. 2011, *ApJ*, 734, 116,
1478 doi: [10.1088/0004-637X/734/2/116](https://doi.org/10.1088/0004-637X/734/2/116)
- 1479 Abdo, A. A., Ajello, M., Allafort, A., et al. 2013,
1480 *ApJS*, 208, 17,
1481 doi: [10.1088/0067-0049/208/2/17](https://doi.org/10.1088/0067-0049/208/2/17)
1482 Abdollahi, S., Ackermann, M., Ajello, M., et al.
1483 2017, *ApJ*, 846, 34,
1484 doi: [10.3847/1538-4357/aa8092](https://doi.org/10.3847/1538-4357/aa8092)
1485 Abramowski, A., Aharonian, F., Ait Benkhali, F.,
1486 et al. 2015, *A&A*, 574, A27,
1487 doi: [10.1051/0004-6361/201322694](https://doi.org/10.1051/0004-6361/201322694)
1488 Acero, F., Ackermann, M., Ajello, M., et al. 2015,
1489 *ApJS*, 218, 23,
1490 doi: [10.1088/0067-0049/218/2/23](https://doi.org/10.1088/0067-0049/218/2/23)
1491 —. 2016a, *ApJS*, 223, 26,
1492 doi: [10.3847/0067-0049/223/2/26](https://doi.org/10.3847/0067-0049/223/2/26)
1493 —. 2016b, *ApJS*, 224, 8,
1494 doi: [10.3847/0067-0049/224/1/8](https://doi.org/10.3847/0067-0049/224/1/8)
1495 Acero, F., Donato, D., Ojha, R., et al. 2013, *ApJ*,
1496 779, 133, doi: [10.1088/0004-637X/779/2/133](https://doi.org/10.1088/0004-637X/779/2/133)
1497 Ackermann, M., Ajello, M., Albert, A., et al.
1498 2012a, *ApJS*, 203, 4,
1499 doi: [10.1088/0067-0049/203/1/4](https://doi.org/10.1088/0067-0049/203/1/4)
1500 —. 2014a, *ApJ*, 787, 15,
1501 doi: [10.1088/0004-637X/787/1/15](https://doi.org/10.1088/0004-637X/787/1/15)
1502 —. 2014b, *Science*, 345, 554,
1503 doi: [10.1126/science.1253947](https://doi.org/10.1126/science.1253947)
1504 —. 2016a, *PhRvD*, 93, 082001,
1505 doi: [10.1103/PhysRevD.93.082001](https://doi.org/10.1103/PhysRevD.93.082001)
1506 —. 2017a, *ApJ*, 836, 208,
1507 doi: [10.3847/1538-4357/aa5c3d](https://doi.org/10.3847/1538-4357/aa5c3d)
1508 Ackermann, M., Ajello, M., Allafort, A., et al.
1509 2011a, *Science*, 334, 1103
1510 —. 2011b, *ApJ*, 743, 171,
1511 doi: [10.1088/0004-637X/743/2/171](https://doi.org/10.1088/0004-637X/743/2/171)
1512 —. 2012b, *Astroparticle Physics*, 35, 346,
1513 doi: [10.1016/j.astropartphys.2011.10.007](https://doi.org/10.1016/j.astropartphys.2011.10.007)
1514 —. 2012c, *ApJ*, 753, 83,
1515 doi: [10.1088/0004-637X/753/1/83](https://doi.org/10.1088/0004-637X/753/1/83)

²³ <http://aladin.u-strasbg.fr/>

²⁴ <http://www.star.bristol.ac.uk/~mbt/topcat/>

²⁵ <http://aplpy.github.com>

²⁶ <http://healpix.jpl.nasa.gov/>

- 1516 —. 2013, *ApJS*, 209, 34,
 1517 doi: [10.1088/0067-0049/209/2/34](https://doi.org/10.1088/0067-0049/209/2/34)
- 1518 Ackermann, M., Ajello, M., Atwood, W. B., et al.
 1519 2012d, *ApJ*, 750, 3,
 1520 doi: [10.1088/0004-637X/750/1/3](https://doi.org/10.1088/0004-637X/750/1/3)
- 1521 —. 2012e, *ApJ*, 761, 91,
 1522 doi: [10.1088/0004-637X/761/2/91](https://doi.org/10.1088/0004-637X/761/2/91)
- 1523 —. 2015, *ApJ*, 810, 14,
 1524 doi: [10.1088/0004-637X/810/1/14](https://doi.org/10.1088/0004-637X/810/1/14)
- 1525 —. 2016b, *ApJS*, 222, 5,
 1526 doi: [10.3847/0067-0049/222/1/5](https://doi.org/10.3847/0067-0049/222/1/5)
- 1527 Ackermann, M., Ajello, M., Baldini, L., et al.
 1528 2011c, *ApJ*, 726, 35,
 1529 doi: [10.1088/0004-637X/726/1/35](https://doi.org/10.1088/0004-637X/726/1/35)
- 1530 —. 2016c, *ApJ*, 826, 1,
 1531 doi: [10.3847/0004-637X/826/1/1](https://doi.org/10.3847/0004-637X/826/1/1)
- 1532 —. 2017b, *ApJ*, 843, 139,
 1533 doi: [10.3847/1538-4357/aa775a](https://doi.org/10.3847/1538-4357/aa775a)
- 1534 —. 2018, *ApJS*, 237, 32,
 1535 doi: [10.3847/1538-4365/aacdf7](https://doi.org/10.3847/1538-4365/aacdf7)
- 1536 Ackermann, M., Albert, A., Atwood, W. B., et al.
 1537 2016d, *A&A*, 586, A71,
 1538 doi: [10.1051/0004-6361/201526920](https://doi.org/10.1051/0004-6361/201526920)
- 1539 Aharonian, F., Akhperjanian, A. G., Aye, K.-M.,
 1540 et al. 2005, *A&A*, 439, 1013,
 1541 doi: [10.1051/0004-6361:20053195](https://doi.org/10.1051/0004-6361:20053195)
- 1542 Aharonian, F., Akhperjanian, A. G., Barres de
 1543 Almeida, U., et al. 2008, *A&A*, 477, 353,
 1544 doi: [10.1051/0004-6361:20078516](https://doi.org/10.1051/0004-6361:20078516)
- 1545 Ajello, M., Allafort, A., Baldini, L., et al. 2012,
 1546 *ApJ*, 744, 80, doi: [10.1088/0004-637X/744/1/80](https://doi.org/10.1088/0004-637X/744/1/80)
- 1547 Ajello, M., Arimoto, M., Axelsson, M., et al. 2019,
 1548 *ApJ*, 878, 52, doi: [10.3847/1538-4357/ab1d4e](https://doi.org/10.3847/1538-4357/ab1d4e)
- 1549 Ajello, M., Atwood, W. B., Baldini, L., et al. 2017,
 1550 *ApJS*, 232, 18, doi: [10.3847/1538-4365/aa8221](https://doi.org/10.3847/1538-4365/aa8221)
- 1551 Ajello, M., Baldini, L., Barbiellini, G., et al. 2016,
 1552 *ApJ*, 819, 98, doi: [10.3847/0004-637X/819/2/98](https://doi.org/10.3847/0004-637X/819/2/98)
- 1553 Allafort, A., Baldini, L., Ballet, J., et al. 2013,
 1554 *ApJL*, 777, L2,
 1555 doi: [10.1088/2041-8205/777/1/L2](https://doi.org/10.1088/2041-8205/777/1/L2)
- 1556 Álvarez Crespo, N., Masetti, N., Ricci, F., et al.
 1557 2016a, *AJ*, 151, 32,
 1558 doi: [10.3847/0004-6256/151/2/32](https://doi.org/10.3847/0004-6256/151/2/32)
- 1559 Álvarez Crespo, N., Massaro, F., Milisavljevic, D.,
 1560 et al. 2016b, *AJ*, 151, 95,
 1561 doi: [10.3847/0004-6256/151/4/95](https://doi.org/10.3847/0004-6256/151/4/95)
- 1562 Álvarez Crespo, N., Massaro, F., D'Abrusco, R.,
 1563 et al. 2016c, *Ap&SS*, 361, 316,
 1564 doi: [10.1007/s10509-016-2902-1](https://doi.org/10.1007/s10509-016-2902-1)
- 1565 Araya, M. 2014, *MNRAS*, 444, 860,
 1566 doi: [10.1093/mnras/stu1484](https://doi.org/10.1093/mnras/stu1484)
- 1567 Araya, M. 2017, *ApJ*, 843, 12,
 1568 doi: [10.3847/1538-4357/aa7261](https://doi.org/10.3847/1538-4357/aa7261)
- 1569 Araya, M. 2018a, *MNRAS*, 474, 102,
 1570 doi: [10.1093/mnras/stx2779](https://doi.org/10.1093/mnras/stx2779)
- 1571 —. 2018b, *ApJ*, 859, 69,
 1572 doi: [10.3847/1538-4357/aabd7e](https://doi.org/10.3847/1538-4357/aabd7e)
- 1573 Arsioli, B., Fraga, B., Giommi, P., Padovani, P., &
 1574 Marrese, P. M. 2015, *A&A*, 579, A34,
 1575 doi: [10.1051/0004-6361/201424148](https://doi.org/10.1051/0004-6361/201424148)
- 1576 Arsioli, B., & Polenta, G. 2018, *A&A*, 616, A20,
 1577 doi: [10.1051/0004-6361/201832786](https://doi.org/10.1051/0004-6361/201832786)
- 1578 Atwood, W. B., Abdo, A. A., Ackermann, M.,
 1579 et al. 2009, *ApJ*, 697, 1071,
 1580 doi: [10.1088/0004-637X/697/2/1071](https://doi.org/10.1088/0004-637X/697/2/1071)
- 1581 Atwood, W. B., Albert, A., Baldini, L., et al.
 1582 2013, Fermi Symposium proceedings - eConf
 1583 C121028. <https://arxiv.org/abs/1303.3514>
- 1584 Ballet, J., et al. 2015, in *ICRC*, Vol. 34, *ICRC*
 1585 2015, ed. A. S. Borisov et al., 848
- 1586 Baltz, E. A., Taylor, J. E., & Wai, L. L. 2007,
 1587 *ApJ*, 659, L125, doi: [10.1086/517882](https://doi.org/10.1086/517882)
- 1588 Berton, M., Foschini, L., Ciroi, S., et al. 2015,
 1589 *A&A*, 578, A28,
 1590 doi: [10.1051/0004-6361/201525691](https://doi.org/10.1051/0004-6361/201525691)
- 1591 Bird, A. J., Bazzano, A., Malizia, A., et al. 2016,
 1592 *ApJS*, 223, 15,
 1593 doi: [10.3847/0067-0049/223/1/15](https://doi.org/10.3847/0067-0049/223/1/15)
- 1594 Bregeon, J., Charles, E., & Wood, M. 2013, Fermi
 1595 Symposium proceedings - eConf C121028.
 1596 <https://arxiv.org/abs/1304.5456>
- 1597 Bruel, P., Burnett, T. H., Digel, S. W., et al. 2018,
 1598 8th Fermi Symposium.
 1599 <https://arxiv.org/abs/1810.11394>
- 1600 Buehler, R., Scargle, J. D., Blandford, R. D.,
 1601 et al. 2012, *ApJ*, 749, 26,
 1602 doi: [10.1088/0004-637X/749/1/26](https://doi.org/10.1088/0004-637X/749/1/26)
- 1603 Bulgarelli, A., Fioretti, V., Parmiggiani, N., et al.
 1604 2019, *A&A*, 627, A13,
 1605 doi: [10.1051/0004-6361/201834143](https://doi.org/10.1051/0004-6361/201834143)
- 1606 Capetti, A., Massaro, F., & Baldi, R. D. 2017a,
 1607 *A&A*, 598, A49,
 1608 doi: [10.1051/0004-6361/201629287](https://doi.org/10.1051/0004-6361/201629287)
- 1609 —. 2017b, *A&A*, 601, A81,
 1610 doi: [10.1051/0004-6361/201630247](https://doi.org/10.1051/0004-6361/201630247)
- 1611 Caputo, R., Buckley, M. R., Martin, P., et al.
 1612 2016, *PhRvD*, 93, 062004,
 1613 doi: [10.1103/PhysRevD.93.062004](https://doi.org/10.1103/PhysRevD.93.062004)

- 1614 Casandjian, J.-M., & Grenier, I. A. 2008, *A&A*,
1615 489, 849, doi: [10.1051/0004-6361:200809685](https://doi.org/10.1051/0004-6361:200809685)
- 1616 Chang, Y.-L., Arsioli, B., Giommi, P., &
1617 Padovani, P. 2017, *A&A*, 598, A17,
1618 doi: [10.1051/0004-6361/201629487](https://doi.org/10.1051/0004-6361/201629487)
- 1619 Cheung, C. C., Donato, D., Gehrels, N.,
1620 Sokolovsky, K. V., & Giroletti, M. 2012, *ApJ*,
1621 756, 33, doi: [10.1088/0004-637X/756/1/33](https://doi.org/10.1088/0004-637X/756/1/33)
- 1622 Cheung, C. C., Jean, P., Shore, S. N., et al. 2016,
1623 *ApJ*, 826, 142,
1624 doi: [10.3847/0004-637X/826/2/142](https://doi.org/10.3847/0004-637X/826/2/142)
- 1625 Chiaro, G., Salvetti, D., La Mura, G., et al. 2016,
1626 *MNRAS*, 462, 3180,
1627 doi: [10.1093/mnras/stw1830](https://doi.org/10.1093/mnras/stw1830)
- 1628 Condon, J. J., Cotton, W. D., Greisen, E. W.,
1629 et al. 1998, *AJ*, 115, 1693, doi: [10.1086/300337](https://doi.org/10.1086/300337)
- 1630 Coronado-Blázquez, J., Sánchez-Conde, M. A.,
1631 Domínguez, A., et al. 2019, *Journal of*
1632 *Cosmology and Astroparticle Physics*, 2019,
1633 020, doi: [10.1088/1475-7516/2019/07/020](https://doi.org/10.1088/1475-7516/2019/07/020)
- 1634 Cowperthwaite, P. S., Massaro, F., D'Abrusco, R.,
1635 et al. 2013, *AJ*, 146, 110,
1636 doi: [10.1088/0004-6256/146/5/110](https://doi.org/10.1088/0004-6256/146/5/110)
- 1637 D'Abrusco, R., Massaro, F., Paggi, A., et al. 2014,
1638 *ApJS*, 215, 14,
1639 doi: [10.1088/0067-0049/215/1/14](https://doi.org/10.1088/0067-0049/215/1/14)
- 1640 de Ruiter, H. R., Willis, A. G., & Arp, H. C. 1977,
1641 *A&AS*, 28, 211
- 1642 Devin, J., Acero, F., Ballet, J., & Schmid, J. 2018,
1643 *A&A*, 617, A5,
1644 doi: [10.1051/0004-6361/201833008](https://doi.org/10.1051/0004-6361/201833008)
- 1645 Doert, M., & Errando, M. 2014, *ApJ*, 782, 41,
1646 doi: [10.1088/0004-637X/782/1/41](https://doi.org/10.1088/0004-637X/782/1/41)
- 1647 Fermi-LAT collaboration. 2019, arXiv:1905.10771.
1648 <https://arxiv.org/abs/1905.10771>
- 1649 Ferrand, G., & Safi-Harb, S. 2012, *Advances in*
1650 *Space Research*, 49, 1313,
1651 doi: [10.1016/j.asr.2012.02.004](https://doi.org/10.1016/j.asr.2012.02.004)
- 1652 Garcia, F., Chaty, S., & Fortin, F. 2019, to be
1653 submitted to *A&A*
- 1654 Giommi, P., Polenta, G., Lähteenmäki, A., et al.
1655 2012, *A&A*, 541, A160,
1656 doi: [10.1051/0004-6361/201117825](https://doi.org/10.1051/0004-6361/201117825)
- 1657 Giroletti, M., Massaro, F., D'Abrusco, R., et al.
1658 2016, *A&A*, 588, A141,
1659 doi: [10.1051/0004-6361/201527817](https://doi.org/10.1051/0004-6361/201527817)
- 1660 Górski, K. M., Hivon, E., Banday, A. J., et al.
1661 2005, *ApJ*, 622, 759, doi: [10.1086/427976](https://doi.org/10.1086/427976)
- 1662 Green, D. A. 2014, *Bulletin of the Astronomical*
1663 *Society of India*, 42, 47.
1664 <https://arxiv.org/abs/1409.0637>
- 1665 Grenier, I. A., Casandjian, J.-M., & Terrier, R.
1666 2005, *Science*, 307, 1292,
1667 doi: [10.1126/science.1106924](https://doi.org/10.1126/science.1106924)
- 1668 Griffin, R. D., Dai, X., & Thompson, T. A. 2016,
1669 *ApJL*, 823, L17,
1670 doi: [10.3847/2041-8205/823/1/L17](https://doi.org/10.3847/2041-8205/823/1/L17)
- 1671 Grondin, M.-H., Funk, S., Lemoine-Goumard, M.,
1672 et al. 2011, *ApJ*, 738, 42,
1673 doi: [10.1088/0004-637X/738/1/42](https://doi.org/10.1088/0004-637X/738/1/42)
- 1674 H. E. S. S. Collaboration, Abdalla, H.,
1675 Abramowski, A., et al. 2018a, *A&A*, 612, A6,
1676 doi: [10.1051/0004-6361/201629790](https://doi.org/10.1051/0004-6361/201629790)
- 1677 —. 2018b, *A&A*, 619, A71,
1678 doi: [10.1051/0004-6361/201832640](https://doi.org/10.1051/0004-6361/201832640)
- 1679 Hanabata, Y., Katagiri, H., Hewitt, J. W., et al.
1680 2014, *ApJ*, 786, 145,
1681 doi: [10.1088/0004-637X/786/2/145](https://doi.org/10.1088/0004-637X/786/2/145)
- 1682 Harris, W. E. 1996, *AJ*, 112, 1487,
1683 doi: [10.1086/118116](https://doi.org/10.1086/118116)
- 1684 Hartman, R. C., Bertsch, D. L., Bloom, S. D.,
1685 et al. 1999, *ApJS*, 123, 79, doi: [10.1086/313231](https://doi.org/10.1086/313231)
- 1686 Hassan, T., Mirabal, N., Contreras, J. L., & Oya,
1687 I. 2013, *MNRAS*, 428, 220,
1688 doi: [10.1093/mnras/sts022](https://doi.org/10.1093/mnras/sts022)
- 1689 Hayashida, M., Stawarz, Ł., Cheung, C. C., et al.
1690 2013, *ApJ*, 779, 131,
1691 doi: [10.1088/0004-637X/779/2/131](https://doi.org/10.1088/0004-637X/779/2/131)
- 1692 Healey, S. E., Romani, R. W., Cotter, G., et al.
1693 2008, *ApJS*, 175, 97, doi: [10.1086/523302](https://doi.org/10.1086/523302)
- 1694 Healey, S. E., Romani, R. W., Taylor, G. B., et al.
1695 2007, *ApJS*, 171, 61, doi: [10.1086/513742](https://doi.org/10.1086/513742)
- 1696 HI4PI Collaboration, Ben Bekhti, N., Flöer, L.,
1697 et al. 2016, *A&A*, 594, A116,
1698 doi: [10.1051/0004-6361/201629178](https://doi.org/10.1051/0004-6361/201629178)
- 1699 Hovatta, T., Lister, M. L., Aller, M. F., et al.
1700 2012, *AJ*, 144, 105,
1701 doi: [10.1088/0004-6256/144/4/105](https://doi.org/10.1088/0004-6256/144/4/105)
- 1702 Hovatta, T., Aller, M. F., Aller, H. D., et al. 2014,
1703 *AJ*, 147, 143, doi: [10.1088/0004-6256/147/6/143](https://doi.org/10.1088/0004-6256/147/6/143)
- 1704 Hu, F., & Zidek, J. V. 2002, *Canad. J. Statist.*,
1705 30, 347
- 1706 Johannesson, G., Orlando, E., & the Fermi-LAT
1707 collaboration. 2013, ICRC proceedings.
1708 <https://arxiv.org/abs/1307.0197>
- 1709 Johnson, T. J., Ray, P. S., Roy, J., et al. 2015,
1710 *ApJ*, 806, 91, doi: [10.1088/0004-637X/806/1/91](https://doi.org/10.1088/0004-637X/806/1/91)

- 1711 Katagiri, H., Tibaldo, L., Ballet, J., et al. 2011,
 1712 ApJ, 741, 44, doi: [10.1088/0004-637X/741/1/44](https://doi.org/10.1088/0004-637X/741/1/44)
 1713 Katagiri, H., Yoshida, K., Ballet, J., et al. 2016a,
 1714 ApJ, 818, 114,
 1715 doi: [10.3847/0004-637X/818/2/114](https://doi.org/10.3847/0004-637X/818/2/114)
 1716 Katagiri, H., Sugiyama, S., Ackermann, M., et al.
 1717 2016b, ApJ, 831, 106,
 1718 doi: [10.3847/0004-637X/831/1/106](https://doi.org/10.3847/0004-637X/831/1/106)
 1719 Kataoka, J., Yatsu, Y., Kawai, N., et al. 2012,
 1720 ApJ, 757, 176,
 1721 doi: [10.1088/0004-637X/757/2/176](https://doi.org/10.1088/0004-637X/757/2/176)
 1722 Katsuta, J., Uchiyama, Y., Tanaka, T., et al.
 1723 2012, ApJ, 752, 135,
 1724 doi: [10.1088/0004-637X/752/2/135](https://doi.org/10.1088/0004-637X/752/2/135)
 1725 Kerr, M. 2010, PhD thesis, University of
 1726 Washington, ArXiv:1101:6072.
 1727 <https://arxiv.org/abs/1101:6072>
 1728 Kovalev, Y. Y. 2009, ApJ, 707, L56,
 1729 doi: [10.1088/0004-637X/707/1/L56](https://doi.org/10.1088/0004-637X/707/1/L56)
 1730 Kuiper, L., Hermsen, W., Krijger, J. M., et al.
 1731 1999, A&A, 351, 119.
 1732 <https://arxiv.org/abs/astro-ph/9903474>
 1733 Kuźmicz, A., Jamroz, M., Bronarska, K.,
 1734 Janda-Boczar, K., & Saikia, D. J. 2018, ApJS,
 1735 238, 9, doi: [10.3847/1538-4365/aad9ff](https://doi.org/10.3847/1538-4365/aad9ff)
 1736 Lande, J., Ackermann, M., Allafort, A., et al.
 1737 2012, ApJ, 756, 5,
 1738 doi: [10.1088/0004-637X/756/1/5](https://doi.org/10.1088/0004-637X/756/1/5)
 1739 Landi, R., Bassani, L., Stephen, J. B., et al. 2015,
 1740 A&A, 581, A57,
 1741 doi: [10.1051/0004-6361/201526221](https://doi.org/10.1051/0004-6361/201526221)
 1742 Landoni, M., Falomo, R., Treves, A., Scarpa, R.,
 1743 & Reverte Payá, D. 2015a, AJ, 150, 181,
 1744 doi: [10.1088/0004-6256/150/6/181](https://doi.org/10.1088/0004-6256/150/6/181)
 1745 Landoni, M., Paiano, S., Falomo, R., Scarpa, R.,
 1746 & Treves, A. 2018, ApJ, 861, 130,
 1747 doi: [10.3847/1538-4357/aac77c](https://doi.org/10.3847/1538-4357/aac77c)
 1748 Landoni, M., Massaro, F., Paggi, A., et al. 2015b,
 1749 AJ, 149, 163, doi: [10.1088/0004-6256/149/5/163](https://doi.org/10.1088/0004-6256/149/5/163)
 1750 Li, J., Rea, N., Torres, D. F., & de Oña-Wilhelmi,
 1751 E. 2017a, ApJ, 835, 30,
 1752 doi: [10.3847/1538-4357/835/1/30](https://doi.org/10.3847/1538-4357/835/1/30)
 1753 Li, J., Torres, D. F., Cheng, K. S., et al. 2017b,
 1754 ApJ, 846, 169, doi: [10.3847/1538-4357/aa7ff7](https://doi.org/10.3847/1538-4357/aa7ff7)
 1755 Liu, Q. Z., van Paradijs, J., & van den Heuvel,
 1756 E. P. J. 2007, VizieR Online Data Catalog, 346,
 1757 90807
 1758 López-Caniego, M., González-Nuevo, J., Massardi,
 1759 M., et al. 2013, MNRAS, 430, 1566,
 1760 doi: [10.1093/mnras/sts680](https://doi.org/10.1093/mnras/sts680)
 1761 Maeda, K., Kataoka, J., Nakamori, T., et al. 2011,
 1762 ApJ, 729, 103,
 1763 doi: [10.1088/0004-637X/729/2/103](https://doi.org/10.1088/0004-637X/729/2/103)
 1764 Manchester, R. N., Hobbs, G. B., Teoh, A., &
 1765 Hobbs, M. 2005, AJ, 129, 1993,
 1766 doi: [10.1086/428488](https://doi.org/10.1086/428488)
 1767 Marchesi, S., Kaur, A., & Ajello, M. 2018, AJ,
 1768 156, 212, doi: [10.3847/1538-3881/aae201](https://doi.org/10.3847/1538-3881/aae201)
 1769 Marchesini, E. J., Peña-Herazo, H. A., Álvarez
 1770 Crespo, N., et al. 2019, Ap&SS, 364, 5,
 1771 doi: [10.1007/s10509-018-3490-z](https://doi.org/10.1007/s10509-018-3490-z)
 1772 Maselli, A., Massaro, F., D’Abrusco, R., et al.
 1773 2015, Ap&SS, 357, 141,
 1774 doi: [10.1007/s10509-015-2372-x](https://doi.org/10.1007/s10509-015-2372-x)
 1775 Massaro, E., Giommi, P., Leto, C., et al. 2009,
 1776 A&A, 495, 691,
 1777 doi: [10.1051/0004-6361:200810161](https://doi.org/10.1051/0004-6361:200810161)
 1778 Massaro, F., & D’Abrusco, R. 2016, ApJ, 827, 67,
 1779 doi: [10.3847/0004-637X/827/1/67](https://doi.org/10.3847/0004-637X/827/1/67)
 1780 Massaro, F., D’Abrusco, R., Ajello, M., Grindlay,
 1781 J. E., & Smith, H. A. 2011, ApJ, 740, L48,
 1782 doi: [10.1088/2041-8205/740/2/L48](https://doi.org/10.1088/2041-8205/740/2/L48)
 1783 Massaro, F., D’Abrusco, R., Giroletti, M., et al.
 1784 2013, ApJS, 207, 4,
 1785 doi: [10.1088/0067-0049/207/1/4](https://doi.org/10.1088/0067-0049/207/1/4)
 1786 Massaro, F., D’Abrusco, R., Tosti, G., et al.
 1787 2012a, ApJ, 750, 138,
 1788 doi: [10.1088/0004-637X/750/2/138](https://doi.org/10.1088/0004-637X/750/2/138)
 1789 —. 2012b, ApJ, 752, 61,
 1790 doi: [10.1088/0004-637X/752/1/61](https://doi.org/10.1088/0004-637X/752/1/61)
 1791 Massaro, F., Landoni, M., D’Abrusco, R., et al.
 1792 2015a, A&A, 575, A124,
 1793 doi: [10.1051/0004-6361/201425119](https://doi.org/10.1051/0004-6361/201425119)
 1794 Massaro, F., Masetti, N., D’Abrusco, R., Paggi,
 1795 A., & Funk, S. 2014, AJ, 148, 66,
 1796 doi: [10.1088/0004-6256/148/4/66](https://doi.org/10.1088/0004-6256/148/4/66)
 1797 Massaro, F., D’Abrusco, R., Landoni, M., et al.
 1798 2015b, ApJS, 217, 2,
 1799 doi: [10.1088/0067-0049/217/1/2](https://doi.org/10.1088/0067-0049/217/1/2)
 1800 Massaro, F., Álvarez Crespo, N., D’Abrusco, R.,
 1801 et al. 2016, Ap&SS, 361, 337,
 1802 doi: [10.1007/s10509-016-2926-6](https://doi.org/10.1007/s10509-016-2926-6)
 1803 Mattox, J. R., Bertsch, D. L., Chiang, J., et al.
 1804 1996, ApJ, 461, 396, doi: [10.1086/177068](https://doi.org/10.1086/177068)
 1805 Mattox, J. R., Wagner, S. J., Malkan, M., et al.
 1806 1997, ApJ, 476, 692, doi: [10.1086/303639](https://doi.org/10.1086/303639)
 1807 Mauch, T., Murphy, T., Buttery, H. J., et al.
 1808 2003, MNRAS, 342, 1117,
 1809 doi: [10.1046/j.1365-8711.2003.06605.x](https://doi.org/10.1046/j.1365-8711.2003.06605.x)

- 1810 McConnachie, A. W. 2012, *AJ*, 144, 4,
1811 doi: [10.1088/0004-6256/144/1/4](https://doi.org/10.1088/0004-6256/144/1/4)
- 1812 Mereghetti, S., Palombara, N. L., Tiengo, A.,
1813 et al. 2011, *ApJ*, 737, 51,
1814 doi: [10.1088/0004-637x/737/2/51](https://doi.org/10.1088/0004-637x/737/2/51)
- 1815 Mirabal, N., & Halpern, J. P. 2009, *ApJ*, 701,
1816 L129, doi: [10.1088/0004-637X/701/2/L129](https://doi.org/10.1088/0004-637X/701/2/L129)
- 1817 Murphy, T., Sadler, E. M., Ekers, R. D., et al.
1818 2010, *MNRAS*, 402, 2403,
1819 doi: [10.1111/j.1365-2966.2009.15961.x](https://doi.org/10.1111/j.1365-2966.2009.15961.x)
- 1820 Napier, P. J., Bagri, D. S., Clark, B. G., et al.
1821 1994, *IEEE Proceedings*, 82, 658
- 1822 Nolan, P. L., Abdo, A. A., Ackermann, M., et al.
1823 2012, *ApJS*, 199, 31,
1824 doi: [10.1088/0067-0049/199/2/31](https://doi.org/10.1088/0067-0049/199/2/31)
- 1825 Nori, M., Giroletti, M., Massaro, F., et al. 2014,
1826 *ApJS*, 212, 3, doi: [10.1088/0067-0049/212/1/3](https://doi.org/10.1088/0067-0049/212/1/3)
- 1827 Oh, K., Koss, M., Markwardt, C. B., et al. 2018,
1828 *ApJS*, 235, 4, doi: [10.3847/1538-4365/aaa7fd](https://doi.org/10.3847/1538-4365/aaa7fd)
- 1829 Orlando, E., & Strong, A. W. 2008, *Astronomy*
1830 *and Astrophysics*, 480, 847,
1831 doi: [10.1051/0004-6361:20078817](https://doi.org/10.1051/0004-6361:20078817)
- 1832 Paggi, A., Massaro, F., D'Abrusco, R., et al. 2013,
1833 *ApJS*, 209, 9, doi: [10.1088/0067-0049/209/1/9](https://doi.org/10.1088/0067-0049/209/1/9)
- 1834 Paggi, A., Milisavljevic, D., Masetti, N., et al.
1835 2014, *AJ*, 147, 112,
1836 doi: [10.1088/0004-6256/147/5/112](https://doi.org/10.1088/0004-6256/147/5/112)
- 1837 Paiano, S., Falomo, R., Franceschini, A., Treves,
1838 A., & Scarpa, R. 2017a, *ApJ*, 851, 135,
1839 doi: [10.3847/1538-4357/aa9af4](https://doi.org/10.3847/1538-4357/aa9af4)
- 1840 Paiano, S., Franceschini, A., & Stamerra, A.
1841 2017b, *MNRAS*, 468, 4902,
1842 doi: [10.1093/mnras/stx749](https://doi.org/10.1093/mnras/stx749)
- 1843 Paiano, S., Landoni, M., Falomo, R., Treves, A.,
1844 & Scarpa, R. 2017c, *ApJ*, 844, 120,
1845 doi: [10.3847/1538-4357/aa7aac](https://doi.org/10.3847/1538-4357/aa7aac)
- 1846 Paiano, S., Landoni, M., Falomo, R., et al. 2017d,
1847 *ApJ*, 837, 144,
1848 doi: [10.3847/1538-4357/837/2/144](https://doi.org/10.3847/1538-4357/837/2/144)
- 1849 Paladini, R., Burigana, C., Davies, R. D., et al.
1850 2003, *A&A*, 397, 213,
1851 doi: [10.1051/0004-6361:20021466](https://doi.org/10.1051/0004-6361:20021466)
- 1852 Peña-Herazo, H. A., Marchesini, E. J., Álvarez
1853 Crespo, N., et al. 2017, *Ap&SS*, 362, 228,
1854 doi: [10.1007/s10509-017-3208-7](https://doi.org/10.1007/s10509-017-3208-7)
- 1855 Pellizzoni, A., Pilia, M., Possenti, A., et al. 2009,
1856 *ApJL*, 695, L115,
1857 doi: [10.1088/0004-637X/695/1/L115](https://doi.org/10.1088/0004-637X/695/1/L115)
- 1858 Peng, F.-K., Wang, X.-Y., Liu, R.-Y., Tang,
1859 Q.-W., & Wang, J.-F. 2016, *ApJL*, 821, L20,
1860 doi: [10.3847/2041-8205/821/2/L20](https://doi.org/10.3847/2041-8205/821/2/L20)
- 1861 Petrov, L., Mahony, E. K., Edwards, P. G., et al.
1862 2013, *MNRAS*, 432, 1294,
1863 doi: [10.1093/mnras/stt550](https://doi.org/10.1093/mnras/stt550)
- 1864 Petrov, L., Phillips, C., Bertarini, A., Murphy, T.,
1865 & Sadler, E. M. 2011, *MNRAS*, 414, 2528,
1866 doi: [10.1111/j.1365-2966.2011.18570.x](https://doi.org/10.1111/j.1365-2966.2011.18570.x)
- 1867 Pivato, G., Hewitt, J. W., Tibaldo, L., et al. 2013,
1868 *ApJ*, 779, 179,
1869 doi: [10.1088/0004-637X/779/2/179](https://doi.org/10.1088/0004-637X/779/2/179)
- 1870 Planck Collaboration, Aghanim, N., Ashdown, M.,
1871 et al. 2016, *A&A*, 596, A109,
1872 doi: [10.1051/0004-6361/201629022](https://doi.org/10.1051/0004-6361/201629022)
- 1873 Popov, S. B., Mereghetti, S., Blinnikov, S. I.,
1874 Kuranov, A. G., & Yungelson, L. R. 2018,
1875 *MNRAS*, 474, 2750, doi: [10.1093/mnras/stx2910](https://doi.org/10.1093/mnras/stx2910)
- 1876 Porter, T. A., Jóhannesson, G., & Moskalenko,
1877 I. V. 2017, *ApJ*, 846, 67,
1878 doi: [10.3847/1538-4357/aa844d](https://doi.org/10.3847/1538-4357/aa844d)
- 1879 Principe, G., Malyshev, D., Ballet, J., & Funk, S.
1880 2018, *A&A*, 618, A22,
1881 doi: [10.1051/0004-6361/201833116](https://doi.org/10.1051/0004-6361/201833116)
- 1882 Rakshit, S., Stalin, C. S., Chand, H., & Zhang,
1883 X.-G. 2017, *ApJS*, 229, 39,
1884 doi: [10.3847/1538-4365/aa6971](https://doi.org/10.3847/1538-4365/aa6971)
- 1885 Reitberger, K., Reimer, A., Reimer, O., &
1886 Takahashi, H. 2015, *A&A*, 577, A100,
1887 doi: [10.1051/0004-6361/201525726](https://doi.org/10.1051/0004-6361/201525726)
- 1888 Ricci, F., Massaro, F., Landoni, M., et al. 2015,
1889 *AJ*, 149, 160, doi: [10.1088/0004-6256/149/5/160](https://doi.org/10.1088/0004-6256/149/5/160)
- 1890 Robitaille, T., & Bressert, E. 2012, *APLpy*:
1891 *Astronomical Plotting Library in Python*,
1892 *Astrophysics Source Code Library*.
1893 <http://ascl.net/1208.017>
- 1894 Sanders, D. B., Mazzeella, J. M., Kim, D.-C.,
1895 Surace, J. A., & Soifer, B. T. 2003, *AJ*, 126,
1896 1607, doi: [10.1086/376841](https://doi.org/10.1086/376841)
- 1897 Saz Parkinson, P., Limyansky, B., Clark, C.,
1898 Marelli, M., & Abdollahi, S. 2018, *Discovery of*
1899 *two energetic gamma-ray pulsars powering*
1900 *supernova remnants MSH 11-62 and CTB 37A*
- 1901 Schinzel, F. K., Petrov, L., Taylor, G. B., &
1902 Edwards, P. G. 2017, *ApJ*, 838, 139,
1903 doi: [10.3847/1538-4357/aa6439](https://doi.org/10.3847/1538-4357/aa6439)
- 1904 Schinzel, F. K., Petrov, L., Taylor, G. B., et al.
1905 2015, *ApJS*, 217, 4,
1906 doi: [10.1088/0067-0049/217/1/4](https://doi.org/10.1088/0067-0049/217/1/4)

- 1907 Schmidt, K., Priebe, A., & Boller, T. 1993,
1908 *Astronomische Nachrichten*, 314, 371
- 1909 Shahbaz, T., & Watson, C. A. 2007, *A&A*, 474,
1910 969, doi: [10.1051/0004-6361:20078251](https://doi.org/10.1051/0004-6361:20078251)
- 1911 Shaw, M. S., Filippenko, A. V., Romani, R. W.,
1912 Cenko, S. B., & Li, W. 2013a, *AJ*, 146, 127,
1913 doi: [10.1088/0004-6256/146/5/127](https://doi.org/10.1088/0004-6256/146/5/127)
- 1914 Shaw, M. S., Romani, R. W., Cotter, G., et al.
1915 2013b, *ApJ*, 764, 135,
1916 doi: [10.1088/0004-637X/764/2/135](https://doi.org/10.1088/0004-637X/764/2/135)
- 1917 Smith, D. A., Bruel, P., Cognard, I., et al. 2019,
1918 *ApJ*, 871, 78, doi: [10.3847/1538-4357/aaf57d](https://doi.org/10.3847/1538-4357/aaf57d)
- 1919 Stappers, B. W., Archibald, A. M., Hessels,
1920 J. W. T., et al. 2014, *ApJ*, 790, 39,
1921 doi: [10.1088/0004-637X/790/1/39](https://doi.org/10.1088/0004-637X/790/1/39)
- 1922 Stroh, M. C., & Falcone, A. D. 2013, *ApJS*, 207,
1923 28, doi: [10.1088/0067-0049/207/2/28](https://doi.org/10.1088/0067-0049/207/2/28)
- 1924 Takahashi, Y., Kataoka, J., Nakamori, T., et al.
1925 2012, *ApJ*, 747, 64,
1926 doi: [10.1088/0004-637X/747/1/64](https://doi.org/10.1088/0004-637X/747/1/64)
- 1927 Takeuchi, Y., Kataoka, J., Maeda, K., et al. 2013,
1928 *ApJS*, 208, 25,
1929 doi: [10.1088/0067-0049/208/2/25](https://doi.org/10.1088/0067-0049/208/2/25)
- 1930 Tang, Q.-W., Wang, X.-Y., & Tam, P.-H. T. 2014,
1931 *ApJ*, 794, 26, doi: [10.1088/0004-637X/794/1/26](https://doi.org/10.1088/0004-637X/794/1/26)
- 1932 Taylor, M. B. 2005, in *Astronomical Society of the*
1933 *Pacific Conference Series*, Vol. 347,
1934 *Astronomical Data Analysis Software and*
1935 *Systems XIV*, ed. P. Shopbell, M. Britton, &
1936 R. Ebert, 29
- 1937 Véron-Cetty, M.-P., & Véron, P. 2010, *A&A*, 518,
1938 A10, doi: [10.1051/0004-6361/201014188](https://doi.org/10.1051/0004-6361/201014188)
- 1939 Voges, W., Aschenbach, B., Boller, T., et al. 1999,
1940 *A&A*, 349, 389
- 1941 —. 2000, *VizieR Online Data Catalog*, 9029
- 1942 Yeung, P. K. H., Kong, A. K. H., Tam, P. H. T.,
1943 et al. 2017, *ApJ*, 837, 69,
1944 doi: [10.3847/1538-4357/aa5df1](https://doi.org/10.3847/1538-4357/aa5df1)
- 1945 —. 2016, *ApJ*, 827, 41,
1946 doi: [10.3847/0004-637X/827/1/41](https://doi.org/10.3847/0004-637X/827/1/41)
- 1947 Yoast-Hull, T. M., Gallagher, John S., I., Aalto,
1948 S., & Varenus, E. 2017, *MNRAS*, 469, L89,
1949 doi: [10.1093/mnras/slx054](https://doi.org/10.1093/mnras/slx054)
- 1950 Zanin, R., Fernández-Barral, A., de Oña
1951 Wilhelmi, E., et al. 2016, *A&A*, 596, A55,
1952 doi: [10.1051/0004-6361/201628917](https://doi.org/10.1051/0004-6361/201628917)
- 1953 Zdziarski, A. A., Malyshev, D., Chernyakova, M.,
1954 & Pooley, G. G. 2017, *MNRAS*, 471, 3657,
1955 doi: [10.1093/mnras/stx1846](https://doi.org/10.1093/mnras/stx1846)
- 1956 Zhang, P. F., Xin, Y. L., Fu, L., et al. 2016,
1957 *MNRAS*, 459, 99, doi: [10.1093/mnras/stw567](https://doi.org/10.1093/mnras/stw567)

APPENDIX

A. DESCRIPTION OF THE FITS VERSION OF THE 4FGL CATALOG

Table 12. LAT 4FGL FITS Format: LAT_Point_Source_Catalog Extension

Column	Format	Unit	Description
Source_Name	18A	...	Source name 4FGL JHHMM.m+DDMMa ^a
RAJ2000	E	deg	Right Ascension
DEJ2000	E	deg	Declination
GLON	E	deg	Galactic Longitude
GLAT	E	deg	Galactic Latitude
Conf_68_SemiMajor	E	deg	Long radius of error ellipse at 68% confidence ^b
Conf_68_SemiMinor	E	deg	Short radius of error ellipse at 68% confidence ^b
Conf_68_PosAng	E	deg	Position angle of the 68% ellipse ^b
Conf_95_SemiMajor	E	deg	Long radius of error ellipse at 95% confidence
Conf_95_SemiMinor	E	deg	Short radius of error ellipse at 95% confidence
Conf_95_PosAng	E	deg	Position angle (eastward) of the long axis from celestial North
ROI_num	I	...	ROI number (cross-reference to ROIs extension)
Extended_Source_Name	18A	...	Cross-reference to the ExtendedSources extension
Signif_Avg	E	...	Source significance in σ units over the 100 MeV to 1 TeV band
Pivot_Energy	E	MeV	Energy at which error on differential flux is minimal
Flux1000	E	cm ⁻² s ⁻¹	Integral photon flux from 1 to 100 GeV
Unc_Flux1000	E	cm ⁻² s ⁻¹	1 σ error on integral photon flux from 1 to 100 GeV
Energy_Flux100	E	erg cm ⁻² s ⁻¹	Energy flux from 100 MeV to 100 GeV obtained by spectral fitting
Unc_Energy_Flux100	E	erg cm ⁻² s ⁻¹	1 σ error on energy flux from 100 MeV to 100 GeV
SpectrumType	18A	...	Spectral type in the global model (PowerLaw, LogParabola, PLSuperExpCutoff)
PL_Flux_Density	E	cm ⁻² MeV ⁻¹ s ⁻¹	Differential flux at Pivot_Energy in PowerLaw fit
Unc_PL_Flux_Density	E	cm ⁻² MeV ⁻¹ s ⁻¹	1 σ error on PL_Flux_Density
PL_Index	E	...	Photon index when fitting with PowerLaw
Unc_PL_Index	E	...	1 σ error on PL_Index
LP_Flux_Density	E	cm ⁻² MeV ⁻¹ s ⁻¹	Differential flux at Pivot_Energy in LogParabola fit
Unc_LP_Flux_Density	E	cm ⁻² MeV ⁻¹ s ⁻¹	1 σ error on LP_Flux_Density
LP_Index	E	...	Photon index at Pivot_Energy (α of Eq. 2) when fitting with LogParabola
Unc_LP_Index	E	...	1 σ error on LP_Index
LP_beta	E	...	Curvature parameter (β of Eq. 2) when fitting with LogParabola
Unc_LP_beta	E	...	1 σ error on LP_beta
LP_SigCurv	E	...	Significance (in σ units) of the fit improvement between PowerLaw and LogParabola. A value greater than 4 indicates significant curvature
PLEC_Flux_Density	E	cm ⁻² MeV ⁻¹ s ⁻¹	Differential flux at Pivot_Energy in PLSuperExpCutoff fit
Unc_PLEC_Flux_Density	E	cm ⁻² MeV ⁻¹ s ⁻¹	1 σ error on PLEC_Flux_Density
PLEC_Index	E	...	Low-energy photon index (Γ of Eq. 4) when fitting with PLSuperExpCutoff
Unc_PLEC_Index	E	...	1 σ error on PLEC_Index
PLEC_Expfactor	E	...	Exponential factor (a of Eq. 4) when fitting with PLSuperExpCutoff
Unc_PLEC_Expfactor	E	...	1 σ error on PLEC_Expfactor
PLEC_Exp_Index	E	...	Exponential index (b of Eq. 4) when fitting with PLSuperExpCutoff
Unc_PLEC_Exp_Index	E	...	1 σ error on PLEC_Exp_Index
PLEC_SigCurv	E	...	Same as LP_SigCurv for PLSuperExpCutoff model
Npred	E	...	Predicted number of events in the model

Table 12 continued on next page

Table 12 (continued)

Column	Format	Unit	Description
Flux_Band	7E	cm ⁻² s ⁻¹	Integral photon flux in each spectral band
Unc_Flux_Band	2 × 7E	cm ⁻² s ⁻¹	1σ lower and upper error on Flux_Band ^c
nuFnu_Band	7E	erg cm ⁻² s ⁻¹	Spectral energy distribution over each spectral band
Sqrt_TS_Band	7E	...	Square root of the Test Statistic in each spectral band
Variability_Index	E	...	Sum of 2×log(Likelihood) difference between the flux fitted in each time interval and the average flux over the full catalog interval; a value greater than 18.48 over 12 intervals indicates <1% chance of being a steady source
Frac_Variability	E	...	Fractional variability computed from the fluxes in each year
Unc_Frac_Variability	E	...	1σ error on fractional variability
Signif_Peak	E	...	Source significance in peak interval in σ units
Flux_Peak	E	cm ⁻² s ⁻¹	Peak integral photon flux from 100 MeV to 100 GeV
Unc_Flux_Peak	E	cm ⁻² s ⁻¹	1σ error on peak integral photon flux
Time_Peak	D	s (MET)	Time of center of interval in which peak flux was measured
Peak_Interval	E	s	Length of interval in which peak flux was measured
Flux_History	12E	cm ⁻² s ⁻¹	Integral photon flux from 100 MeV to 100 GeV in each year (best fit from likelihood analysis with spectral shape fixed to that obtained over full interval)
Unc_Flux_History	2 × 12E	cm ⁻² s ⁻¹	1σ lower and upper error on integral photon flux in each year ^c
Sqrt_TS_History	12E	...	Square root of the Test Statistic in each year
Variability2_Index	E	...	Variability_Index over two-month intervals; a value greater than 72.44 over 48 intervals indicates <1% chance of being a steady source
Frac2_Variability	E	...	Fractional variability computed from the fluxes every two months
Unc_Frac2_Variability	E	...	1σ error on Frac2_Variability
Signif2_Peak	E	...	Source significance in peak interval in σ units
Flux2_Peak	E	cm ⁻² s ⁻¹	Peak integral photon flux from 100 MeV to 100 GeV
Unc_Flux2_Peak	E	cm ⁻² s ⁻¹	1σ error on peak integral photon flux
Time2_Peak	D	s (MET)	Time of center of interval in which peak flux was measured
Peak2_Interval	E	s	Length of interval in which peak flux was measured
Flux2_History	48E	cm ⁻² s ⁻¹	Integral photon flux from 100 MeV to 100 GeV in each two-month interval
Unc_Flux2_History	2 × 48E	cm ⁻² s ⁻¹	1σ lower and upper error on Flux2_History ^c
Sqrt_TS2_History	48E	...	Square root of the Test Statistic in each two-month interval
ASSOC_FGL	18A	...	Most recent correspondence to previous FGL source catalogs, if any
ASSOC_FHL	18A	...	Most recent correspondence to previous FHL source catalogs, if any
ASSOC_GAM1	18A	...	Name of likely corresponding 2AGL source, if any
ASSOC_GAM2	18A	...	Name of likely corresponding 3EG source, if any
ASSOC_GAM3	18A	...	Name of likely corresponding EGR source, if any
TEVCAT_FLAG	A	...	P if positional association with non-extended source in TeVCat, N if no TeV association
ASSOC_TEV	24A	...	Name of likely corresponding TeV source from TeVCat, if any
CLASS1	5A	...	Class designation for associated source; see Table 7
CLASS2	5A	...	Class designation for low-confidence association
ASSOC1	28A	...	Name of identified or likely associated source
ASSOC2	26A	...	Name of low-confidence association or of enclosing extended source
ASSOC_PROB_BAY	E	...	Probability of association according to the Bayesian method ^d
ASSOC_PROB_LR	E	...	Probability of association according to the Likelihood Ratio method ^e
RA_Counterpart	D	deg	Right Ascension of the counterpart ASSOC1
DEC_Counterpart	D	deg	Declination of the counterpart ASSOC1
Unc_Counterpart	E	deg	95% precision of the counterpart localization ^f

Table 12 continued on next page

Table 12 (*continued*)

Column	Format	Unit	Description
Flags	I	...	Source flags (binary coding as in Table 5) ^g

^aThe letter at the end can be **c** (coincident with interstellar clump), **e** (extended source), **i** (for Crab nebula inverse Compton) or **s** (for Crab nebula synchrotron).

^bfrom the 95% ellipse, assuming a Gaussian distribution.

^cSeparate 1σ errors are computed from the likelihood profile toward lower and larger fluxes. The lower error is set equal to NULL and the upper error is derived from a Bayesian upper limit if the 1σ interval contains 0 ($TS < 1$).

^dNaN in this column when ASSOC1 is defined means that the probability could not be computed, either because the source is extended or because the counterpart is the result of dedicated follow-up.

^eProbabilities < 0.8 are formally set to 0.

^fFor extended counterparts, this reports their extension radius.

^gEach condition is indicated by one bit among the 16 bits forming **Flags**. The bit is raised (set to 1) in the dubious case, so that sources without any warning sign have **Flags** = 0.

1960 The FITS format version of the second release of the 4FGL catalog has eight binary table extensions.
 1961 The extension **LAT_Point_Source_Catalog_Extension** has all of the information about the sources.
 1962 Its format is described in Table 12.

1963 The extension **GTI** is a standard Good-Time Interval listing the precise time intervals (start and
 1964 stop in Mission Elapsed Time, MET) included in the data analysis. The number of intervals is fairly
 1965 large because on most orbits (~ 95 min) *Fermi* passes through the SAA, and science data taking is
 1966 stopped during these times. In addition, data taking is briefly interrupted on each non-SAA-crossing
 1967 orbit, as *Fermi* crosses the ascending node. Filtering of time intervals with large rocking angles,
 1968 gamma-ray bursts, solar flares, data gaps, or operation in non-standard configurations introduces
 1969 some more entries. The GTI is provided for reference and is useful, e.g., for reconstructing the
 1970 precise data set that was used for the analysis.

1971 The extension **ExtendedSources** (format unchanged since 2FGL) contains information about the
 1972 75 spatially extended sources that are modeled in the 4FGL source list (§ 3.4), including locations
 1973 and shapes. The extended sources are indicated by an e appended to their names in the main table.

1974 The extension **ROIs** contains information about the 1748 RoIs over which the analysis ran. In
 1975 particular it reports the best-fit diffuse parameters. Its format is very close to that in 3FGL, with
 1976 one exception. The **RADIUS** column is replaced by **CoreRadius** which reports the radius of the RoI
 1977 core (in which the sources which belong to the RoI are located). The RoI radius (half-width in binned
 1978 mode) depends on the component, and is given by the core radius plus **RingWidth**, where the latter
 1979 is given in the **Components** extension.

1980 The extension **Components** is new to 4FGL. It reports the settings of each individual component
 1981 (15 in all) whose sum forms the entire data set for the SummedLikelihood approach, as described in
 1982 Table 2. Its format is given by Table 13.

1983 The extension **EnergyBounds** is new to 4FGL. It contains the definitions of the bands in which
 1984 the fluxes reported in the **xx_Band** columns of the main extension were computed, and the settings
 1985 of the analysis. Its format is the same as that of the **Components** extension, plus one more column
 1986 (**SysRel**) reporting the systematic uncertainty on effective area used to flag the sources with Flag
 1987 10 (Table 5). When several components were used in one band, several lines appear with the same
 1988 **LowerEnergy** and **UpperEnergy**.

Table 13. LAT 4FGL FITS Format: Components Extension

Column	Format	Unit	Description
Emin	E	MeV	Lower bound of component's energy interval
Emax	E	MeV	Upper bound of component's energy interval
ENumBins	I	...	Number of bins inside energy interval
EvType	I	...	Event type selection for this component
ZenithCut	E	deg	Maximum zenith angle for this component
RingWidth	E	deg	Difference between RoI radius and core radius
PixelSize	E	deg	Pixel size for this component (of exposure map in unbinned mode)
BinnedMode	I	...	0=Unbinned, 1=Binned
Weighted	I	...	1 if weights were applied to this component

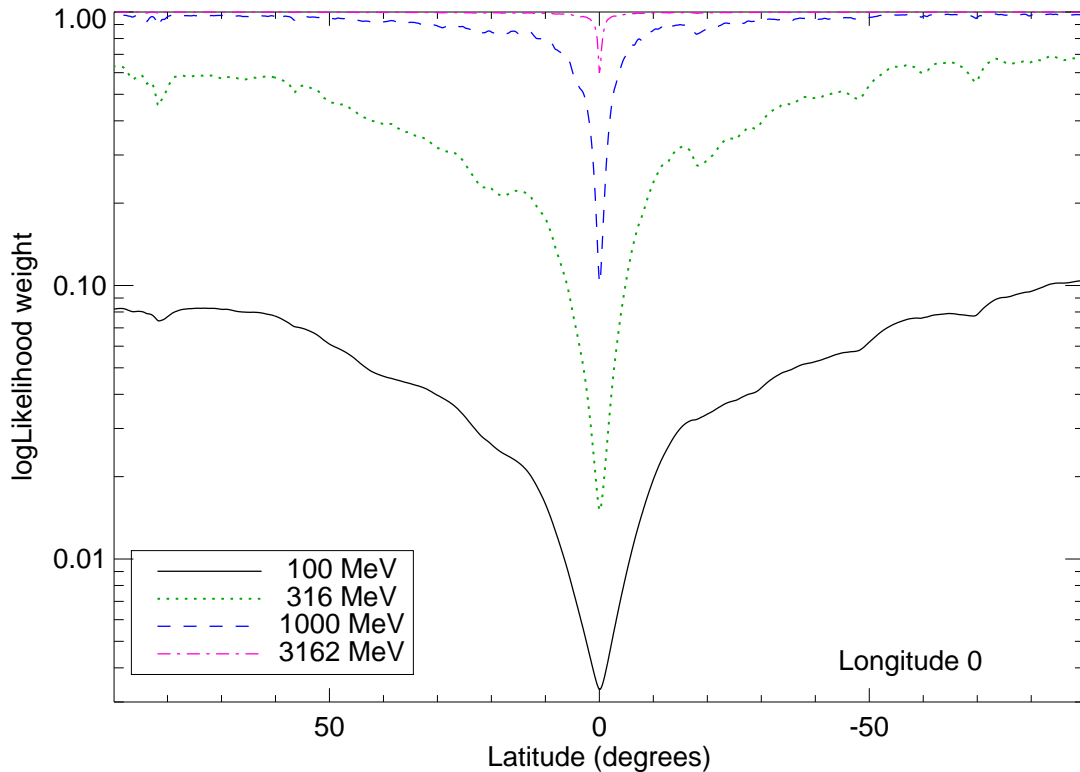


Figure 22. Data-based log-likelihood weights as a function of latitude across the Galactic Center, at 100 MeV, 300 MeV, 1 GeV and 3 GeV, assuming all events are used throughout, and the same zenith cut at 105° . The dips at some latitudes are point sources, which are included in the data-based weights. Those weights were not used in 4FGL (which uses separate event types), they are shown here only for illustration.

1989 The extension `Hist_Start` (format unchanged since 1FGL) contains the definitions of the time
1990 intervals used to build the light curves. The new extension `Hist2_Start` (same format) describes
1991 the time intervals used to build the second series of light curves.

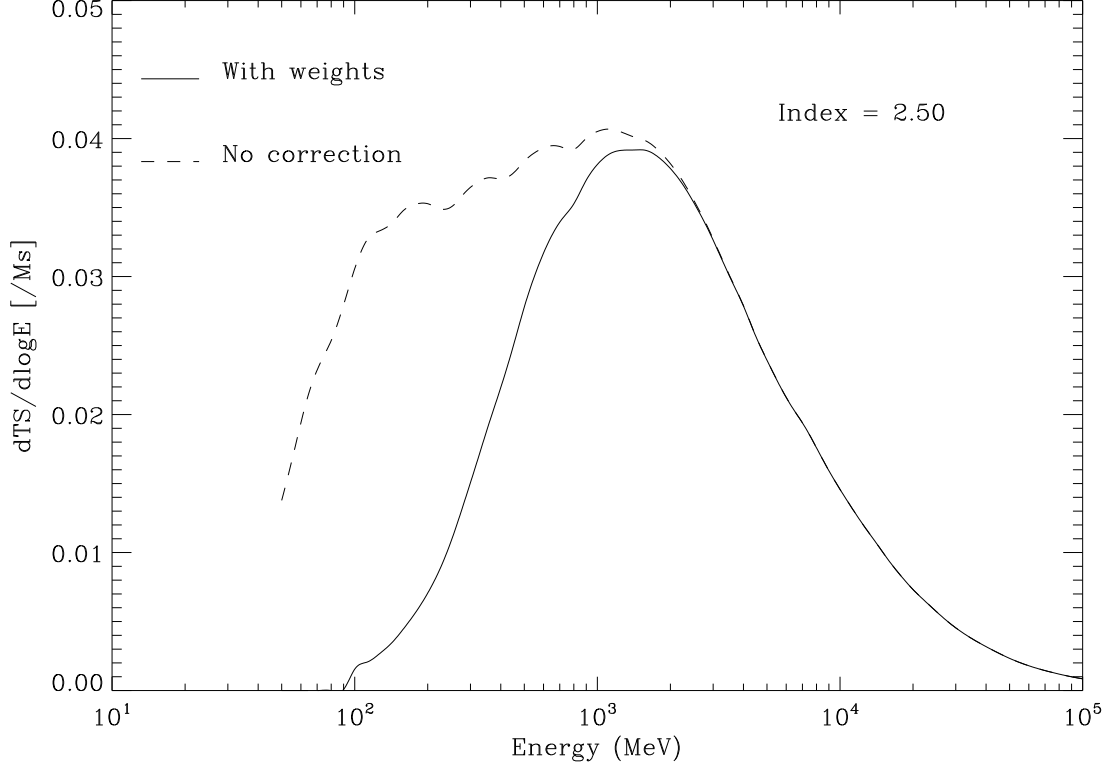


Figure 23. Contribution to TS as a function of energy for a power-law source with $\Gamma = 2.5$ at high latitude, with and without weights. This assumes all events are used throughout (and with the same zenith cut at 105°), as in Figure 22.

1992

B. WEIGHTED LOG-LIKELIHOOD

1993 In 3FGL we introduced a first attempt at accounting for systematic errors in the maximum
 1994 likelihood process itself, at the source detection level. It was not used in the source characterization,
 1995 however, for lack of a suitable framework. The standard way to account for systematic errors (for
 1996 example in *XSPEC*²⁷) is to define them as a fraction ϵ of the signal and add them to the statistical
 1997 errors in quadrature, in a χ^2 formalism. This can be adapted to the maximum likelihood framework
 1998 by introducing weights $w_i < 1$ (Hu & Zidek 2002) as

$$\log \mathcal{L} = \sum_i w_i (n_i \log M_i - M_i) \quad (\text{B1})$$

1999 where M_i and n_i are the model and observed counts in each bin, and the sum runs over all bins
 2000 in space and energy. The source significance can then be quantified in the same way, via the Test
 2001 Statistic $TS = 2 \log(\mathcal{L}/\mathcal{L}_0)$ in which \mathcal{L} and \mathcal{L}_0 are the (weighted) log-likelihood with and without
 2002 the source of interest, respectively.

2003 Since the statistical variance in Poisson statistics is the signal itself, a first guess for the weights
 2004 could be

$$w_i = \frac{M_i}{M_i + (\epsilon M_i)^2} = \frac{1}{1 + \epsilon^2 M_i} \quad (\text{B2})$$

²⁷ <https://heasarc.gsfc.nasa.gov/xanadu/xspec/>

2005 However, that formulation has a serious flaw, which is that it is not stable to rebinning. If one splits
 2006 the bins in half, then M_i is split in half while ϵ stays the same (it is defined externally). In the limit
 2007 of very small bins, obviously the weights will all tend to 1 and the $\log \mathcal{L}$ formula will tend to the
 2008 unweighted one, even though nothing has changed in the underlying data or the model.

2009 The solution we propose, originally presented in [Ballet et al. \(2015\)](#), is to define a suitable integral
 2010 over energy (E) and space (\mathbf{r}) $N(\mathbf{r}, E)$ which does not depend on binning. M_i in the weight formula
 2011 is then replaced by $N(\mathbf{r}_i, E_i)$ taken at the event's coordinates. For the integral over space, since the
 2012 catalog mostly deals with point sources, the logical solution is to integrate the background under
 2013 the PSF, i.e., to convolve the model with the PSF $P(\mathbf{r}, E)$, normalized to 1 at the peak (this is
 2014 equivalent, for a flat diffuse emission, to multiplying by the PSF solid angle). Note that the model
 2015 already contains the PSF, so this amounts to applying a double convolution to the sky model.

2016 For the energy integral the choice is less obvious. The source spectrum is not a narrow line, so
 2017 convolving with the energy dispersion (similar to what is done for space) is not justified. An integral
 2018 over the full energy range would give the same weight to all energies, which is clearly not what we
 2019 want (there is no reason to downplay the few high-energy events). The option we adopt here is to
 2020 start the integration at the current energy.

$$w_i = \frac{1}{1 + \epsilon^2 N(\mathbf{r}_i, E_i)} \quad (\text{B3})$$

$$N(\mathbf{r}_i, E_i) = \int_{E_i}^{E_{\max}} S(\mathbf{r}_i, E) dE \quad (\text{B4})$$

$$S(\mathbf{r}, E) = \frac{dM}{dE}(\mathbf{r}, E) * P(\mathbf{r}, E) \quad (\text{B5})$$

2021 where dM/dE is the differential model. As energy increases, the spectra (in counts) decrease and
 2022 the LAT PSF gets narrower so the convolution makes S even steeper than dM/dE . As a result, the
 2023 integral giving N is nearly always dominated by the lowest energies, so the exact upper bound E_{\max}
 2024 is not critical. The only spectral region where it is important is the very lowest energies (< 100 MeV)
 2025 where the effective area rises steeply. In order not to penalize the lowest energies too much, we set
 2026 $E_{\max} = 2E_i$ in Eq. B4.

2027 There are two possibilities to define dM/dE . Since the main origin of the systematic error is the
 2028 diffuse emission, we can restrict dM/dE to the diffuse emission model only (we call the result model-
 2029 based weights). On the other hand there are also systematic uncertainties on sources due to PSF
 2030 calibration and our imperfect spectral representation, so another option is to enter the full model (or
 2031 the data themselves) into dM/dE (we call the result data-based weights). That second choice limits
 2032 spurious sources next to bright sources. There is of course no reason why the level of systematics ϵ
 2033 should be the same for the diffuse emission model and the sources, but in practice it is a reasonable
 2034 approximation.

2035 Another important point, for the procedure to be stable, is that the weights should not change
 2036 with the model parameters. So dM/dE must be defined beforehand (for example from a previous
 2037 fit). In this work we use data-based weights computed from the data themselves, with a common ϵ .
 2038 The data are not as smooth as the model, but this is not a problem in the regime of large counts
 2039 where weights play a role.

2040 We assume here that ϵ is a true constant (it depends neither on space nor on energy). For a given
 2041 ϵ the weights are close to 1 at high energy and decrease toward low energy. At a given energy the

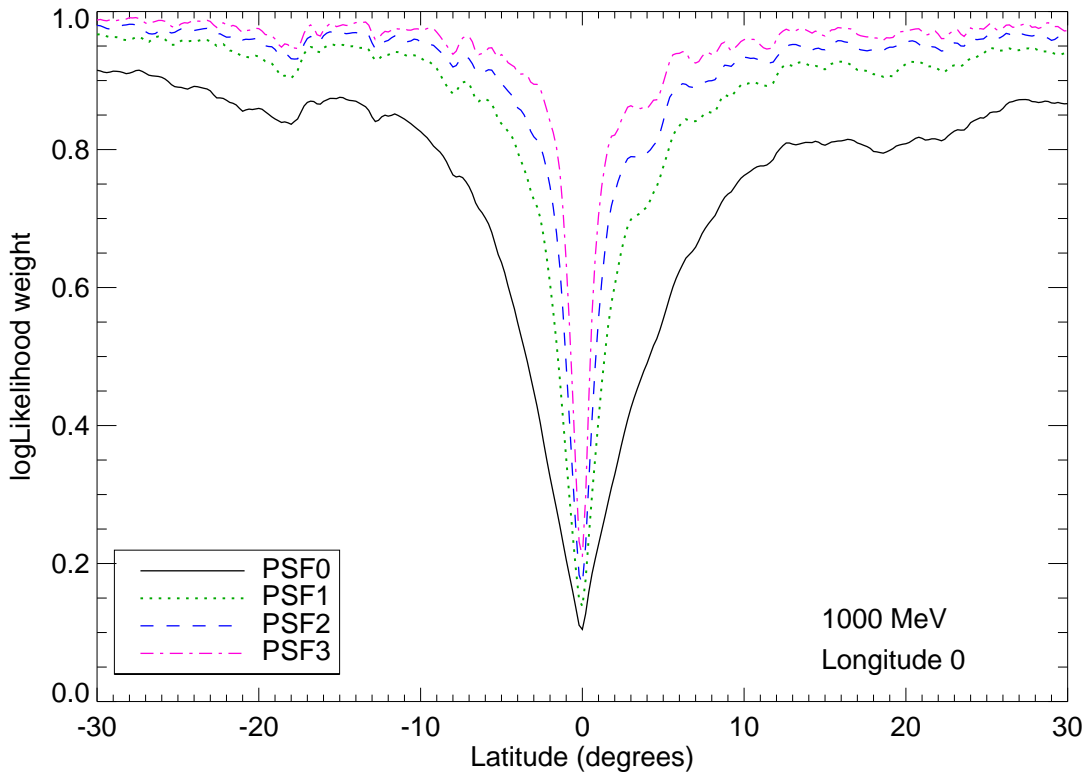


Figure 24. Data-based weights at 1 GeV for $Z_{\text{Max}} = 105^\circ$ as a function of latitude (for the interesting $[-30^\circ, 30^\circ]$ region) across the Galactic Center, for different PSF event types, computed according to Eq. B9. These weights were actually used in 4FGL. The average (over event types) weight is larger than the weight using all events together at the same 1 GeV energy (blue dashed line in Figure 22). This is because keeping event types separate is more favorable than merging them and losing the event type information.

weights are smallest where the data is largest (in the Galactic ridge). We illustrate that behavior in Figure 22, merging all event types together (not what we do in 4FGL), for 8 years and $\epsilon = 3\%$. The width of the trough in the Galactic Ridge gets narrower at high energy, as the PSF improves. At 100 MeV the weights are everywhere less than 12%. They reach 50% at high latitude at 250 MeV, and 90% at 500 MeV. This justifies our choice of discarding 75% of the events below 100 MeV and 50% below 300 MeV (Table 2). The entire sky is limited by systematic effects below 300 MeV. On average in the Galactic ridge (a little better than the very center shown in Figure 22), the weights are 0.5% at 100 MeV, 1.5% at 250 MeV, 5% at 500 MeV, 20% at 1 GeV, 60% at 2 GeV and reach 90% at 4.5 GeV.

Another way to illustrate the effect of the weights is Figure 23 (similar to Figure 18 of the 1FGL paper). It shows the contribution to TS of all energies, for a rather soft source at high latitude (the background and exposure are averaged over all latitudes larger than 10°), with and without weights. Energies below 300 MeV contribute very little when the weights are applied. This remains true with the actual data selection used in 4FGL.

A specific difficulty remains because at a given energy we split the data into several components, each corresponding to a particular event type (with a different PSF). Since the systematics act in the same way on all components, the weights must be computed globally (i.e., weights must be lower

when using PSF2 and PSF3 events than when using PSF3 alone). On the other hand, the resulting uncertainties with two components should be smaller than those with a single component (adding a second one adds information). In this work, we started by computing weights w_k individually for each component k (the dependence on E and \mathbf{r} is left implicit). Then we assumed that the final weights are simply proportional to the original ones, with a factor $\alpha < 1$ (α depends on E and \mathbf{r} as well). A reasonable solution is then

$$N_{\min} = \min_k N_k \quad (\text{B6})$$

$$K_{\text{tot}} = \sum_k \left(\frac{N_{\min}}{N_k} \right)^2 \quad (\text{B7})$$

$$\alpha = \frac{1 + \epsilon^2 N_{\min}}{1 + \epsilon^2 N_{\min} K_{\text{tot}}} \quad (\text{B8})$$

$$w_k = \frac{\alpha}{1 + \epsilon^2 N_k} \quad (\text{B9})$$

K_{tot} and α are 1 if one component dominates over the others, and K_{tot} is the number of components if they are all similar. The effect of this procedure is depicted in Figure 24 at 1 GeV, the lowest energy at which we use all event types. It illustrates quantitatively how the PSF0 events are unweighted at low latitudes, compared to better event types.